Politecnico di Torino

Politecnico di Torino

Master's Degree in Aerospace Engineering

Graduation Session March/April 2026

Models for the Structural Design of a Pressurized Rover for Lunar Exploration

Tutors:

Giuseppe Palaia

Matteo Filippi

Marco Petrolo

Candidate:

Simone Camposeo

«Remember to look up at the stars
and not down at your feet»

Stephen Hawking

Abstract

This thesis develops a parametric framework for the sizing of the primary structure of a pressurized rover, with the objective of identifying minimum-mass configurations while satisfying the main structural constraints.

The model treats geometric parameters and structural element properties as design variables and evaluates the rover's response under representative loading conditions, including lunar surface operations and launch environment loads. Verification criteria include allowable stress limits and dynamic requirements associated with launch-induced vibrations.

The framework is implemented in a Matlab environment and interfaced with commercial FEM software (MSC Patran/Nastran) to enable automated structural analyses. The developed architecture autonomously generates numerical models consistent with user-defined inputs and returns result matrices suitable for parametric analyses and sensitivity studies. A surrogate-based optimization strategy is employed to identify minimum-mass configurations within the defined design space.

The outcome is a flexible and scalable tool supporting the preliminary design phase of pressurized rovers, providing both qualitative and quantitative insights into the assessment of conventional and innovative structural configurations.

Table of Contents

List of Tables

List of Figures

Glossary

BDF

Bulk Data File

DBTT

Ductile-to-Brittle Transition Temperature

DIPS

Dynamic Isotope Power System

ECLSS

Environmental Control and Life Support System

EMU

Extravehicular Mobility Unit

EVA

Extra-Vehicular Activity

FCSP

Foam Core Sandwich Panel

FEM

Finite Element Method

FH

Falcon Heavy

FI

Failure Index

FNF

First Natural Frequency

GCR

Galactic Cosmic Rays

GEL

Global Edge Length

HCSP

Honeycomb Core Sandwich Panels

HDF5

Hierarchical Data Format version 5

ISRU

In Situ Resource Utilization

MDB

Mesh Double Bumper

MLI

Multi Layer Insulation

MMOD

MicroMeteoroid and Orbital Debris

MPC

Multi Point Constraint

MPE

Maximum Predicted Environment

MSS

Multi-Shock Shields

OASPL

Overall Sound Pressure Level

PCL

Patran Command Language

PSD

Power Spectral Density

RBE3

Rigid Body Element 3

RTG

Radioisotope Thermoelectric Generator

SBO

Surrogate-Based Optimization

SF

Safety Factor

SPL

Sound Pressure Level

SWS

Stuffed Whipple Shield

TCS

Thermal Control System

TRL

Technology Readiness Level

WS

Whipple Shield

Chapter 1

Introduction

1.1 Aim

The objective of this thesis is the development of a parametric framework for the preliminary sizing of the primary structure of a pressurized rover for lunar exploration missions. In particular, the study aims to identify minimum-mass structural configurations that satisfy the main strength and stiffness constraints imposed by both the launch environment and lunar surface operations.

As a preliminary step, the work includes a general discussion on the sizing of passive protection systems required for long-duration surface missions. Simple analytical models are adopted to provide first-order estimates for the preliminary design of the thermal protection system, with particular focus on Multi Layer Insulation (MLI), as well as for the MicroMeteoroid and Orbital Debris (MMOD) shielding. Since these systems are located in the outer region of the vehicle, they must be taken into account in order to obtain an overall assessment of the mass and volumetric constraints of the rover.

To support the structural assessment, a parametric model is defined in which the design variables include both geometric parameters and structural element properties. The framework enables the evaluation of the rover's structural performance under representative loading conditions, including quasi-static and dynamic loads experienced during launch, as well as operational loads in the lunar environment. The verification criteria include compliance with allowable stress limits and dynamic requirements associated with vibration loads.

A key aspect of the work is the development of an automated computational architecture, implemented in a Matlab environment and interfaced with commercial finite element analysis software. The tool is capable of automatically generating numerical models consistent with user-defined inputs and efficiently processing the results, enabling parametric analyses and sensitivity studies.

Particular emphasis is placed on the application of a Surrogate-Based Optimization (SBO) strategy to identify minimum-mass solutions. The framework is applied to several geometric configurations of the pressurized rover, enabling a systematic comparison of their structural efficiency and highlighting the influence of the main design parameters.

Overall, the goal is to provide a flexible and scalable tool to support the preliminary design phase, delivering both qualitative insights and quantitative assessments for the comparison of conventional and innovative structural configurations.

1.2 Context

In recent years, interest in lunar surface exploration has significantly increased, primarily driven by the Artemis program promoted by NASA. This initiative aims to return humans to the Moon by the end of the decade and to establish a sustainable human presence,focusing on the exploration of the lunar south pole and the development of enabling technologies for future missions to Mars [1].

At the same time, several other countries with active space programs are pursuing similar initiatives. In particular, China, through its lunar exploration program (the Chang'e missions), aims to achieve a crewed lunar landing and to develop an international lunar base, the International Lunar Research Station, in the coming decades [2].

From a scientific point of view, the Moon offers unique opportunities for radio astronomy: permanently shadowed craters on the far side provide a naturally shielded environment from terrestrial electromagnetic interference, making them ideal for the installation of radio telescopes dedicated to the study of the early universe [3]. The establishment of permanent or semi-permanent scientific outposts on the lunar surface would also enable a wide range of in-situ investigations. In particular, it would allow detailed geological studies of the lunar regolith and subsurface, improving our understanding of the Moon's formation, thermal evolution, and impact history. Furthermore, such infrastructures would provide a unique platform to study biological processes under reduced gravity conditions, including the growth and adaptation of plant life. These studies are essential for the development of bio-regenerative life support systems and for enabling long-duration human missions beyond Low Earth Orbit.

However, the interest in the Moon is not limited to scientific exploration alone. It also represents a key environment for the development of advanced technologies and a potential platform for future economic activities. Among these, particular relevance is given to In Situ Resource Utilization (ISRU), including the extraction of water ice (primarily located in the lunar south pole region) and its processing to produce oxygen and hydrogen, which could be used both as life-support resources

and as propellant components for space transportation systems [4], as well as the potential exploitation of rare earth elements [5]. In addition, the Moon can serve as a logistical node for deep-space missions, contributing to cost reduction and increasing the sustainability of future exploration campaigns [6].

A further element of interest is the potential exploitation of Helium-3, an isotope that is extremely rare on Earth but relatively abundant in the lunar regolith, and which has been proposed as a possible resource for future nuclear fusion applications. Although the technologies required for its large-scale utilization are not yet mature, its presence further contributes to the long-term strategic value of the Moon [7].

This renewed global interest highlights how the Moon represents today a strategic objective from scientific, technological, and economic perspectives, fostering the development of new engineering solutions for long-duration missions.

Within this context, pressurized rovers represent a versatile and broadly applicable technological class, essential for long-duration missions on the lunar surface. They provide a protected environment for astronauts, enabling the extension of both range and duration of extravehicular activities. Vehicles in this category can vary in characteristics and functions but can be grouped into three main types:

- transport vehicles, designed to move crew and cargo between bases or points of interest;
- medium- to long-range exploration vehicles, capable of supporting crew life and operations during autonomous missions;
- autonomous mobile scientific platforms, intended as independent environments for conducting scientific experiments or commercial activities while in transit.

1.3 State of the Art

1.3.1 Unpressurised Rovers

All planetary surface rovers successfully operated to date are unpressurised vehicles, reflecting both the technological constraints and mission architectures adopted in early and contemporary planetary exploration. These systems operate either fully autonomously, through teleoperation from Earth, or as crewed open vehicles requiring astronauts to remain in spacesuits during all surface activities.

From an engineering perspective, unpressurised rovers offer significant advantages in terms of mass, structural simplicity, and reduced system complexity. The absence of a pressure vessel eliminates the need for atmospheric containment, thermal control for habitable volumes, and integrated life-support systems, enabling more efficient use of mass and power for mobility and scientific payloads. This has made

unpressurised configurations particularly suitable for robotic exploration missions, where autonomy, reliability, and energy efficiency are primary design drivers.

The following subsections describe the main unpressurised rover missions chronologically, highlighting key engineering characteristics and operational performance.

Apollo Lunar Roving Vehicle (LRV), 1971-1972

The Apollo Lunar Roving Vehicle (LRV) was an electrically powered crewed rover designed to extend the reach of Apollo astronauts beyond the immediate vicinity of the lunar module. Three units were deployed on Apollo 15, 16, and 17. Each was used on three Extra-Vehicular Activity (EVA) traverses over the three-day surface phase of each mission. The longest single traverse recorded was 20.1 km, while the greatest distance achieved from the lunar module was 7.6 km, both during Apollo 17. The LRV had a mass of 210 kg and was engineered to carry a payload of up to 490 kg on the lunar surface, reflecting the reduced gravitational environment. The chassis consisted of a three-part aluminium alloy (Al-2219) frame hinged at the centre for folded stowage in the lunar module's equipment bay. The four wire-mesh wheels incorporated titanium chevron cleats over 50% of the contact area for traction, and were individually driven by 190 W DC series motors. Power was supplied by two non-rechargeable 36 V silver-zinc batteries with a combined capacity of 121 A h [8, 9].

Soviet Lunokhod Programme, 1970-1973

The Soviet Union's Lunokhod programme deployed two teleoperated robotic rovers on the lunar surface, representing the first successful robotic surface exploration missions beyond Earth. Both rovers were controlled by a five-person team on Earth transmitting commands in real time via onboard cameras. Lunokhod 1, with a mass of 900 kg, landed in the *Mare Imbrium* in November 1970. Designed for a nominal 90-day operational life, it ultimately operated for 11 months, covering 11 km while returning television imagery and scientific data. Lunokhod 2, an improved version with an additional television camera, landed in the *Le Monnier* crater in January 1973. Measuring 135 cm in height, 170 cm in length, and 160 cm in width with a mass of 840 kg, it featured eight independently suspended and braked wheels, two speed settings ($\sim$1 km/h and $\sim$2 km/h), solar panel charging, and a radioisotopic heat source to maintain thermal equilibrium during the two-week lunar night. Lunokhod 2 traversed 37 km in eight weeks: a distance record for planetary rovers that stood for decades [8].

Mars Pathfinder – Sojourner, 1997

The Mars Pathfinder mission, originally conceived as a technology demonstration of a novel entry, descent, and landing architecture, also carried the first successful Mars surface rover: Sojourner. With a mass of only 11 kg, it demonstrated that a compact, low-cost robotic rover could operate effectively in the Martian environment. A six-wheeled vehicle with this configuration can surmount obstacles three times larger than those manageable by a four-wheeled vehicle of equivalent wheel size; Sojourner could negotiate rocks exceeding 20 cm. During its approximately four months of surface operation, Sojourner traversed a total of roughly 100 m at speeds of up to 0.036 km/h [8].

Mars Exploration Rovers – Spirit and Opportunity, 2004-2018

The Mars Exploration Rover (MER) mission deployed two geologically focused rovers: Spirit (*Gusev Crater*) and Opportunity (*Meridiani Planum*). Both rovers greatly exceeded their design lifetimes, with Spirit operating until 2010 and traversing over 7.7 km, and Opportunity remaining active until 2018, achieving approximately 45 km. Minor anomalies included increased motor current draw on Spirit's right front wheel, which was subsequently driven backwards to extend its life [8].

Mars Science Laboratory – Curiosity, 2012-present

NASA's Mars Science Laboratory mission landed the Curiosity rover in *Gale Crater* in August 2012. Curiosity represented a substantial step up in scale and capability: with a mass of approximately 899 kg, it is roughly five times heavier than the MER rovers, and was the first Mars rover powered by a Multi-Mission Radioisotope Thermoelectric Generator (MMRTG) rather than solar panels, providing approximately 110 W of continuous electrical power independent of solar flux and dust accumulation. As of 2024, Curiosity had traversed over 30 km and remained operational, although significant wheel damage accumulated on rocky terrain [8].

Mars 2020 – Perseverance, 2021-present

The Perseverance rover, landed in *Jezero Crater* in February 2021, built upon the Curiosity chassis architecture while incorporating a redesigned wheel geometry and an upgraded MMRTG power system. Among its most significant additions are a sample caching system capable of sealing drilled core samples in hermetically sealed tubes for potential future return to Earth, and the Mars Oxygen In-Situ Resource Utilization Experiment (MOXIE), which successfully demonstrated electrochemical extraction of oxygen from the Martian atmosphere, which is a technology directly relevant to life support and propellant production for crewed missions. As of early

2024, Perseverance had traversed over 22 km. It also served as the base station and communication relay for the Ingenuity helicopter, the first powered aerial vehicle to fly on another planet [8].

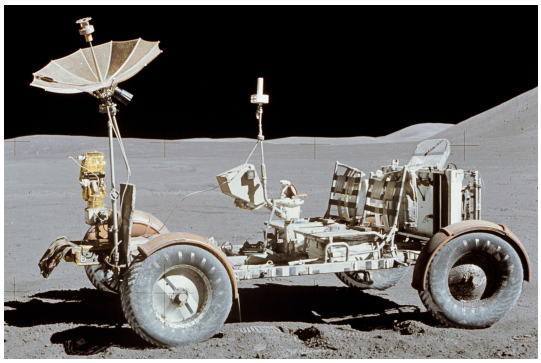

(a) LRV (NASA image)

(b) Curiosity (NASA/JPL-Caltech image)

Figure 1.1: Images of unpressurised rovers

1.3.2 Pressurised Rovers

While all rovers deployed to date have been unpressurised, the requirements of long-duration human surface exploration demand vehicles capable of providing a fully enclosed, life-supporting environment independent of spacesuits. A pressurised rover allows the crew to operate in shirt-sleeve conditions, significantly reducing fatigue and the operational complexity associated with EVA suits. It also provides inherently improved radiation shielding relative to unpressurised configurations, and enables sustained multi-day or multi-week traverses at distances far beyond what is feasible in a suit-limited EVA. These concepts are reviewed below, grouped by the nature and scale of the vehicle.

Rover First – Boeing / NASA (1992)

The Rover First concept, developed by Boeing under a NASA study, represents one of the most operationally efficient early pressurised rover architectures. Its defining feature is the elimination of a dedicated landing stage: the rover is designed to land directly on its own wheels, using the suspension system in conjunction with lightweight crushable elements to absorb landing loads. This approach saved considerable launch mass that would otherwise be consumed by a separate descent stage. The vehicle consists of a cylindrical pressure vessel 4.1 m in length and 2.6 m in diameter, sized to fit within a Titan IV shroud or the Shuttle payload bay, with a landed mass limited to 4.3 t. Power during crewed operations is

provided by fuel cells (8 kW), with a 700 W solar array/battery system supporting teleoperation between crew sorties. The rover is equipped with a manipulator arm with interchangeable end-effectors, usable in both crewed and teleoperated modes. Regarding crew capacity, the rover accommodates two persons for up to 14 days, with a nominal range of 80 km, assuming 16 hours of daily driving [8].

Pressurised Lunar Rover (PLR) – Virginia Tech / USRA (1992)

Two separate pressurised rover studies conducted by students at Virginia Polytechnic Institute and State University under the NASA/USRA Advanced Design Programme produced distinct but complementary designs. The first study [10] produced a single cylindrical vehicle 7 m in length and 3 m in diameter with a total mass of 6.2 t. The pressure vessel shell is constructed from layered carbon-fibre/foam composite. A Radioisotope Thermoelectric Generator (RTG) mounted on a detachable trailer produces 6.7 kW of continuous electrical power. Steered by differential wheel speed (skid steering), the rover achieves a nominal speed of 10 km/h and a maximum of 18 km/h, with an operational radius of 500 km and a crew capacity of four for 14 days. The second study [11] took a more unconventional approach by proposing two cylindrical pressure hulls, each 5 m in length and 4 m in diameter, passively connected by a pressurised flexible passageway, for a total vehicle length of 11 m and mass of 7.0 t. A Dynamic Isotope Power System (DIPS) operating on a closed Brayton cycle provides a constant 8.5 kW. Nominal speed is 14.7 km/h with a maximum of 29.4 km/h and a nominal range of 2000 km.

Mars Pressurised Rover – Hoffman & Kaplan (1997)

Proposed as part of a comprehensive NASA Mars mission reference study, the Hoffman and Kaplan pressurised rover is explicitly designed for the demands of long-duration Mars surface exploration, centred on an 18-to-20-month surface stay. The vehicle features a cylindrical pressure vessel with spherical end caps and an integrated airlock, with a total landed mass of 16.5 t. Four cone-shaped wheels, each independently driven through a speed-reducing electric motor transmission, provide mobility at a maximum speed of 10 km/h over a range of 500 km assuming 10 hours per day of operation. A DIPS producing 10 kW of continuous electrical power is mounted on a separate towed trailer, isolating the primary radiation source from the crew compartment. The rover can be docked directly to the base habitat module via a compatible interface, enabling shirt-sleeve crew transfer. Crew capacity is two persons for up to 20 days per sortie, with 10 days allocated to on-site research [12].

Daylight Rover – Boeing / Finley (1990)

The Daylight Rover concept, developed for Boeing by Finley, is among the most capable single-mission pressurised rover designs in the literature. With a mass of 23 t, it incorporates two cylindrical pressure vessels: the forward module serves as the primary driving station, while the rear module functions as both a storm shelter (for solar particle event refuges) and the EVA airlock. This dual-vessel architecture places the primary EVA ingress/egress point at the vehicle's rear, separating it physically from the primary crew workspace. 10 kW of continuous electrical power are supplied by regenerative fuel cells. Two forward-mounted manipulator arms perform the majority of geological sampling and sample transfer through a small forward airlock, substantially reducing EVA frequency and associated dust contamination risk. The vehicle supports a crew of two for up to 80 days with a range of 1000 km, at an average speed of 4 km/h in daylight and 2 km/h in darkness. Emergency capacity is four persons [8].

Lunar Polar Mission Rover – Arno (1999)

Applied to a hypothetical lunar polar mission, the resulting pressurised rover concept is compact (6.08 t) and purpose-designed for ISRU activities: it carries up to 500 kg of ploughing, drilling, and digging equipment, and is equipped with manipulator arms capable of lifting 50 kg payloads. A 6 mm-thick aluminium shell with stiffener construction is designed for robustness in rugged operations. Power is provided by fuel cells (2.5 kW continuous). Maximum speed is 20 km/h on solid ground. Crew capacity is three persons for a 6-day sortie with a 100 km range [8].

Mobile Base Concepts

A distinct class of pressurised mobility concept removes the constraint of a fixed base entirely by making the entire surface habitat mobile. This approach eliminates the logistical requirement to return periodically to a stationary base and provides full-base redundancy at every exploration site.

The Habot (Habitat Robot) concept takes a fundamentally modular approach. Individual habitat units, each up to 5 m in diameter and 10 t, land on six articulated legs that also provide surface locomotion at up to approximately 1 km/h. Photovoltaic cells power the units during the 14-day lunar day, while the units enter a low-power stationary mode during lunar night. A six-unit configuration can support a crew of six for a 100-day mission. The primary engineering challenge is the complexity and mass of the articulated leg mechanisms relative to wheeled alternatives.

The MORPHLAB (Modular Roving Planetary Habitat, Laboratory, and Base), proposed by the University of Maryland, offers a sophisticated modularity. Six 4 m

diameter habitat modules and four power modules land and autonomously assemble into a long-duration base. Upon completion of the manned phase, the modules disassemble, reconfigure into transit assemblies (one power module powering two habitat modules), and autonomously relocate to an alternative site up to 1000 km away. A DIPS distributed across four power modules provides up to 20 kW peak. The system supports four crew for 90-day missions [8, 13].

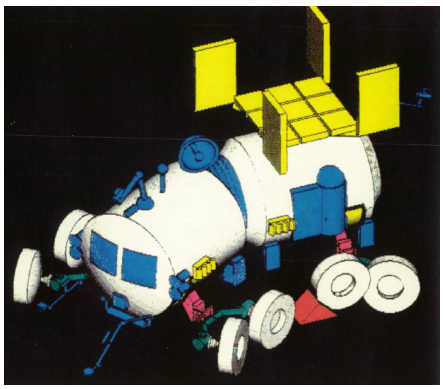

(a) PLR II (concept: Bhardwaj et al; image credit: NASA)

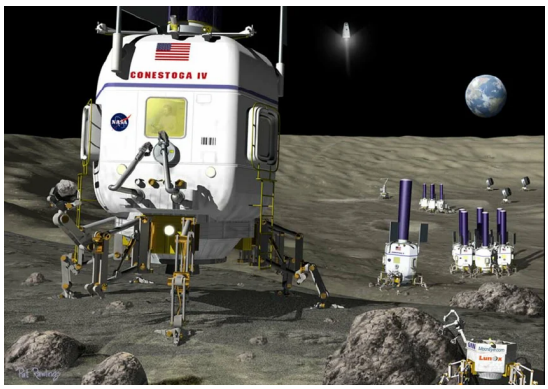

(b) Habot (concept: Mankins; artist credit: Pat Rawlings)

Figure 1.2: Concept designs of pressurised rovers

Table 1.1: Comparative summary of pressurised rover concepts

Concept	Origin	Crew	Mass	Range	Duration	Power Source
Rover First	Boeing / NASA, 1992	2	4.3 t	80 km	14 days	Shuttle fuel cells (8 kW)
PLR – Creel	Virginia Tech / USRA, 1992	4	6.2 t	500 km	14 days	RTG (6.7 kW)
PLR – Bhardwaj	Virginia Tech / USRA, 1992	4	7.0 t	2000 km	14 days	DIPS (8.5 kW)
Mars Press. Rover	Hoffman & Kaplan, 1997	2 (+4 emerg.)	16.5 t	500 km	20 days	DIPS (10 kW)
Daylight Rover	Boeing / Finley, 1990	2 (+4 emerg.)	23 t	1000 km	80 days	Regen. fuel cells (10 kW)
Lunar Polar Rover	Arno, 1999	3	6.08 t	100 km	6 days	Fuel cells (6 kW)
Habot	Mankins, 2000	6	10 t/mod	–	100 days	Photovoltaic cells
MORPHLAB	Univ. of Maryland	4	3.7 t/mod	1000 km	90 days	DIPS (20 kW)

Chapter 2

Lunar environment

2.1 Soil composition

The lunar soil, commonly referred to as regolith, is the unconsolidated superficial layer covering the Moon's crust and is the result of an extremely long evolution dominated by meteoritic impact processes. In the absence of an atmosphere and erosive agents such as water and wind, regolith formation has primarily occurred through the progressive fragmentation of surface rocks and the subsequent reworking of debris by successive impacts. This process has led to the formation of a highly heterogeneous material, both in terms of grain size distribution and composition.

The lunar surface is primarily divided into two major terrain types:

- Maria (singular: *mare*) are extensive, relatively flat and dark regions formed by ancient volcanic activity. They mainly consist of basaltic lava flows that filled large impact basins billions of years ago. Owing to their composition, maria exhibit a lower albedo and a smoother morphology compared to the surrounding terrain. They are predominantly located on the near side of the Moon. In these regions, the regolith thickness is typically on the order of 3 m.
- Highlands (Latin: *terrae*, singular: *terra*) are brighter and heavily cratered regions representing the oldest portions of the lunar surface. They feature rough topography, high crater density, and thicker regolith layers due to prolonged meteoritic bombardment. In these areas, the underlying bedrock is typically found at depths of approximately 15 m.

From the standpoint of particle size distribution, lunar regolith exhibits characteristics similar to very fine silty sand. The average grain size typically ranges between 45 and 100 µm, with a mean value around 60 µm. However, what fundamentally distinguishes this material from terrestrial soils is the morphology

of the grains: they are generally angular, irregular, and often characterized by glassy surfaces. This peculiarity arises from the absence of fluid-driven erosion processes that would otherwise round the particles, as well as from localized melting phenomena caused by high-energy impacts.

The composition of lunar soil reflects both the nature of the parent rocks and the effects of impact processes. Analysed samples show a complex mixture consisting of lithic fragments derived from both basaltic regions and anorthosite-rich highlands. These are accompanied by glassy components and, in particular, agglutinates, which represent one of the most distinctive features of lunar regolith. Agglutinates are aggregates of particles cemented by glass formed during meteoritic impacts and testify to the intense bombardment that has affected the lunar surface throughout its history.

A key aspect from an engineering perspective is represented by the physical properties of the soil, which are strongly influenced by its granular structure and compaction history. Despite its unconsolidated nature, lunar regolith exhibits surprisingly high relative density values even at shallow depths. Within the first 15 cm, the relative density is approximately 65%, while below 30 cm it can exceed 90%. This behaviour is attributed to the repeated action of shock waves generated by meteoritic impacts, which have progressively compacted the soil over time.

The soil structure directly affects several macroscopic properties, including thermal conductivity, mechanical strength, compressibility, and electromagnetic characteristics. In particular, the dependence of these properties on relative density implies that even small variations in compaction can lead to significant changes in material behaviour. This is of fundamental importance for engineering applications such as rover mobility, structural anchoring, and drilling operations [14, 15].

2.2 Thermal environment

The thermal environment of the Moon is determined almost exclusively by the interaction between the surface and solar radiation, in the absence of an atmosphere or convective processes. The lack of a heat-transferring medium leads to particularly extreme thermal conditions: during the lunar day, solar energy is absorbed by the surface and stored in the upper layers of the soil, whereas during the night heat loss occurs solely by radiation into space. In this context, the thermal conductivity of the regolith plays a fundamental role in determining the system's thermal response.

Measurements conducted during the Apollo missions have shown that surface temperatures vary significantly over the course of the lunar day. Near lunar dawn, the surface can reach minimum temperatures on the order of 92 K, while in the middle of the day maximum temperatures of up to approximately 374 K are recorded. The overall variation over a single day–night cycle (with an average duration of

about 29.531 Earth days) is therefore on the order of 280 K, an extremely high value compared to any terrestrial environment.

A particularly relevant aspect is the strong temperature variation with depth. It is estimated that, near the Apollo landing sites, the subsurface temperature below 30 cm remains nearly constant at approximately 254.8 K [16]. This is especially important for the design of underground habitats, which exploit this characteristic of the lunar regolith to shield occupants from extreme thermal fluctuations and radiation.

An additional source of complexity is the spatial variability of surface temperatures. Thermal conditions can change significantly depending on latitude and local morphology. In particular, in polar regions and within permanently shadowed craters, temperatures remain extremely low and constant, on the order of 40 K. Conversely, in equatorial regions, thermal excursions are maximal, with monthly variations that can reach approximately 140 K (Table 2.1) [15].

This strong spatial heterogeneity is further influenced by the local surface geometry. Studies conducted on craters at non-polar latitudes indicate that crater floors can be slightly warmer than the walls and outer slopes due to self-radiation and shading effects. Although relatively small, these differences can have a significant impact on the design of systems sensitive to local thermal conditions [15].

Table 2.1: Estimated lunar surface temperatures

	Shadowed Polar Craters	**Other Polar Areas**	**Front Equatorial**	**Back Equatorial**	**Limb Equatorial**	**Typical Mid-Latitudes**
Average temp.	40 K	220 K	254 K	256 K*	255 K	$220 < T < 255$ K
Monthly range	none	± 10 K†	± 140 K	± 140 K	± 140 K	± 110 K

* The far side of the Moon receives slightly more solar energy at local noon than the near side, resulting in approximately 1% higher peak temperatures.

† The average temperature exhibits a yearly variation, causing the surface to remain very cold (T < 200 K) for several weeks.

2.3 Radiation environment

The lunar radiation environment is characterized by exposure levels significantly higher than those found on the Earth's surface. This condition is a direct consequence of the absence of both a substantial atmosphere and a global magnetic field, which on Earth play a fundamental role in shielding against ionizing radiation. As a result, the lunar surface is directly exposed to a wide range of energetic particles originating from interplanetary space.

The main components of the incident radiation include the solar wind, galactic

cosmic rays, and solar energetic particles. The solar wind is predominantly composed of low-energy ions, typically on the order of 1 keV/u (keV per atomic mass unit, or keV per nucleon for nuclei), which continuously strike the lunar surface. Although these particles are not particularly penetrating, they play an important role in surface alteration processes, particularly through the implantation of volatile species into the outer layers of regolith grains [7].

Galactic Cosmic Rays (GCR), in contrast, represent the most energetic and penetrating component of the lunar radiation field. They consist of high-energy particles, often exceeding 1 GeV/u, including both protons and heavy nuclei. The primary particles of this component can penetrate several centimetres into the soil; however, their most significant effect arises from the production of secondary particles, generated through nuclear interactions with surface material. In particular, neutrons produced by these interactions can propagate to depths on the order of meters, contributing substantially to the overall radiation dose.

Solar energetic particles, often associated with flares and other transient phenomena, constitute an additional source of risk. Although their average contribution is generally lower than that of GCR, particularly intense solar events can cause a significant and sudden increase in radiation flux. These events, which typically occur with a frequency of about one per decade, represent one of the main hazards for the safety of systems and personnel on the lunar surface [15].

2.4 Electrostatic properties

The electrical conductivity of the regolith is extremely low; this property implies that electric charges, once accumulated, tend to dissipate very slowly, promoting the establishment of persistent charging conditions on the surface of the grains.

A key role is played by electromagnetic radiation, particularly in the ultraviolet and visible bands. Exposure to such radiation causes a rapid increase in surface conductivity, which decays just as quickly once the irradiation ceases. This behaviour introduces a coupling between illumination conditions and the electrical state of the soil, promoting the formation of potential gradients on the lunar surface. Near the terminator, the boundary between illuminated and shadowed regions, the sudden change in solar radiation intensity generates local variations in conductivity and electric potential, producing electric fields capable of mobilizing dust. These fields can lift regolith particles up to heights of about 10 m, forming clouds of particulate matter. However, the primary source of dust lifting during the mission will be human activity, both during the landing phase and throughout rover traverses.

The operational implications of these phenomena are numerous and significant. Electrostatic dust mobilization can reduce local visibility, interfere with optical instruments and sensors, and compromise the performance of mechanical systems.

Furthermore, the strong tendency of dust to adhere to exposed areas represents one of the main challenges for lunar surface operations. It has been observed that lunar dust can stick to painted and metallic components with considerable force, making its removal difficult. This phenomenon leads to a reduction in the efficiency of solar panels and affects the optical and thermal properties of materials exposed to the external environment [15, 17].

2.5 Light conditions

Under direct illumination, solar radiation incident on the lunar surface is not subject to diffuse scattering, as it is on Earth due to the presence of the atmosphere. As a result, illuminated regions appear extremely bright, while shadowed areas are characterized by near-total darkness. This sharp difference between light and shadow produces very high contrast, with significant implications for human vision, optical systems, and navigation sensors.

A distinctive aspect of lunar illumination is the strong directionality of sunlight. In the absence of atmospheric scattering, light originates almost exclusively from a single direction, determined by the position of the Sun relative to the surface. This leads to the formation of pronounced and well-defined shadows, which can become particularly long when the Sun is at a low elevation above the horizon. Under these conditions, even small surface irregularities can cast extended shadows, significantly altering the perception of surface morphology [15].

Understanding these illumination conditions is particularly important during mission planning, especially when solar panels are used as a primary energy source. Both the placement and orientation of the panels must account for the Sun's direction and the resulting shadows to ensure adequate power generation throughout the lunar day.

2.6 Meteorites

The meteoritic environment represents an additional critical factor for operations on the lunar surface. In the absence of a significant atmosphere, the Moon's surface is directly exposed to the continuous bombardment of solid particles of extraterrestrial origin, ranging from micro-metric dust to larger bodies. Unlike what occurs on Earth, where most meteoroids are destroyed or slowed down during atmospheric entry, on the Moon these particles impact the surface without experiencing significant deceleration.

From an engineering standpoint, the most relevant component is represented by micrometeorites, i.e., particles generally smaller than a millimetre but characterized by extremely high velocities. Their average velocity ranges between 13 km/s to

18 km/s, with peaks exceeding 70 km/s. Despite their small mass, the high kinetic energy associated with such velocities makes these impacts potentially damaging for exposed surfaces and structural components. The flux of particles with masses greater than one microgram is approximately $4.7 \times 10^{-8}/(\mathrm{m}^2\,\mathrm{s})$, corresponding to an average of about 1.48 impacts per year for each square meter of exposed surface (Figure 2.1) [18]. The micrometeorite flux on the lunar surface is relatively constant over time, with variations mainly related to the Moon's orbit and the presence of periodic meteor showers. However, the dominant contribution comes from a continuous background of interplanetary particles.

Another important aspect to consider is the generation of secondary particles resulting from impacts. When a micrometeorite strikes the surface, a portion of the material is ejected at high velocity as ejecta. These secondary particles can in turn impact nearby surfaces, amplifying the overall erosive effect and increasing the likelihood of damage to sensitive components.

In the context of long-duration missions, the cumulative effect of micrometeoritic bombardment becomes particularly significant. Even in the absence of catastrophic impacts, the progressive degradation of materials can compromise system performance over time. The severity of an impact is strongly dependent on the criticality of the affected component; therefore, appropriate mitigation measures should be identified and implemented based on a thorough risk assessment process [15].

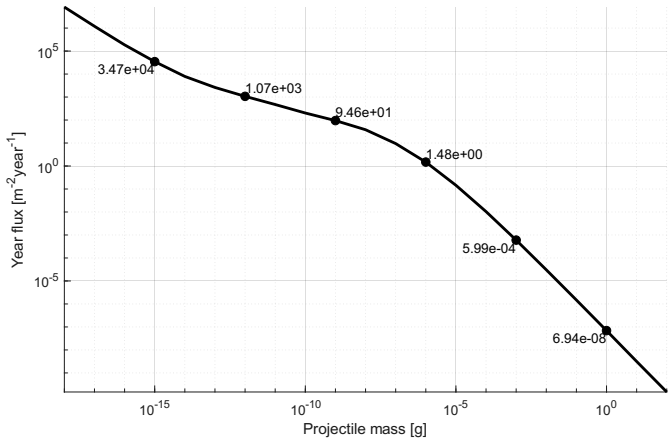

Figure 2.1: Meteoroid flux as a function of projectile mass

Chapter 3

Functions of the structure

3.1 Loads

The study of the loads acting on the structure represents a fundamental step in the structural sizing process. In the aeronautical field, this phase is often bypassed, as the loads to which the aircraft will be subjected during its operational life are well known. In the space domain, however (especially for missions that have never been performed before, such as the one considered in this work) it is essential to identify the forces acting on the structure throughout its lifetime. Consequently, it is necessary to identify not only the individual loads, but also the manner in which they are combined when acting simultaneously.

Three main phases are analysed:

- Ground testing;
- Launch;
- Operations in the lunar environment.

During the construction and testing phase of the rover on Earth, the loads acting on the system include Earth gravity ($g = 9.81\,\mathrm{m/s^2}$), internal pressurization ($\Delta p = 101{,}325\,\mathrm{Pa}$) and sudden accelerations due to the braking system in the longitudinal direction ($a_L = 5\,\mathrm{m/s^2}$) or vertical accelerations due to bumps or obstacles ($a_V = 10\,\mathrm{m/s^2}$), as estimated by Aldo Saponaro in his master's thesis *Development of a modular multi-DOF motion simulator for a pressurized lunar rover*, considering a geometry and payload similar to the final design [19].

Regarding the launch environment, it is assumed that the Falcon Heavy (FH) will be used, as it currently represents an excellent option among the launch vehicles available on the market. In fact, although no official data is available regarding the maximum transferable mass to the Moon, the maximum declared payload

deliverable to Mars is 16,800 kg. Since the Δv required to reach the Moon is lower than that needed to reach Mars, and because payload mass decreases as Δv increases, a conservative estimate of 16,800 kg is adopted as the maximum mass. This estimate also neglects the effects of interfaces between the rover and the launcher, as well as the presence of a landing module. Regarding maximum size, the FH fairing has an external diameter of 5.2 m and a total length of 13.2 m (increasable up to 18.7 m with the extended fairing); its internal dimensions are shown in Figure 4.13, while the flight envelope of Falcon Heavy is illustrated in Figure 3.1 [20]. As can be observed, for the heaviest payload class the maximum axial acceleration reaches 6 g, which will be combined with a lateral acceleration of 0.5 g. On the other hand, the maximum lateral acceleration is up to 2 g, combined with an axial one of 3.5 g. A static analysis will be performed in both these load conditions. For launch phase, the rover is considered unpressurised and at full mass.

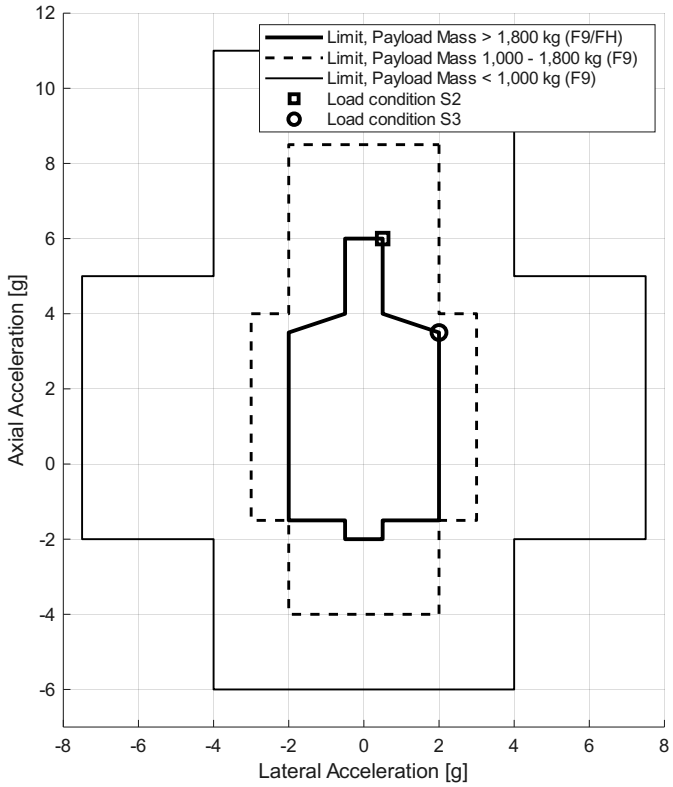

Figure 3.1: Falcon Heavy flight envelope for different payload mass ranges

Finally, the loads acting during the operational phase on the lunar surface include lunar gravity ($g_L = 1.622\,\mathrm{m/s^2}$), internal pressurization and acceleration due to manoeuvrers during operations, as previously described. Pressurization on

the Moon is assumed to take place within an existing local base; therefore, this scenario corresponds to a relatively advanced stage of lunar colonization. This assumption avoids combining launch loads with pressurization loads, which would otherwise result in significantly higher stresses on the external shell.

In summary, the analyses performed include three static analyses, one corresponding to the ground-test configuration (S1) and two representing the launcher acceleration conditions, each characterized by different acceleration levels (S2 and S3), as well as a modal analysis aimed at determining the natural frequencies of the rover (M1). The analysis under lunar operational conditions can be omitted, since the loads involved are the same as those in the ground-testing case, except for gravity, which is significantly lower than on Earth.

3.2 Composition of the structure

The structure of a pressurized rover must satisfy the following fundamental functions:

1. Ensure the structural integrity of the rover, allowing the mission to be carried out safely;

2. Protect the crew and the onboard subsystems from hazardous environmental events.

The first category includes the principal function of the primary structure, which is responsible for withstanding the mechanical loads imposed by the mission. The second category consists of the thermal insulation layer, the meteoroid and debris shield and the radiation absorption layer.

An example of the structural layering is shown in Figure 3.2. The MMOD shield is positioned on the outer side of the rover to protect the underlying layers from high-energy micrometeoroid impacts. Beneath it, the thermal insulation layer ensures the survivability of the main structure under the extreme thermal conditions typical of a lunar mission. The primary structure is then located under the insulating layer.

Placing the primary structure below the thermal insulation also provides protection against highly variable thermal loads, which could otherwise increase the stress levels developing within the material. In fact, severe and repeated sudden thermal variations over time can induce material fatigue and lead to the initiation of cracks in the shell. In addition, this configuration enables the use of materials characterized by a higher Ductile-to-Brittle Transition Temperature (DBTT). This temperature, which is specific to each material, marks the transition from ductile behaviour (capable of undergoing plastic deformation and therefore absorbing energy) to brittle behaviour, which in this case results in sudden material failure.

The reason why the insulating layer is positioned behind the MMOD shield is that it exhibits very low resistance not only to micrometeoroid impacts but also to abrasion caused by lunar regolith dust, which would significantly degrade its insulating effectiveness. However, this does not represent a major issue, as the materials used for MMOD shields are typically aluminium alloys, which maintain high performance even at low temperatures.

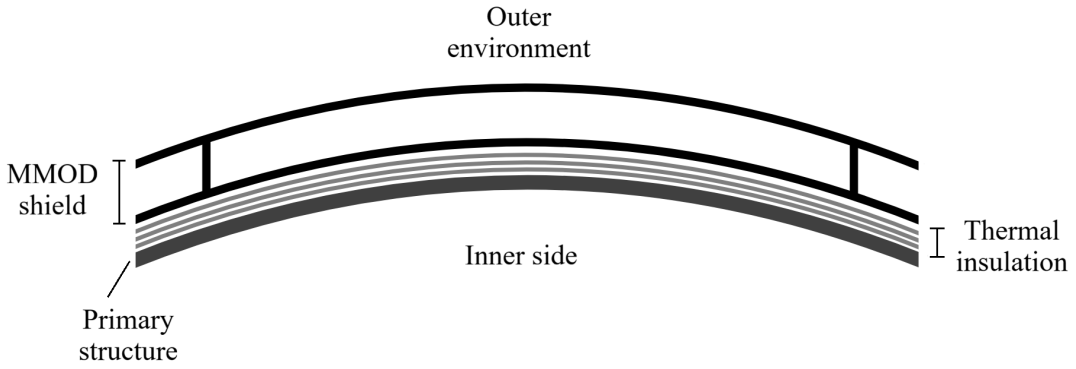

Figure 3.2: Example of the cross-section of the structure of a lunar pressurized rover

The primary focus of this work is the design of the rover's main structure, which will be addressed in detail in the following chapters. Here, a brief overview is provided of the most common strategies for shielding the rover from the harsh external environment, including extreme temperatures, micrometeoroid impacts, and space radiation.

3.2.1 Thermal insulation

The passive thermal control system must ensure a thermal environment compatible with crew life and allow all planned operations to be carried out without causing discomfort to the crew throughout the entire mission. It must maintain an internal cabin temperature between 18 °C and 27 °C [21].

The range of external temperatures on the Moon is extremely wide and depends on several factors, including the region being explored, solar illumination, and the time of year. Since this study focuses on a preliminary theoretical design without a specific mission scenario, only the extreme cases will be considered (Table 2.1):

- Hot case: 396 K (equatorial region in daylight);
- Cold case: 40 K (permanently shadowed polar craters).

MLI

The Multi Layer Insulation system is one of the most widely used and studied approaches in space applications, because it is specifically designed to reduce radiative heat transfer under vacuum or near-vacuum conditions, such as those on the Moon. A typical MLI blanket consists of alternating layers of very thin reflective films, usually plastic films metallized on one or both sides, and low-conductivity spacers (Figure 3.3).

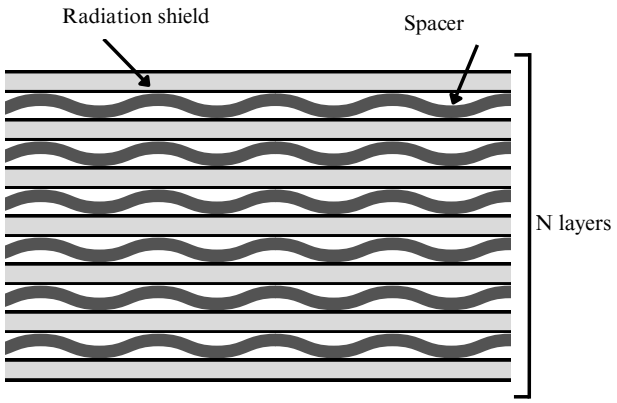

Figure 3.3: MLI cross-section showing N layers of alternating radiation shields and spacers

The physical principle behind MLI is reducing thermal radiation emission and absorption between surfaces at different temperatures: each layer reflects part of the radiative heat flux, and the presence of multiple layers creates temperature drops between adjacent surfaces, thus reducing the net energy flow. This mechanism effectively suppresses radiative heat transfer, which dominates in the absence of air, while the spacers limit conductive heat flow through the layers. This is achieved through the use of materials with very low thermal conductivity, combined with netted geometries that minimize the contact area between two adjacent layers. Heat transfer through residual gas in the spacers can be neglected if the air pressure is less than 1×10^{-5} mmHg, a condition verified on the lunar surface.

The most common plastic films used are *Mylar*, *Teflon*, and *Kapton*, onto which a metal layer is deposited (typically silver, aluminium or gold). Aluminium is preferred due to its relative low material and deposition costs, with a low emissivity ($\varepsilon = 0.03$), although it is slightly higher than that of silver and gold ($\varepsilon = 0.02$). Polyester net is typically used as a spacer to minimize the solid fraction and thus reduce conduction between layers; *Dacron* is commonly employed for this purpose [22].

A theoretical framework can be obtained as follows: starting from the internal energy balance for a compressible continuum,

$$\rho \frac{De}{Dt} = -\nabla \cdot \mathbf{q} + \boldsymbol{\sigma} : \nabla \mathbf{U} + \dot{q}_v \tag{3.1}$$

where

- ρ is the density;
- $\dfrac{D}{Dt}$ denotes the material derivative;
- e is the specific internal energy;
- $\mathbf{q}$ is the heat flux vector;
- $\boldsymbol{\sigma}$ is the Cauchy stress tensor;
- $\mathbf{U}$ is the velocity vector field;
- $\dot{q}_v$ is the volumetric heat generation rate per unit volume.

Assuming the Cauchy stress decomposition $\boldsymbol{\sigma} = -p\mathbf{I} + \boldsymbol{\tau}$, we obtain

$$\rho \frac{De}{Dt} = -\nabla \cdot \mathbf{q} + (-p\mathbf{I} + \boldsymbol{\tau}) : \nabla \mathbf{U} + \dot{q}_v \tag{3.2}$$

Expanding the double contraction,

$$\rho \frac{De}{Dt} = -\nabla \cdot \mathbf{q} - p(\mathbf{I} : \nabla \mathbf{U}) - \boldsymbol{\tau} : \nabla \mathbf{U} + \dot{q}_v \tag{3.3}$$

Using the tensor identity $\mathbf{I} : \nabla \mathbf{U} = \nabla \cdot \mathbf{U}$,

$$\rho \frac{De}{Dt} = -\nabla \cdot \mathbf{q} - p\nabla \cdot \mathbf{U} + \boldsymbol{\tau} : \nabla \mathbf{U} + \dot{q}_v \tag{3.4}$$

Introducing Fourier conduction and the radiative contribution, with constitutive relation $\mathbf{q} = -k\nabla T + \mathbf{q}_{\text{rad}}$,

$$\rho \frac{De}{Dt} = -\nabla \cdot (-k\nabla T + \mathbf{q}_{\text{rad}}) - p\nabla \cdot \mathbf{U} + \boldsymbol{\tau} : \nabla \mathbf{U} + \dot{q}_v \tag{3.5}$$

Expanding the divergence and assuming constant thermal conductivity k,

$$\rho \frac{De}{Dt} = \nabla \cdot (k\nabla T) - \nabla \cdot \mathbf{q}_{\text{rad}} - p\nabla \cdot \mathbf{U} + \boldsymbol{\tau} : \nabla \mathbf{U} + \dot{q}_v \tag{3.6}$$

Viscous dissipation defined by $\boldsymbol{\tau} : \nabla \mathbf{U} = \mu\phi$ is introduced,

$$\rho \frac{De}{Dt} = \nabla \cdot (k \nabla T) - \nabla \cdot \mathbf{q}_{\text{rad}} - p \nabla \cdot \mathbf{U} + \mu\phi + \dot{q}_v \tag{3.7}$$

Using the relation $e = cT$:

$$\rho c \frac{DT}{Dt} = \nabla \cdot (k \nabla T) - \nabla \cdot \mathbf{q}_{\text{rad}} - p \nabla \cdot \mathbf{U} + \mu\phi + \dot{q}_v \tag{3.8}$$

Finally, expanding the material derivative $\frac{DT}{Dt} = \frac{\partial T}{\partial t} + \mathbf{U} \cdot \nabla T$,

$$\rho c \left(\frac{\partial T}{\partial t} + \mathbf{U} \cdot \nabla T \right) = \nabla \cdot (k \nabla T) - \nabla \cdot \mathbf{q}_{\text{rad}} - p \nabla \cdot \mathbf{U} + \mu\phi + \dot{q}_v \tag{3.9}$$

Starting from this general equation, the following assumptions are made:

- Steady-state conditions $\left(\dfrac{\partial T}{\partial t} = 0 \right)$;
- Absence of convection ($\mathbf{U} = 0 \;\Rightarrow\; \rho c (\mathbf{U} \cdot \nabla T) = 0$);
- No compression ($-p \, \nabla \cdot \mathbf{U} = 0$);
- No viscous dissipation ($\mu\phi = 0$);
- No volumetric heat source ($\dot{q}_v = 0$).

Under these assumptions, the governing equation reduces to:

$$\nabla \cdot (k \nabla T) = \nabla \cdot \mathbf{q}_{\text{rad}} \tag{3.10}$$

Simplifying the problem to a one-dimensional model along the x coordinate:

$$\frac{\partial}{\partial x} \left(k \, \frac{\partial T}{\partial x} \right) = \frac{\partial q_{\text{rad}}}{\partial x} \tag{3.11}$$

Equation (3.11) is discretised over a stack of N reflective shields separated by spacers of uniform thickness δ (Figure 3.4). Integrating both sides over the control volume of the i-th internal node, between $x_{i-1/2}$ and $x_{i+1/2}$:

$$\int_{x_{i-1/2}}^{x_{i+1/2}} \frac{\partial}{\partial x} \left(k \, \frac{\partial T}{\partial x} \right) dx = \int_{x_{i-1/2}}^{x_{i+1/2}} \frac{\partial q_{\text{rad}}}{\partial x} \, dx \tag{3.12}$$

Applying the fundamental theorem of calculus to both sides:

$$\left[k \, \frac{\partial T}{\partial x} \right]_{x_{i-1/2}}^{x_{i+1/2}} = \left[q_{\text{rad}} \right]_{x_{i-1/2}}^{x_{i+1/2}} \tag{3.13}$$

Recognising the conductive flux $q_{\text{cond}} = k\,\partial T/\partial x$ evaluated at the two faces of the control volume, and expanding the boundary terms:

$$q_{\text{cond},i} - q_{\text{cond},i-1} = q_{\text{rad},i} - q_{\text{rad},i-1} \tag{3.14}$$

This expresses the steady-state condition that the total net flux entering node i is zero. Approximating the conductive fluxes with central finite differences across each spacer of uniform thickness δ:

$$q_{\text{cond},i} = k\,\frac{T_{i+1} - T_i}{\delta}, \qquad q_{\text{cond},i-1} = k\,\frac{T_i - T_{i-1}}{\delta} \tag{3.15}$$

Substituting Eq. (3.15) into Eq. (3.14) yields the nodal energy balance:

$$k\,\frac{T_{i+1} - T_i}{\delta} + k\,\frac{T_{i-1} - T_i}{\delta} + \Big(q_{\text{rad},i-1} - q_{\text{rad},i}\Big) = 0, \qquad i = 2, \ldots, N+1 \tag{3.16}$$

where $k = k_{\text{sp}}$ is the effective through-thickness conductivity of the Dacron spacer, since the conductive heat flux contribution associated with the reflective layers is neglected.

The radiative flux between two adjacent grey parallel surfaces i and $i+1$, assuming a unit view factor, follows the classical grey-body exchange relation [23]:

$$q_{\text{rad},i} = \frac{\sigma\Big(T_i^4 - T_{i+1}^4\Big)}{\dfrac{1}{\varepsilon_i} + \dfrac{1}{\varepsilon_{i+1}} - 1} \tag{3.17}$$

Dirichlet boundary conditions are imposed by considering the minimum admissible temperature difference within the requirements:

- Hot case:
$$T_1 = T_{\text{in}} = 300\,\text{K}, \qquad T_{N+2} = T_{\text{out}} = 400\,\text{K}; \tag{3.18}$$
- Cold case:
$$T_1 = T_{\text{in}} = 291\,\text{K}, \qquad T_{N+2} = T_{\text{out}} = 40\,\text{K}. \tag{3.19}$$

Writing Eq. (3.16) for every internal node $i = 2, \ldots, N+1$ produces a non-linear algebraic system $F(T) = 0$ of size N. Because q_{rad} depend on the unknown temperatures, the system is solved with an outer fixed-point iteration.

In Figures 3.5 and 3.6, the results for the hot and cold cases are shown, respectively, using the material properties reported in Table 3.1 [24]. The thermal conductivity of the Dacron spacer mesh is not available in the literature and was therefore assumed to be $k_{sp} = 2 \times 10^{-5}\,\text{W/(m K)}$.

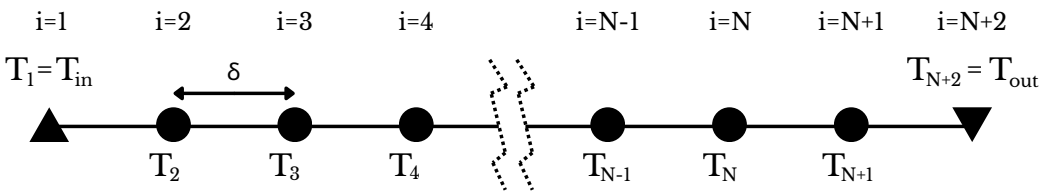

Figure 3.4: MLI simplified node model; each node represents a reflective layer

Using these curves obtained from the model, it is possible to properly size the MLI, selecting the number of layers required to maintain the outgoing thermal flux (as in the cold case) in thermal equilibrium with the internally generated heat. However, since the reference mission for this work is not fully defined in terms of thermal aspects, the hot case must also be considered. Therefore, a trade-off is necessary, balancing the total mass of the MLI with any additional active temperature control systems, while staying within the margins imposed by the requirements.

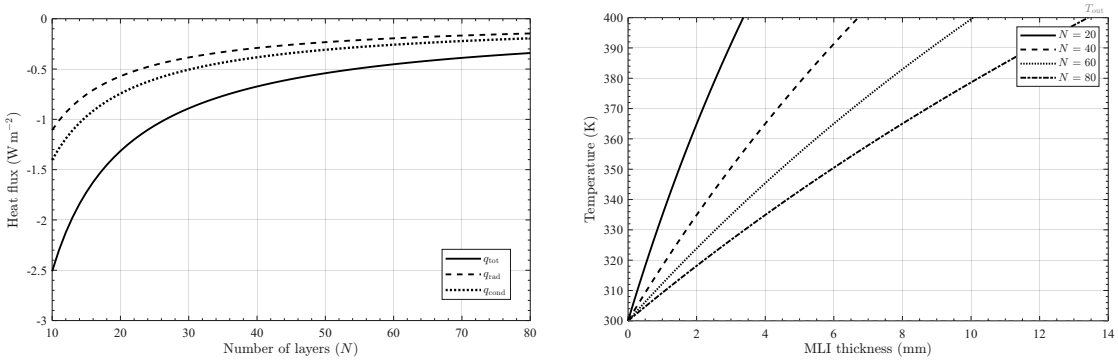

(a) Heat flux **(b)** Temperature in MLI thickness

Figure 3.5: MLI Hot case heat flux and temperature through thickness

The benefits of employing an MLI system are evident from its extremely low areal mass and minimal thickness, as illustrated in Figure 3.7. Typically, up to 60 layers are used, corresponding to an areal mass of $0.105\,\mathrm{kg/m^2}$. For an external surface of $65\,\mathrm{m^2}$, the total mass of this passive system alone would be $6.825\,\mathrm{kg}$.

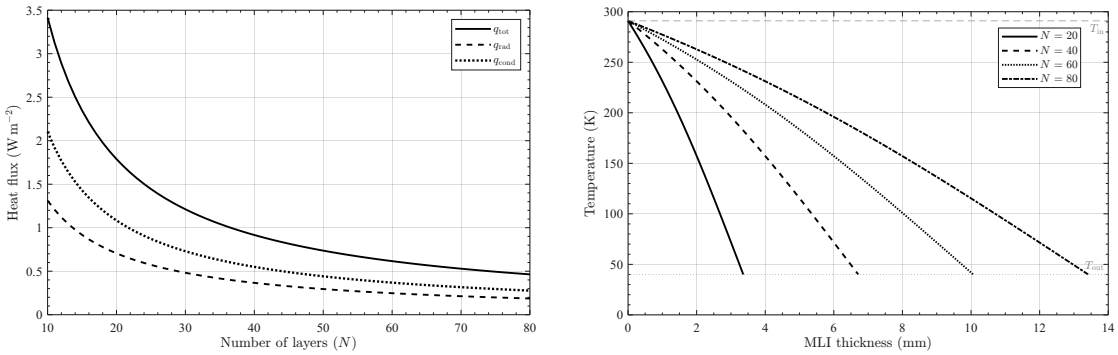

(a) Heat flux **(b)** Temperature in MLI thickness

Figure 3.6: MLI Cold case heat flux and temperature through thickness

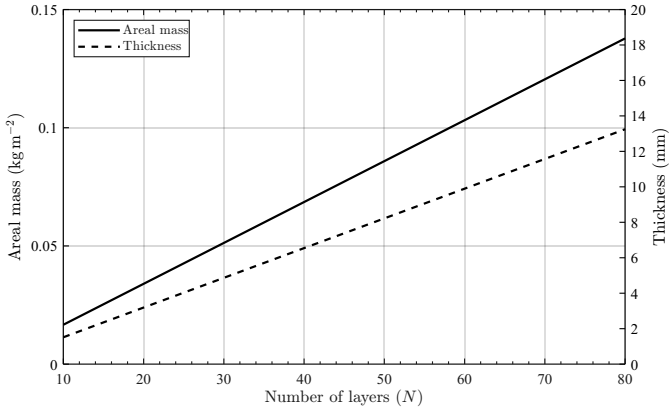

Figure 3.7: Areal mass and thickness of the MLI as a function of the number of layers

Table 3.1: Material properties of the MLI spacers and reflective foils

Component	**Property**	**Value**	**Unit**
Reflector layer	Material	Double aluminized Kapton	–
	Thickness	0.0076	mm
	Areal weight	11	g/m^2
	Emissivity ε	0.03	–
Spacer	Material	Dacron	–
	Thickness	0.16	mm
	Mesh density	7.8	meshes/cm^2
	Areal weight	6.3	g/m^2

Aerogel

Another advanced isolation technique consists of using a cover in aerogel. Aerogels are materials with extremely low density that can be employed in a wide range of applications. In the case of silica aerogels, they provide exceptionally low thermal conductivity. They are a porous nanostructured form of silicon dioxide, characterized by a very low thermal conductivity ($\sim$0.015 W/(m K)) and an extremely low density ($\sim$100 kg/m^3). This material has been demonstrated to be the solid with the lowest thermal conductivity measured under atmospheric pressure conditions.

Their insulating performance is based on two main mechanisms of heat transfer reduction:

1. Limitation of solid conduction, because the structure consists mostly of voids and the solid paths are highly tortuous and poorly connected;

2. Limitation of gas convection inside the pores, since the pore size is often smaller than the mean free path of gas molecules (λ), thereby reducing the effectiveness of heat transfer via molecular collisions [25]. The mean free path is defined as the average distance a particle travels between successive collisions. The ratio between this length and the characteristic length of the surrounding medium (e.g., the average pore size in silica aerogel) is known as the Knudsen number (Kn). When $Kn > 1$, collisions of particles with the pore walls occur more frequently than collisions among particles. This phenomenon, known as Knudsen diffusion, further limits the thermal conductivity [26].

$$Kn = \frac{\lambda}{L} \tag{3.20}$$

Silica aerogels, despite being fragile and brittle and thus unsuitable for bearing mechanical loads, have been successfully employed in planetary missions where their exceptional thermal insulation properties are advantageous. They were selected by NASA for the *Sojourner* rover in the *Pathfinder* mission and later for the Mars Exploration Rovers *Spirit* and *Opportunity* [27]. In these missions, the presence of a thin Martian atmosphere renders MLI far less effective due to convective heat transfer, whereas aerogel insulation outperforms MLI under such conditions [27].

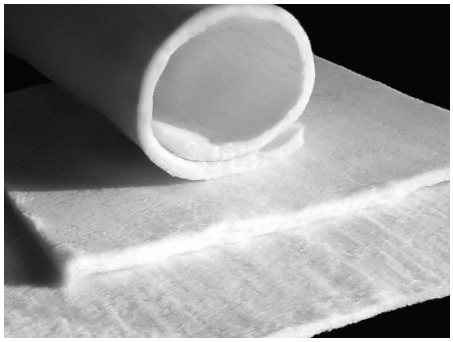

Figure 3.8: Example of Silica aerogel cover

3.2.2 MMOD shield

The main micrometeoroid shielding technique is the Whipple Shield (WS), which consists of two impact-absorbing layers separated by a stand-off distance (Figure 3.10) [28]. The front wall (or bumper) is sacrificial and can be perforated by the projectile; if this occurs, the projectile is fragmented into smaller pieces that expand radially while traversing the stand-off region and impact the rear wall over a larger area. The role of the rear wall is to absorb the impact of these fragments without being perforated. One of the most important parameter in MMOD shield designing is the ballistic limit, which is defined as the critical projectile diameter beyond which the protective shield is penetrated. Some of the most common materials used for a WS are reported in Table 3.2.

The preliminary design of a Whipple Shield is based on empirical equations [29]. For protection against a high-speed projectile impact ($V_n \geq 7\,\mathrm{km/s}$), the bumper thickness t_b is given (in cm) by

$$t_b = \frac{c_b m_p}{\rho_b} = c_b\, d\, \frac{\rho_p}{\rho_b} \tag{3.21}$$

where the coefficient $c_b = 0.25$ for $S/d < 30$ and $c_b = 0.20$ for $S/d \geq 30$, S is the stand-off distance between the bumper and the rear wall (cm), d is the projectile diameter (cm), m_p is the projectile areal density (g/cm^2), ρ_b is the bumper density (g/cm^3), and ρ_p is the projectile density (g/cm^3).

The rear wall thickness t_w (in cm) is given by

$$t_w = c_w \sqrt{d}\,(\rho_p \rho_b)^{1/6}\, M_p^{1/3} \frac{V_n}{\sqrt{S}} \sqrt{\frac{70}{\sigma}} \tag{3.22}$$

where the coefficient $c_w = 0.16\,\mathrm{cm^2 s/g^{2/3} km}$, M_p is the projectile mass (g), V_n is the normal component of the projectile velocity (km/s), defined as $V_n = V \cos\theta$, θ

is the impact angle (considering $\theta = 0°$ the angle normal to the bumper), and σ is the yield strength of the rear wall material (ksi).

The curves are shown in Figure 3.9 as a function of the projectile diameter, considering $\rho_p = 2.50\,\mathrm{g/cm^3}$, $\rho_b = 2.71\,\mathrm{g/cm^3}$, $\sigma = 40\,\mathrm{ksi}$, $S = 15\,\mathrm{cm}$, $V_n = 15.5\,\mathrm{km/s}$ and a spherical shape for the projectile.

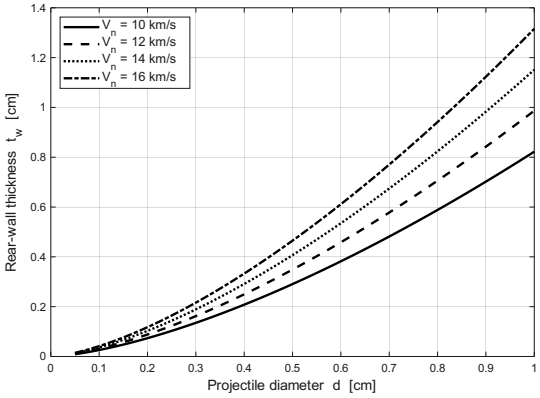

(a) Rear wall thickness - parametric in projectile velocity

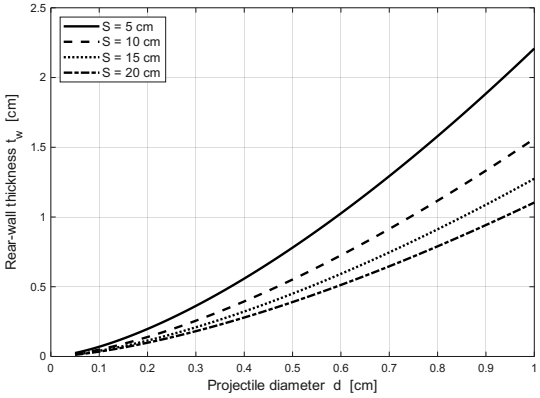

(b) Rear wall thickness - parametric in stand-off distance

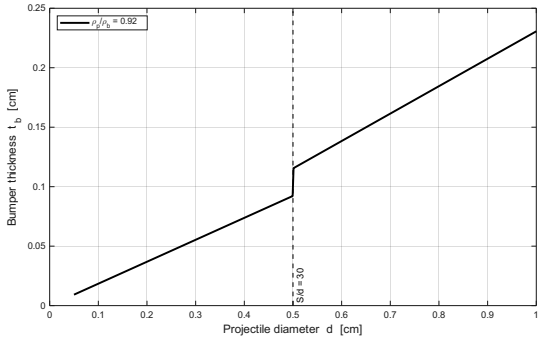

(c) Bumper thickness

Figure 3.9: Bumper and rear wall thicknesses of WS as a function of the projectile diameter

It is important to ensure an adequate stand-off distance, since, as can be observed from Figure 3.9b, it contributes to reducing the rear-wall thickness and therefore the overall mass. However, the dependence on this parameter follows a square-root trend; consequently, excessively increasing the stand-off is not advantageous, as the resulting benefit becomes marginal while leading to a penalty in terms of overall volume.

Table 3.2: Physical and mechanical properties of materials used as bumper and rear wall [30]

Material	**Alloy/Model**	**Density (g/cm^3)**	**Yield Strength (MPa)**	**Modulus of Elasticity (GPa)**
Aluminium	6061	2.70	276	68.9
	2024	2.78	345	73.1
	2017	2.79	276	72.4
	7075	2.80	572	71.7
	2219	2.82	290	73.1
Titanium	Ti-6242	4.42	883	113.8
CFRP	HMF371-7714B	1.80–1.85	–	69.1–69.5

An evolution of this concept is the Stuffed Whipple Shield (SWS), in which fibrous layers are inserted within the stand-off region to further reduce the impact energy. Configurations employing multiple bumpers followed by a rear wall are referred to as Multi-Shock Shields (MSS). Another variant is the Mesh Double Bumper (MDB), consisting of a metallic mesh bumper followed by metallic and composite bumpers; this configuration (Figure 3.11c) has been shown to be more mass-efficient for both 90° and 45° impact angles, saving up to 70% of weight in respect to WS [31].

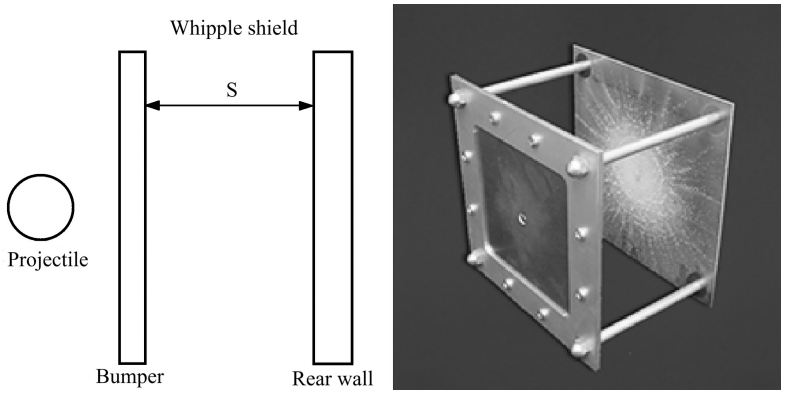

Figure 3.10: Diagram (left) and specimen (right) of a Whipple shield

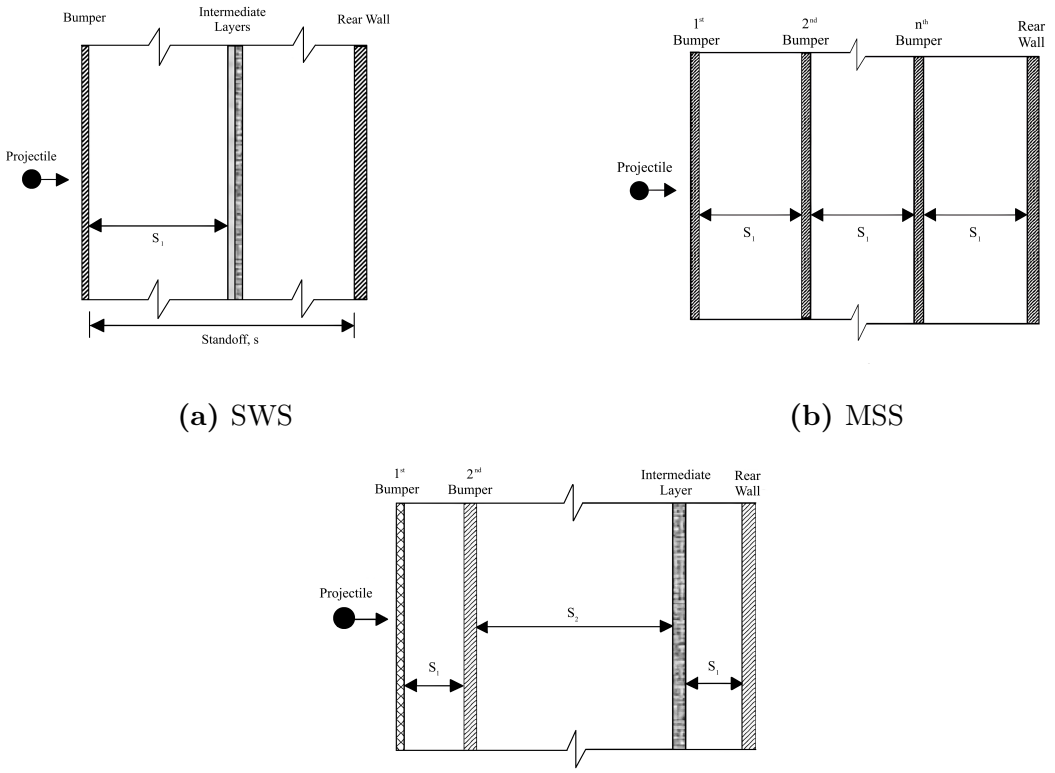

(a) SWS

(b) MSS

(c) MDB

Figure 3.11: Evolved MMOD shields: SWS, MSS, MDB [30]

An alternative class of micrometeoroid shields is represented by Honeycomb Core Sandwich Panels (HCSP), which consist of metallic skins and a metallic honeycomb core. While they offer superior structural strength, their shielding capability is generally lower than that of Whipple-type shields, as the honeycomb core restricts the radial expansion of debris, causing the fragments to impact the rear skin over a smaller area causing more damage. This channelling effect is contrasted by placing the honeycomb cells perpendicular to the direction of the debris [32]. A similar concept is the Foam Core Sandwich Panel (FCSP), in which the honeycomb core is replaced by an isotropic metallic foam. FCSPs exhibit structural properties comparable to those of HCSPs, while providing improved shielding performance. An example of these configurations is shown in Figure 3.12. In some designs, the solid core can also be replaced by a fluid (either liquid or gaseous) to further enhance the impact mitigation capability [33].

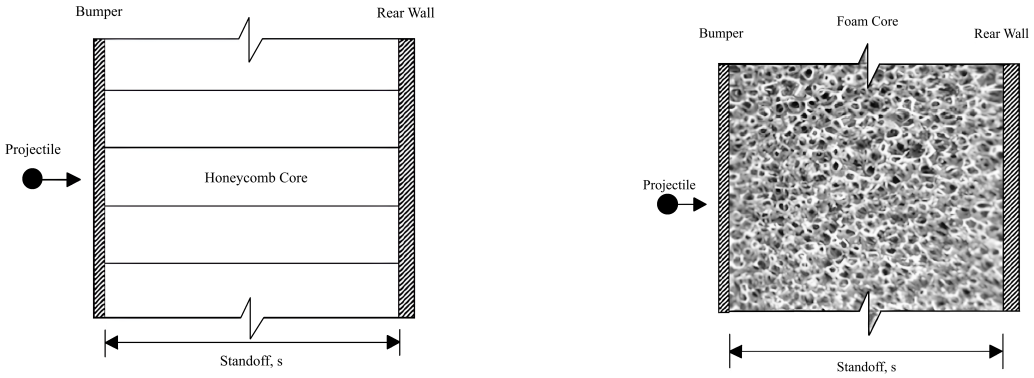

(a) HCSP **(b)** FCSP

Figure 3.12: Alternative MMOD shields: HCSP, FCSP [30]

The materials most commonly used for the front wall are aluminium alloys, among which Al6061-T6 is the most extensively studied and widely adopted. Alternatively, titanium alloys can be considered. Of particular interest are hybrid configurations combining titanium, aluminium, and nylon, which demonstrate superior performance compared to monolithic aluminium bumpers. These configurations generate higher shock pressures and induce larger temperature rises upon impact, thereby enhancing projectile fragmentation [34].

A possible material suitable for this application is Nextel ceramic fabric, a fibrous material characterized by density and impact resistance comparable to aluminium. Its main advantage is that, upon impact, it does not generate secondary debris (fragments of the bumper generated by the projectile impact) that could damage the rear wall of the shield. An additional benefit is its intrinsic flexibility, which allows the material to be deployed during operation. This feature is particularly advantageous for inflatable structures and for for complex geometries. For instance, it could be employed to shield flexible junction regions, such as the connection between the front and rear sections of the rover using a modular configuration.

The use of self-healing materials for micrometeoroid shielding can also be considered, as they can partially or fully repair damage from impact. However, these materials were not specifically developed for space applications, and experimental evidence is currently insufficient to validate their use in this scenario, resulting in a low Technology Readiness Level (TRL). In particular, extrinsic self-healing systems, where the healing agent is stored in microcapsules or capillaries and released upon impact, often require oxygen to initiate oxidation-based repair, which is absent on the lunar surface [30].

3.2.3 Radiation absorption

Radiation shielding effectiveness in space systems is typically evaluated in terms of areal density g/cm^2 rather than physical thickness. Increasing shielding thickness generally reduces radiation exposure; however, beyond a certain threshold the benefits diminish significantly. High-energy GCR particles penetrate deeply into materials and generate cascades of secondary particles, causing the dose reduction curve to flatten with increasing shielding depth.

The effectiveness of shielding materials against GCR is strongly dependent on their atomic composition and hydrogen content. Materials rich in hydrogen and composed of low-atomic-number elements are particularly effective because they reduce the production of harmful secondary radiation generated during nuclear interactions with high-energy cosmic particles. In this context, liquid hydrogen represents an ideal shielding material in terms of radiation attenuation. However, its practical use is highly challenging, as the handling and storage of liquid hydrogen require cryogenic temperatures, complex containment systems, and stringent safety measures.

Hydrogenous materials provide two major advantages for radiation mitigation:

- Fragmentation of heavy ions: hydrogen nuclei efficiently break up incoming high-energy ions into lighter fragments with reduced biological effectiveness;
- Reduced secondary particle production: low-Z elements generate fewer secondary neutrons and other energetic particles during nuclear interactions.

Radiation shielding is rarely implemented as a dedicated layer in mobile systems. Traditional structural materials such as aluminium, while effective at reducing dose equivalent, can paradoxically increase the biological risk from GCR, highlighting the need for an integrated mitigation strategy (Table 3.3). One of the most effective approaches is to use consumables and operational fluids as shielding material. Hydrogen-rich resources, including water tanks, waste storage and other essential life-support materials, can be strategically positioned around the crew compartment to increase the effective areal density of the shield. This method provides meaningful radiation protection without adding dedicated shielding mass, making it particularly suitable for pressurized lunar rovers where both weight and volume are highly constrained. [35].

Table 3.3: Annual GCR exposure behind various shields at 1997 solar minimum. Numbers in parenthesis are shield performances relative to aluminium values at the same thickness [35]

Shield	**Dose Equivalent, cSv***	**Excess Harderian Gland Tumor Risk, percent***
1.5148 g/cm^2		
Aluminum	130.9 (1.00)	3.57 (1.00)
TransHab	121.6 (1.08)	3.07 (1.16)
Polyethylene	113.1 (1.16)	2.64 (1.35)
5 g/cm^2		
Aluminum	113.9 (1.00)	3.37 (1.00)
TransHab	99.4 (1.15)	2.74 (1.24)
Polyethylene	86.4 (1.32)	2.20 (1.54)

* Unshielded, dose equivalent is 120 cSv and excess tumor risk is 2.23%.

Chapter 4

Structural sizing framework

4.1 Requirements

The primary structure is responsible for housing and protecting the crew and the onboard subsystems from the external environment.

- It shall be as lightweight as possible, as the structure mass strongly influences mission costs and limits the maximum transportable payload mass.
- It shall have a geometry suitable for withstanding the internal pressurization loads.
- It shall be functional in terms of rover manoeuvrability and efficient management of the internal layout.
- It shall withstand the various loads encountered throughout its lifetime, both during launch (surviving the launcher's accelerations and vibrations without damage) and during the testing and operational phases.
- It shall comply with the launcher mass and envelope constraints, in order to allow manufacturing, integration and testing on Earth, as well as launch the entire rover in a single mission.

The requirements described here are addressed in detail in Section 4.5.

4.2 Shape

Pressure vessels are structures designed to contain fluids at a pressure significantly different from that of the surrounding environment. The geometry of the vessel plays a fundamental role in determining its structural efficiency and the stress distribution

over its surfaces. It is well known that geometries characterized by continuous curvature, such as spheres, cylinders, and toroids, are optimal for containing pressure loads, whereas geometric discontinuities such as sharp corners and sudden changes in cross-section introduce potentially critical stress concentrations, i.e. regions where local stresses are significantly higher than the average membrane stress. From a mechanical standpoint, such discontinuities interrupt the regular flow of stress trajectories, locally inducing complex stress states.

Within the framework of linear elasticity theory, sharp corners are associated with stress singularities, for which the theoretical stress value tends to infinity as the fillet radius approaches zero. In real materials, this behaviour results in localized plastic deformation, crack initiation, or delamination in case of composite materials, leading to a drastic reduction in the load-carrying capacity of the structure.

In pressure vessels, these effects are particularly critical because the pressure load acts continuously and uniformly over the entire surface. Consequently, even small geometric imperfections or local discontinuities may govern the structural collapse mechanism.

In thin-walled pressure vessels, internal pressure primarily generates in-plane stresses acting along the surface. For doubly curved geometries, such as spheres or toroids, the pressure load is uniformly balanced in all directions, resulting in an isotropic stress state. A doubly curved surface is defined as a surface exhibiting curvature in two principal directions at every point and therefore cannot be developed onto a plane without distortion.

For a thin spherical vessel [36], the membrane stress can be derived from force equilibrium:

$$p\pi R^2 = \sigma_\theta \left[(R+t)^2 - R^2\right] \pi \tag{4.1}$$

$$\sigma_\theta = \frac{pR^2}{2Rt + t^2} \tag{4.2}$$

By applying the thin-wall assumption ($R \gg t$), which is valid when $R/t > 10$, the quadratic thickness term can be neglected, yielding:

$$\sigma_\theta = \frac{pR}{2t} \tag{4.3}$$

where p is the internal pressure, R the radius of the sphere, t the shell thickness, and σ_θ the hoop stress. Due to spherical symmetry, the meridional stress σ_ϕ is equal to the hoop stress, and therefore:

$$\sigma_\theta = \sigma_\phi = \frac{pR}{2t} \tag{4.4}$$

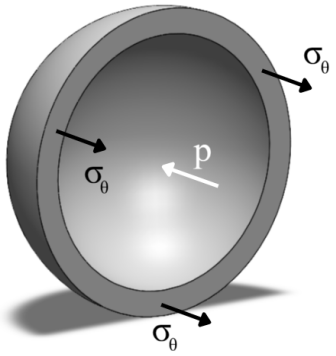

Figure 4.1: Sphere hoop stress diagram

For cylindrical shells, the two principal membrane stresses are the hoop stress and the axial stress. These stress components are again obtained from equilibrium considerations, where R is the cylinder radius, h the cylinder length, t the shell thickness, σ_θ the hoop stress, and σ_z the axial stress:

$$p\pi R^2 = \sigma_z \left[(R+t)^2 - R^2\right] \pi \tag{4.5}$$

$$\sigma_z = \frac{pR^2}{2Rt + t^2} \tag{4.6}$$

Applying the thin-wall assumption once more yields:

$$\sigma_z = \frac{pR}{2t} \tag{4.7}$$

Moreover, equilibrium in the circumferential direction gives:

$$p\,2Rh = \sigma_\theta\,2th \tag{4.8}$$

$$\sigma_\theta = \frac{pR}{t} \tag{4.9}$$

which is twice the stress present in an equivalent spherical vessel under the same pressure and thickness conditions. This classical result highlights how the sphere represents the most efficient geometry for minimizing pressure-induced stresses.

The advantage of curved geometries arises from the fact that curvature allows pressure loads to be transmitted as in-plane forces, thereby avoiding the development of bending moments. As a result, the structure operates predominantly in the membrane regime, which represents the most efficient load-bearing mechanism for thin shells.

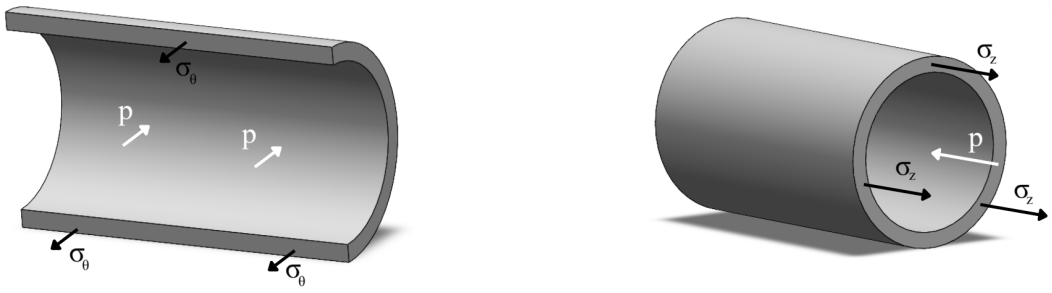

(a) hoop stress **(b)** axial stress

Figure 4.2: Cylinder stress diagram: hoop and axial stress

Constraints related to internal volume optimization and stability requirements, such as the location of the centre of mass, may require deviations from the ideal geometry. For this reason, shapes such as the ellipsoid (a generalization of the sphere), the elliptical cylinder with semi-ellipsoidal end caps, and the torus with an elliptical cross-section are considered. Furthermore, in order to introduce additional degrees of freedom and explore different configurations, each elliptical section of the aforementioned geometries may feature an upper semi-axis different from the lower one, as illustrated in Figure 4.3.

For the purposes of the present study, the analysis focuses primarily on cylindrical and ellipsoidal geometries, as these configurations are generally more suitable for relatively compact pressurized rovers intended mainly for transportation and exploration missions, which currently represent the most relevant applications. Nevertheless, toroidal pressurized environments, particularly for static surface bases, may become of interest in future developments, and the methodology presented here could be adapted to address such configurations as well.

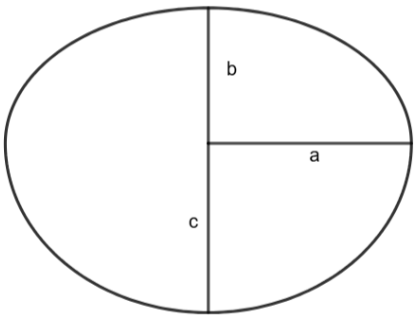

Figure 4.3: Double-ellipse cross-section shape

4.3 Materials

This section provides a brief discussion of the most commonly used materials for structural applications in the aerospace field and their main areas of use, with a perspective on potential future developments related to ISRU.

In a future scenario characterized by the presence of a stable and advanced lunar base, it is reasonable to foresee the extraction of raw materials directly on the Moon. This would make the establishment of local manufacturing facilities particularly attractive, enabling in-situ production of structural components and significantly reducing launch-related costs, which are extremely high. Moreover, this approach would allow the structure to be sized primarily for operational loads, which are considerably less severe than those experienced during launch.

Aluminium alloys are of particular interest, also due to the fact that aluminium is present in approximately 15% of the lunar regolith in the form of aluminium oxide (Al_2O_3). Among these, Al7075 and Al2024 alloys are widely used thanks to their superior strength properties and they can also be employed as skins for sandwich panels. The Al6061 alloy exhibits inferior mechanical properties and is therefore generally used for components subjected to lower stress levels; however, it offers advantages in terms of ease of manufacturing and lower costs.

Another material of interest is magnesium, which can be mined from olivine. Magnesium alloys could be particularly useful in meteoroid shielding due to their high vibration damping capacity, roughly thirty times that of aluminium, as well as their effectiveness against electromagnetic radiation. The main drawback of magnesium alloys is their brittleness at low temperatures (typical of the lunar night), an issue not present in Al–Li alloys.

Beryllium exhibits a high specific stiffness and good thermal properties; however, its use is limited due to its toxicity. Titanium alloys can replace aluminium alloys when higher performance is required, as they provide high strength and low thermal expansion, albeit at the cost of higher density. Similarly, stainless steels are often employed for bolts or small mechanical components that require high performance.

With regard to composite materials, they represent a promising alternative due to their superior structural performance compared to conventional materials, especially under extreme environmental conditions such as those encountered in space. Their properties strongly depend on fibre orientation and manufacturing processes. Fibres can be classified into high-modulus types, which are suitable for buckling-sensitive components, and high-strength types, typically used for elements subjected to high loads.

Composite materials can be classified into five main categories:

1. Organic matrix composites (e.g. graphite/epoxy, Gr/E), commonly used in inflatable structures or truss-based configurations;

2. Metal matrix composites (e.g. SiC/Al or Gr/Al), inherently resistant to harsh space environments but rarely used due to high production costs;

3. Ceramic matrix composites, which are non-brittle, refractory materials capable of withstanding severe thermo-mechanical and corrosive conditions, offering excellent strength characteristics;

4. Carbon fibre reinforced carbon (C/C), suitable for both internal and external load-bearing structural systems;

5. Polyimides (e.g. Kapton), belonging to the family of high-performance polymers and commonly used as insulating materials.

At present, metallic alloys are still preferred for primary load-bearing space structures due to the complexity involved in predicting the failure behaviour of composite materials. Consequently, a more conservative design approach based on well-characterized materials is often adopted. Nevertheless, composite materials clearly represent a highly attractive and competitive alternative for future space applications [37, 38].

In Table 4.1 it's possible to see some of the most common materials for space structures and their mechanical properties [37].

Table 4.1: Mechanical properties of typical materials for spacecraft

Material	**Density** (kg/m^3)	**Tensile strength** (MPa)	**Compressive yield stress** (MPa)	**Young's modulus** (GPa)	**Elongation** (%)
Aluminium					
2024-T3 sheet	2770	441	269	72	12
6061-T6 bar	2710	290	240	68	10
7075-T73 sheet	2800	460	380	71	8
Heat-resistant alloys					
A-286 bar	7940	970	660	201	12
Inconel 718 bar	8220	1280	1080	203	12
Magnesium					
AZ31B H24 sheet	1770	270	165	45	6
Titanium					
Ti-6Al-4V annealed plate	4430	900	855	110	10
Beryllium					
AMS 7906 bar	1850	320	–	290	2
Composite materials					
T800H/epoxy [0, ±45, 90]	1600	820	660[a]	60	–
Kevlar 49/epoxy [0, ±45, 90]	1400	500	150[a]	30	–
E-glass/epoxy [0, ±45, 90]	2200	300	300[a]	10	–

[a] Compressive strength.

Metals: MIL-HDBK-5H. Composites: typical data.

4.4 Methodology

The logic followed by the software is shown in Figure 4.5. Upon startup, the user must provide the input data related to the geometry, material, loads to be applied, safety factors used and the mesh size for the finite element discretization. The program has been designed to run on any machine with valid licenses for MSC Patran and MSC Nastran; compatibility is guaranteed with the most recent versions up to 2017.1. It was written in Matlab, which is particularly suitable for handling matrix data.

Once the user inputs the parameters defining the problem, the software generates a *session file*. This type of file contains all the instructions needed to build the geometric and mathematical model, and is written in Patran's proprietary language, Patran Command Language (PCL). It thus includes specifications for geometry, materials, finite element discretization, element properties, simulation of subsystem masses, applied loads, and imposed boundary conditions.

The session file is then executed in Patran, producing the Bulk Data File (BDF), which contains the description of the mathematical model and requests the desired outputs from Nastran. A BDF is generated for each required analysis, and each must be solved individually by Nastran, which provides an HDF5 as output for each case. This file is read by the software, as it contains all the useful information requested from the solver.

Finally, this data is collected into a matrix which, when read in the integrated post-processor, provides the user with trends showing how variations in the parameters of interest affect the system's response.

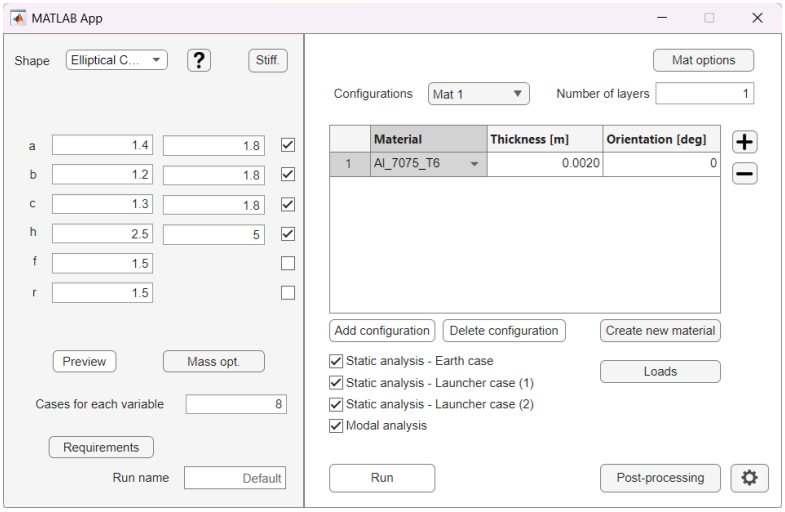

Figure 4.4: Graphical user interface of the program: selection of geometric parameters

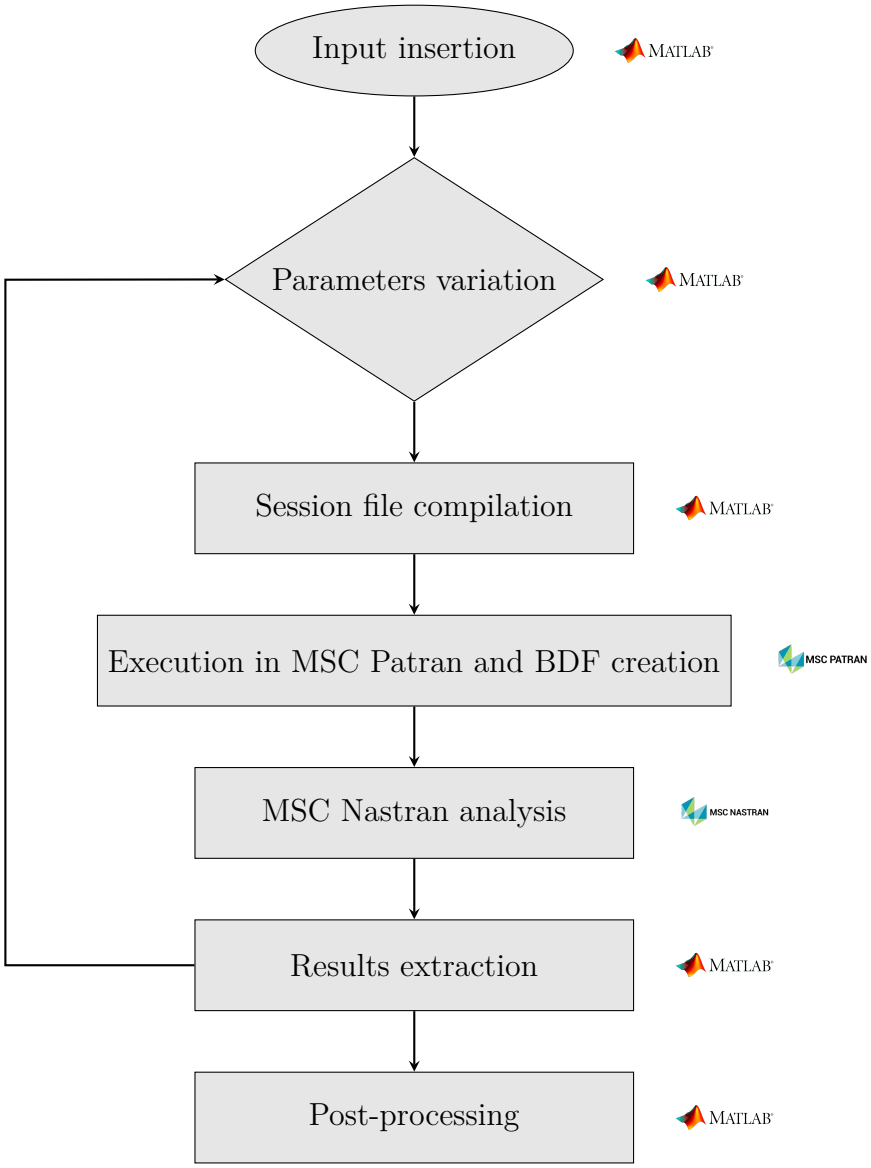

Figure 4.5: Framework flowchart. Each block shows the symbol of the corresponding software used

4.4.1 Parameters

The geometric parameters that can be varied are:

- a – Major semi-axis of the section;
- b – Upper minor semi-axis of the section;
- c – Lower minor semi-axis of the section;
- d – Distance between the centre of the section and the revolution axis;
- h – Length of the cylindrical segment;
- f – Semi-axis of the front ellipsoid;
- r – Semi-axis of the rear ellipsoid.

Table 4.2: Geometric parameters for the considered shapes

Parameter	Ellipsoid	Cylinder	Torus
a	X	X	X
b	X	X	X
c	X	X	X
d			X
h		X	
f		X	
r		X	

For a better understanding of the geometry and the parameters described, Figure 4.6 shows the schematic representation of the structure's framework.

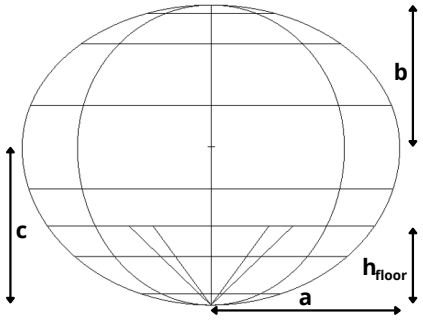

(a) Ellipsoid

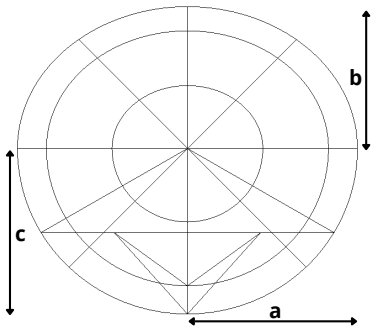

(b) Cylinder (front)

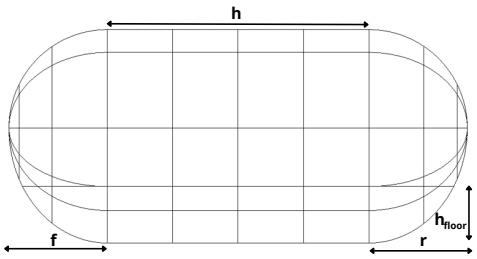

(c) Cylinder (side)

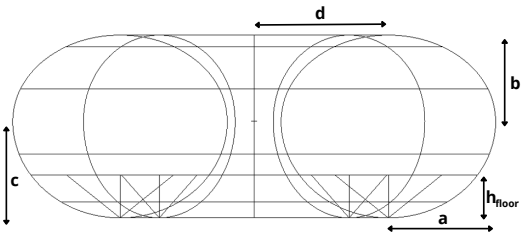

(d) Torus

Figure 4.6: Geometrical parameters for each shape: ellipsoid, cylinder and torus

Other possible geometry parameters (shown in Figure 4.7) are:

- n_{str} – Number of stringers (the stiffening elements parallel to the floor);
- n_{fr} – Number of frames (the stiffening elements perpendicular to the floor);
- $n_{fr,f}$ – Number of frames spaced with a constant angle on the front-end cap (only for cylinder);
- $n_{fr,r}$ – Number of frames spaced with a constant angle on the rear-end cap (only for cylinder);
- $n_{str,floor}$ – Number of additional floor stringers (the minimum number of floor stringers is 2 lateral and 1 central: if $n_{str,floor} = 1$, two additional stringers are placed at equal distance between the central and the lateral ones);
- h_{floor} – Height of the floor plane with respect to the rover base.

Regarding materials, isotropic or orthotropic properties can be defined by the user, or selected from the material library. These materials may be assigned either to isotropic plates or to laminates defined within the model. Each structural element must be associated with a material. These elements are:

- Outer shell;
- Stringers;
- Frames;
- Floor;
- Floor stiffeners;
- Floor pillars.

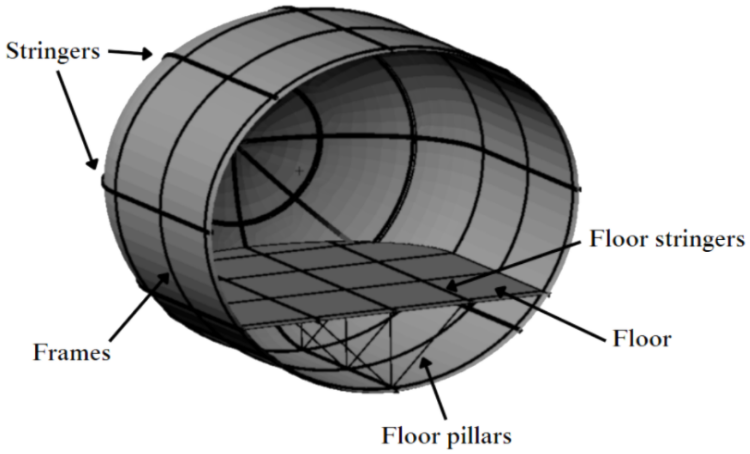

Figure 4.7: Cylindrical rover section

Furthermore, regarding beam elements, which are stringers, frames, floor stiffeners, and floor pillars, additional parameters correspond to the dimensions of their cross-sections. The possible cross-section types shown in Figure 4.8 have been defined, along with the associated parameters that can be varied.

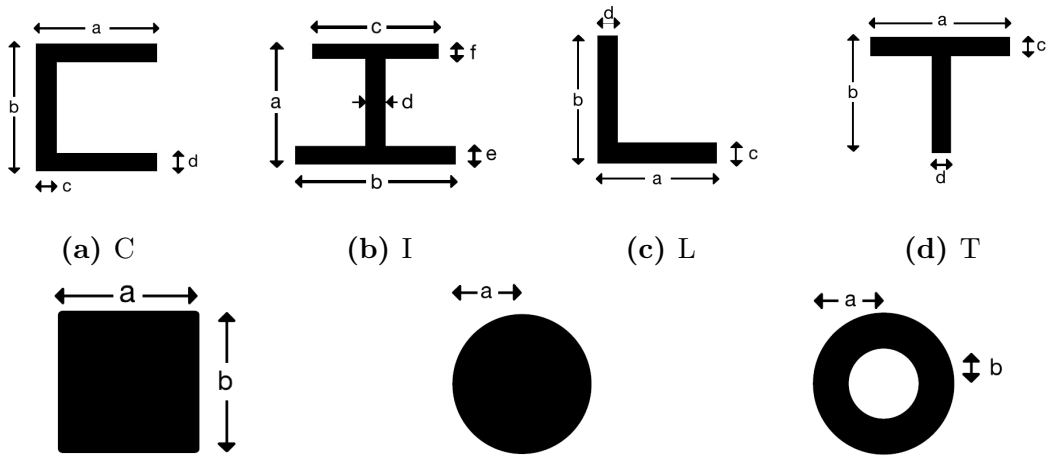

(a) C **(b)** I **(c)** L **(d)** T

(e) Bar **(f)** O **(g)** Tube

Figure 4.8: Studied beams sections

The material for the plates is treated as a laminate if the user set more than one layer; therefore, the thickness of each ply and its orientation with respect to the horizontal axis must be specified, which is especially important when using

orthotropic materials. For a parametric analysis, the thickness and orientation of each layer can be varied within a range or among discrete values chosen by the user, as the materials available on the market are limited.

Finally, the loads that can be varied are:

- Internal pressurization load;
- Gravitational inertial acceleration (lunar/terrestrial);
- Inertial acceleration due to launch;
- Inertial acceleration due to manoeuvrers.

Each of these loads has an associated Safety Factor (SF), which can be modified by the user. Minimum SF are reported in Tables 4.3, 4.4 [39]. To ensure a conservative design approach at this stage, the safety factor is selected as the highest value among those reported in the reference tables, resulting in SF = 2.

Table 4.3: Minimum design and test factors for metallic and composite space structures

Metallic Structures				
Verification Approach	Ultimate Design Factor	Yield Design Factor	Qualification Test Factor	Proof Test Factor
Prototype	1.4	1.0*	1.4	N/A or 1.05**
Protoflight	1.4	1.25	1.2	N/A or 1.05**
Composite Structures				
Verification Approach	Geometry of Structure	Ultimate Design Factor	Qualification Test Factor	Proof Test Factor
Prototype	Discontinuity Area	2.0***	1.4	1.05
	Uniform Material	1.4	1.4	1.05
Protoflight	Discontinuity Area	2.0***	1.2	1.2
	Uniform Material	1.5	1.2	1.2

* Structure has to be assessed to prevent detrimental yielding during its design service life, acceptance, or proof testing.
** Propellant tanks and SRM cases only.
*** Factor applies to concentrated stresses. For non-safety-critical applications, this factor may be reduced to 1.4 for prototype structures and 1.5 for protoflight structures.

The choice of boundary conditions is also important, as it strongly influences the solution. To simulate the operational and test configurations, a fixed constraint has been applied at the interface between the main structure and the wheel attachment, assuming this is a region of high stiffness. Since the project is still in a preliminary phase, the exact nature and position of these attachments are unknown, so the system has been constrained on the lower half of the first and the last frames of the cylindrical part of the rover (Figure 4.9a).

Table 4.4: Minimum design and test factors for habitable modules, doors, and hatches

Pressure Load Case	Yield Design Factor	Ultimate Design Factor	Proof Test Factor
Internal pressure only	1.65	2.0	1.5
Negative pressure differential*	N/A	1.5	N/A
Negative pressure differential verified by analysis only	N/A	2.0	N/A

*Has to be capable of withstanding maximum external pressure multiplied by the ultimate factor of safety (negative pressure differential) without collapse or rupture when internally pressurized to the minimum anticipated operating pressure.

For the launch configuration, the rover is assumed to be held fixed relative to the launcher by a stiffening system composed of two rings that constrain all its degrees of freedom, positioned at the first and last frames of the rover's cylindrical section (Figure 4.9b).

The last parameter that the user can vary is the Global Edge Length (GEL), which is the finite element mesh size. The optimal value depends on the geometry and the required accuracy. A convergence analysis was carried out, and a GEL of 0.1 m was adopted (Appendix A).

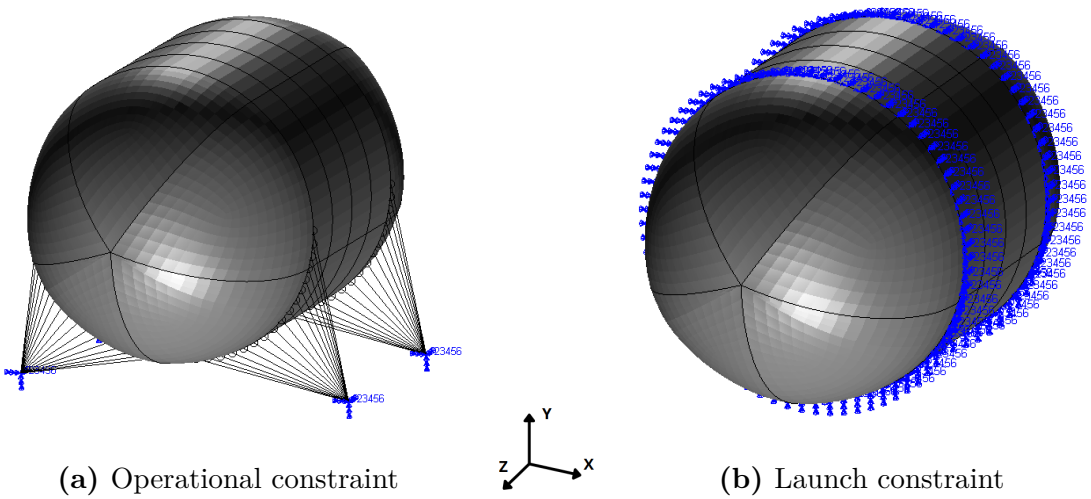

(a) Operational constraint **(b)** Launch constraint

Figure 4.9: Constraints in operational and launch configuration

4.4.2 Creation and execution of session file

Once the analysis is set up and the program is launched, the function that generates the structure's geometry based on the selected geometric parameters is automatically called. The geometry is created through a Patran *session file*. The file is read by Patran, which, once executed, sets up the input file for Nastran.

Patran generates the mesh by distributing the nodes that will be connected by the elements in such a way as to fit the elements as uniformly as possible within the associated geometry (in the case of a uniform mesh). For this reason, it is essential to create geometric entities with matching common interfaces (Figure 4.10). If this requirement is not satisfied, the nodes along the interfaces will differ and connectivity between elements belonging to different geometries is not guaranteed; as a result, geometric continuity of the numerical model is lost. For each curve and surface, the program assigns the appropriate property to the corresponding structural element, as defined in the input.

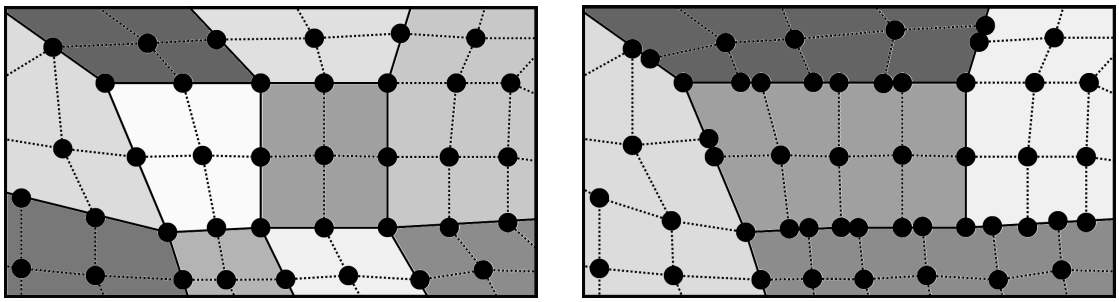

(a) Correct mesh **(b)** Improper mesh

Figure 4.10: Example of meshes of planar geometrical entities: colours refer to geometries, dots to nodes, and dotted lines to element edges

Four groups of geometries (and their associated elements) have been created:

- Outer shell – External surfaces of the rover;
- Stiffeners – Structural reinforcements of the external shell, including stringers, frames, and pillars;
- Floor – Floor panels of the rover;
- Floor stiffeners – Structural reinforcements coplanar with the floor;

To maintain a consistent structure, the elements must be connected through shared nodes. This is achieved using the Equivalence command, which eliminates the nodes that coincide within a specified tolerance, thereby allowing connections.

Care must be taken with this operation, as indiscriminate use may connect structural elements that are not physically joined. To prevent this, the system connects the groups in pairs as follows:

1. Equivalence between "Floor" and "Floor stiffeners," to join the floor plates with their reinforcements;

2. Equivalence between "Outer shell" and "Stiffeners," to join the load-bearing plates with their reinforcements;

3. Equivalence between "Floor stiffeners" and "Stiffeners," to connect the floor to the reinforcements and pylons.

This procedure avoids connecting elements of the floor with those of the outer shell except at the intended connection points.

To achieve meaningful predictions of the structural response, particularly regarding natural frequencies and inertial loads, the masses of the onboard subsystems must be included in the numerical model. Initially, a distributed approach was considered, in which each subsystem mass was applied as a concentrated inertial force at a point representing its plausible centre of gravity, connected to the structure through MPCs, specifically RBE3 elements. This method links the dependent node, where the mass is applied, to a set of independent nodes on the structural stiffeners, thereby distributing the load to the surrounding structural elements.

However, it was observed that this distributed approach produced results that were highly sensitive to the exact placement of each subsystem. At such a preliminary stage of the design process, the detailed positions of the subsystems cannot be reliably defined. Consequently, a centralized mass model was adopted: the total mass of all subsystems is concentrated in a single point, which is connected via RBE3 elements to all nodes belonging to the stringers, frames, and floor stiffeners. This approach, as illustrated in Appendix B, provides a set of predictive results for the global structural behaviour, suitable for initial numerical optimizations.

A secondary consequence of this modelling choice is a reduction in the local accuracy of stress predictions due to inertial loads. In the distributed model, local stress peaks occurred near the attachment points of the subsystems, whereas in the centralized model the inertial load is uniformly distributed across the stiffeners. Nonetheless, this approximation is acceptable at the preliminary design stage, since the primary goal of the framework is to provide a reliable tool for preliminary sizing and parametric studies of the structure. The different distributions of the point masses are illustrated in Figure 4.11.

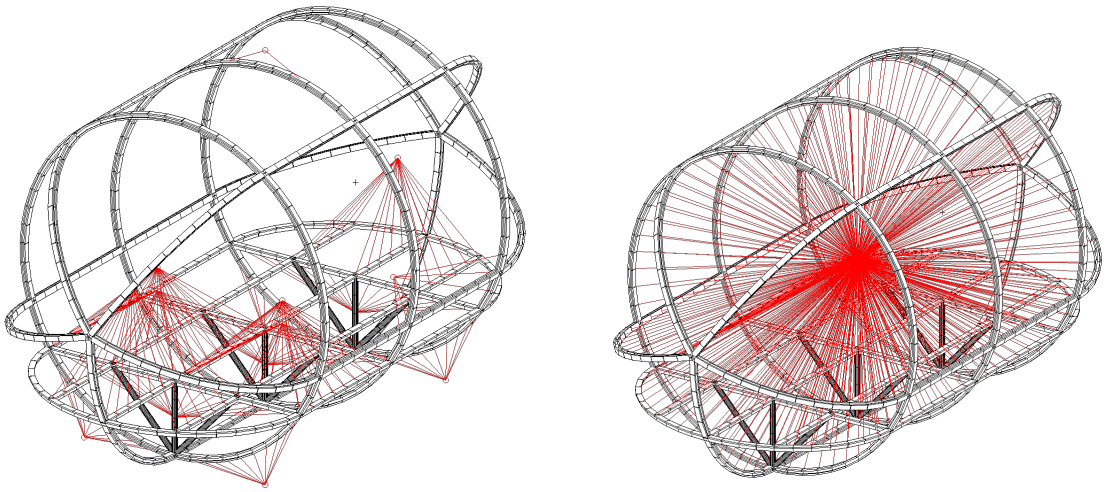

(a) Distributed model **(b)** Centralized model

Figure 4.11: Location of the MPCs in the distributed and centralized models

The masses considered are [40]:

- humans 160 kg;
- cockpit 300 kg;
- batteries 522 kg;
- locomotion system 462 kg;
- solar panels 25 kg;
- chairs 120 kg;
- hygiene system 100 kg;
- payload 500 kg;
- ECLSS 611 kg;
- EMU 290 kg;
- TCS 97 kg.

Finally, all loads and load cases (the combinations of loads applied under different conditions, as described in Section 3.1) are defined. The instructions for performing the analyses are then passed to Nastran.

4.4.3 Analysis and collection of results

Once the Patran *session file* has been executed, the resulting BDF is obtained. It contains all information about the numerical model which has been created. This type of file does not include any reference to the geometry itself, but only the numerical discretization, that consists in the position of each node and the connectivity between nodes through the created elements and their relative properties.

The BDF is then executed in Nastran, which solves the numerical problem and produces the results. Two types of analyses can be performed: a SOL101 (static

analysis) and a SOL103 (modal analysis), which simulate the load conditions the rover will experience throughout its operational life. As previously stated, for each parameter configuration, three static analyses and one modal analysis are carried out, or only a subset of them if requested by the user.

Upon completion of the analyses, Nastran generates an HDF5, a hierarchical data format that allows efficient handling of large amounts of information. The program then reads this file to extract the relevant data. For static analyses, these include the maximum nodal displacements and the stresses in both CQUAD4 and beam elements. For modal analysis, the most important data are the natural vibration frequencies of the structure, which are compared with the frequency of vibration of the launcher.

Another key piece of information, and the primary purpose of this program, is the total mass of the structure. This value is computed numerically by summing the masses of all elements and can be obtained for both static and modal analyses. Finally, another important set of data concerns the habitable and stowage volumes inside the rover, which are evaluated using the relations given below.

The habitable volume refers to the internal space enclosed between the floor and the outer shell. It should be noted, however, that this volume does not correspond to the actual space accessible to the crew, as it also contains subsystems and other components that must be accommodated within this region. The stowage volume, on the other hand, corresponds to the space beneath the floor, which can be used to house certain subsystems, such as the battery pack and the ECLSS.

For the ellipsoid and the elliptical cylinder geometry, the total volume, habitable volume, and stowage volume are calculated as follows:

- **Ellipsoid**

$$V_{\mathrm{TOT}} = \frac{2}{3}\pi a^2(b+c) \tag{4.10}$$

$$V_{\mathrm{hab}} = \pi a^2\,\xi, \qquad V_{\mathrm{stowage}} = V_{\mathrm{TOT}} - V_{\mathrm{hab}} \tag{4.11}$$

- **Elliptical cylinder**

$$V_{\mathrm{TOT}} = \frac{1}{2}\pi a(b+c)h + \frac{1}{3}\pi a(b+c)(f+r) \tag{4.12}$$

$$V_{\mathrm{hab}} = V_{\mathrm{cyl}} + \frac{1}{2}\pi a(f+r)\,\xi, \qquad V_{\mathrm{stowage}} = V_{\mathrm{TOT}} - V_{\mathrm{hab}} \tag{4.13}$$

$$V_{\mathrm{cyl}} = \left[\frac{1}{2}\pi ab + ac\Big(\arcsin(1-\alpha) + (1-\alpha)\sqrt{2\alpha-\alpha^2}\Big)\right] h \tag{4.14}$$

where in both cases:

$$\alpha = \frac{|y_{\mathrm{floor}}|}{c} = \frac{c - h_{\mathrm{floor}}}{c}, \qquad \xi = \frac{2b}{3} + c\left(\alpha - \frac{\alpha^3}{3}\right) \tag{4.15}$$

4.5 Design criteria

The criteria used for the design are:

- The rover's first natural frequency must be higher than the allowable value specified in the launcher's user manual;
- The stress in each component must be compared with its allowable value to ensure that all Failure Indices are less than 1;
- The habitable and stowage volumes must be greater than or equal to the required minimum values;
- The floor area and the fraction of walkable floor area must be greater than or equal to their minimum required values.

For Falcon Heavy the lower threshold for natural frequencies is 10 Hz for lateral modes, 25 Hz for axial modes and 35 Hz for secondary structures [20]. Distinguishing automatically between these categories within the present framework is not straightforward; therefore, a general minimum threshold of 25 Hz is adopted, as the analysis focuses on the design of primary structural elements at this stage of the project.

The failure index is a tool that allows us to determine whether a material has exceeded its allowable limit. As long as this index remains below 1, the material is considered intact; this evaluation is conducted using functions of the stresses within the element. For isotropic materials, the maximum stress criterion is adopted, which is given by the following expression:

$$\frac{\sigma}{\sigma_y} < 1 \tag{4.16}$$

This criterion compares the von Mises stress in each element with both the allowable tensile and compressive stress limits. For 2D elements, the Von Mises stress is evaluated at the element centroid, whereas for 1D elements it is taken as the maximum value among the stresses computed at the four section points (C, D, E, and F in Patran nomenclature).

On the other hand, a useful criterion for laminates is the Tsai-Hill criterion:

$$\frac{\sigma_1^2}{X^2} - \frac{\sigma_1 \sigma_2}{X^2} + \frac{\sigma_2^2}{Y^2} + \frac{\tau_{12}^2}{S^2} < 1 \tag{4.17}$$

where σ_1 and σ_2 are the normal stresses along the principal material directions of the laminate, τ_{12} is the in-plane shear stress, and X, Y and S represent the corresponding allowable strengths in the longitudinal, transverse and shear directions of the ply, respectively.

For the composite plates, the FI is computed by Patran and it can be red in the HDF5, whereas for isotropic plates, the software retrieves the stress components necessary to determine the Von Mises equivalent stress, which is subsequently compared with the material's allowable limit. By convention, a positive value of stress corresponds to tensile stress, a negative one to compressive stress. Once the stress vector is extracted, the program identifies the type of stiffener it belongs to thanks to its ID, and therefore the material associated with its property; the stress is then compared with the allowable value for that material. The sign of stress is used to determine whether the tensile or compressive allowable must be applied. The same procedure was followed for the beams.

The minimum volume of the habitable and the stowage sections can be evaluated from historical data of past NASA spacecraft (See Figure 4.12) [21], but there is not a strict regulation on this point. The equation of the regression line, which is only functional of the duration of the mission, is:

$$6.67 \log(\text{duration in days}) - 7.79. \tag{4.18}$$

Assuming a crew of two and a mission duration of 14 days, the estimated required pressurized volume is $19.63\,\mathrm{m}^3$. The reference data are derived from 0-g spacecraft; however, in the case of a rover, the available space cannot be exploited as efficiently as in a microgravity environment. Moreover, at this stage of the design, the volume occupied by subsystems is difficult to estimate. Therefore, based on engineering judgement, a conservative multiplicative factor of 1.5 is adopted, resulting in a required volume of $29.45\,\mathrm{m}^3$, considering only the habitable volume (V_{hab}).

The minimum height of the habitable section of the rover (h_{hab}) must also be sufficient to allow the crew to walk upright; therefore, a minimum height of 2 m (since the maximum height for ESA astronauts is 1.9 m) from floor level to ceiling is required for at least 75% of the walkable area of the rover, in order to allow comfortable movement inside the vehicle. This percentage is adopted as a reasonable engineering assumption for preliminary design purposes and allows the requirement to be formulated in a quantitative manner.

A requirement on the minimum floor area shall be defined in order to design an environment that allows the mission-required tasks to be performed comfortably. This metric was chosen because, in the presence of gravity, a constraint on the minimum floor area is more appropriate in addition to the minimum volume requirement [41]. Since no specific limits are available in the literature for pressurized rovers of this type, mainly due to the absence of operational missions with comparable characteristics, an external reference is required to define a reasonable lower bound for the habitable floor area. In this context, reference is made to the minimum living space standards established by the Council of Europe for confined living environments. These guidelines specify a minimum area of $4\,\mathrm{m}^2$ per person, with an additional $2\,\mathrm{m}^2$ allocated for shared space, resulting in a total minimum floor area

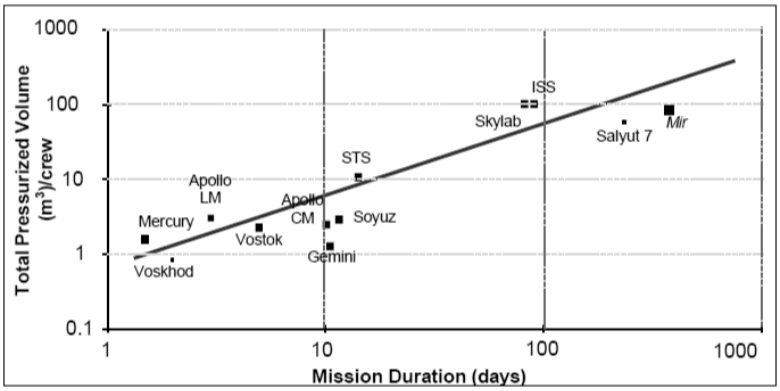

Figure 4.12: Historical NASA spacecraft pressurized volume

of 10 m^2 for a two-person crew [42]. Although developed for a different context, these standards provide a conservative benchmark for defining minimum spatial requirements in environments where occupants must remain for extended periods within a confined volume.

Furthermore, the storage compartment is intended to house the batteries and the ECLSS. It is advantageous to employ this volume for a subsystem with significant mass, as this allows efficient use of the available space while simultaneously lowering the rover's centre of gravity. Doing so improves stability during turning or in response to major asymmetric disturbances, such as encountering an obstacle located on only one side of the rover.

An estimate of the volume occupied by the two subsystems can be performed as follows. The masses of the subsystems were provided by Bruna Di Maggio, who was responsible for the design of the rover subsystems, in her master's thesis *Multidisciplinary Design and Optimization of a Pressurized Rover for Lunar Surface Exploration* [40].

The battery system is based on $N = 8536$ LG INR18650–MJ1 cells, whose characteristics are reported in Table 4.5 [43].

Table 4.5: LG INR18650–MJ1 cell properties

Parameter	Symbol	Value
Cell mass	m_{cell}	0.049 kg
Cell diameter	d_{cell}	18.5×10^{-3} m
Cell length	l_{cell}	65.1×10^{-3} m
Cell volume	V_{cell}	1.75×10^{-5} m^3

Assuming an optimal packing factor of $f = \pi/\sqrt{12} \approx 0.9069$ (corresponding to circle packing [44]) and an additional efficiency factor of $\eta = 0.9$ to account for

interfaces and required clearances, the total battery volume is

$$V_{\text{batt}} = \frac{N\, V_{\text{cell}}}{f\, \eta} = 0.183\,\text{m}^3 \tag{4.19}$$

For the Environmental Control and Life Support System, the subsystem masses and densities listed in Table 4.6 are considered.

Table 4.6: ECLSS consumables and storage properties

Material	**Mass** [kg]	**Density** [kg/m^3]
Oxygen (O_2)	23.52	248
Water (H_2O)	344.12	997
Lithium Hydroxide (LiOH)	28.00	1460
Food	22.40	412

Oxygen must be stored in a pressurized tank; the optimal geometry in this case is spherical. The tank wall thickness is computed from the thin-walled pressure vessel relation:

$$t = \frac{p_{O_2}\, r_{O_2}}{2(\sigma_y/SF) - p_{O_2}} \tag{4.20}$$

with the oxygen pressure $p_{O_2} = 18.892\,\text{MPa}$ [45], safety factor SF = 1.5 and the Inconel yield stress $\sigma_y = 1034.21\,\text{MPa}$.

The internal tank radius is obtained from the oxygen volume, which is computed from the ideal gas law as

$$V_{O_2,ideal} = \frac{M_{O_2} R_{O_2} T}{p_{O_2}} \tag{4.21}$$

with $T = 293.15\,\text{K}$ and $R_{O_2} = 259.8\,\text{J/(kg K)}$. The equivalent spherical tank radius is therefore

$$r_{O_2} = \left(\frac{3V_{O_2,ideal}}{4\pi}\right)^{1/3}. \tag{4.22}$$

Using these values, the wall thickness is found to be $t = 3.9\,\text{mm}$, and the resulting tank mass is $M_{\text{tank},O_2} = 10.98\,\text{kg}$. The tank volume is conservatively estimated by approximating it as a cube with side length $r_{O_2} + t = 0.287\,\text{m}$, which yields $V_{O_2} = 0.024\,\text{m}^3$. A multiplicative factor of $f = 1.3$ is applied to account for additional tanks, valves, and interfaces, leading to a total ECLSS volume of

$$V_{\text{ECLSS}} = (V_{O_2} + V_{H_2O} + V_{\text{LiOH}} + V_{\text{food}})\, f = 0.575\,\text{m}^3. \tag{4.23}$$

The total volume occupied by the two subsystems is therefore

$$V_{\text{tot}} = V_{\text{batt}} + V_{\text{ECLSS}} = 0.758\,\text{m}^3. \tag{4.24}$$

Regarding the maximum dimensions allowed by the selected launcher, shown in Figure 4.13 [20], a 20% margin is considered since neither the presence of external elements to the main body, such as the locomotion system, nor the presence of a lander, which is necessary for performing the lunar landing, are taken into account. Furthermore, the length of the fairing is not being considered as a constraint because the Falcon Heavy provides an extended fairing that would easily fulfil the task of housing the rover. The maximum mass that the launch vehicle is capable of delivering to lunar orbit is 16,800 kg, based on the assumptions presented in Section 3.1. A margin of 30% is therefore applied to account for interfaces and the lunar lander, resulting in a maximum allowable mass limit of 11,760 kg.

These limits are adopted to maintain a realistic design framework based on current launch capabilities. However, it is expected that future missions of this type will likely rely on next-generation launch vehicles, which may provide significantly larger mass and volume capacities than those considered in the present study.

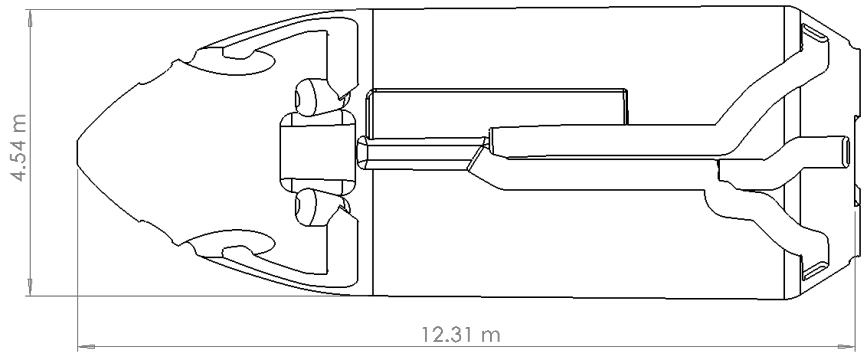

Figure 4.13: Falcon's fairing internal size

In summary, the constraint equations that limit the designing are:

- FI $< 1 \; \forall$ finite element;
- FNF > 25 Hz;
- $V_{\text{hab}} \geq 29.45\,\text{m}^3$;
- $h_{\text{hab, 2 m}} \geq 75\%$;
- $A_{\text{floor}} \geq 10\,\text{m}^2$;
- $\max(2a,\, bc) \leq 3.63$ m;
- $V_{\text{stowage}} \geq 0.758\,\text{m}^3$;
- $M_{\text{tot}} < 11{,}760$ kg.

4.6 Vibroacoustic analysis

After completing the analysis, once a suitable configuration has been identified, it will also be necessary to perform a vibroacoustic analysis to assess the effects of the acoustic field inside the launcher fairing. Approximately 60% of satellite failures during the first day of life are caused by damage due to high acoustic loads during launch [46], so it is essential to take this analysis into account.

The launch environment is characterized by strong dynamic vibrations that propagate from the launcher to the payload. These loads mainly originate from two phenomena:

- Engine-induced excitations resulting from the supersonic exhaust plume and its interaction with the launch pad during lift-off;
- Structural dynamic responses of the launch vehicle caused by aerodynamic loads and aeroelastic instabilities during ascent.

For this reason, two launch phases are considered particularly critical: the lift-off, and the transonic flight phase, which is typically the most demanding in terms of aerodynamic loading.

Sound is a pressure variation in an elastic medium and propagates through matter. The associated fluctuations relative to the static level of the medium define the Sound Pressure Level (SPL). Sound waves reach the fairing, and from it the fluctuations are transmitted inside. Since the fairing is an enclosed cavity, the sound is reflected by the internal walls, giving rise to a reverberant effect, increasing the intensity of the acoustic field. This is therefore referred to as a diffuse acoustic field inside the fairing [46], meaning that the sound energy is uniformly distributed within the environment, and there is no preferred direction, but the wave reflections come from all directions with equal probability (non-directional field).

Maximum Predicted Environment (MPE) indicates the limit for which in 95% of launches the SPL will be equal to or below the indicated value, with a 50% statistical confidence [47].

Starting from the SPL values, it is possible to derive the Power Spectral Density (PSD) of the input acoustic pressure as:

$$W_p = \frac{P(f)^2}{f} \qquad \left[\mathrm{Pa}^2/\mathrm{Hz}\right] \tag{4.25}$$

where the pressure amplitude $P(f)$ is obtained from the SPL through the relation:

$$P(f) = P_{\mathrm{ref}}\, 10^{\frac{\mathrm{SPL}(f)}{20}} \qquad [\mathrm{Pa}] \tag{4.26}$$

with the reference pressure defined as:

$$P_{\mathrm{ref}} = 2 \times 10^{-5}\,\mathrm{Pa}. \tag{4.27}$$

The pressure PSD describes how the acoustic pressure energy is distributed as a function of frequency. This quantity is of fundamental importance, as it represents the input for the random vibration analysis, which computes the frequency response function ($H(f)$) of the finite element model and, through it, allows the evaluation of the structural response (such as accelerations) also expressed in terms of PSD, according to the relation:

$$W_{\ddot{x}} = |H(f)|^2 \, W_p \qquad \left[\mathrm{g}^2/\mathrm{Hz}\right]. \tag{4.28}$$

Table 4.7 and Figures 4.14, 4.15 show MPE (P95/50) acoustic field and it's PSD using acoustic blankets and a fairing fill factor up to 60%, based on data from the LC-39A launch site at the Kennedy Space Center, Florida [20].

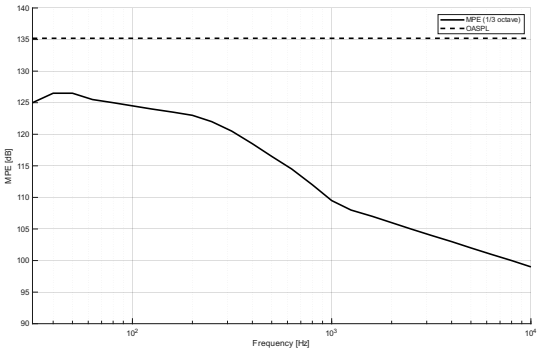

Figure 4.14: Falcon Heavy Acoustic MPE Spectrum

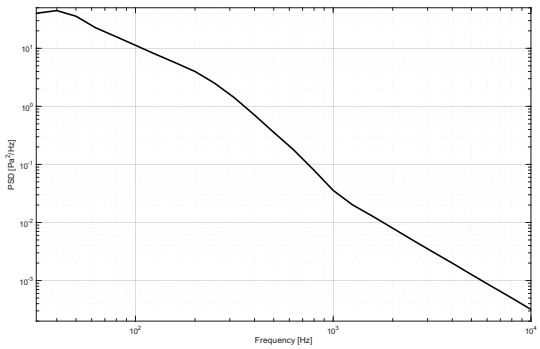

Figure 4.15: Falcon Heavy Acoustic pressure PSD

There are mitigation methods to reduce vibrations; these include the use of materials with high acoustic insulation, modifications to the engine nozzle, and the use of barriers that absorb or redirect sound waves. The main parameters influencing acoustic loads can be classified as:

- Parameters related to the flow exiting the launcher nozzle;
- Launcher, launch pad, and flow geometry;
- Vehicle velocity.

One of the most common mitigation methods during the ground phase is the injection of water into the exhaust plumes. This is done because water has acoustic suppression properties while also protecting the launch pad by cooling the exhaust gases. Studies have shown that the greater the water flow, the greater the beneficial effect of suppression across all frequencies [48].

Regarding acoustic loads during flight caused by the interaction between the external airflow and the launcher, the design of the vehicle's external shape is

Table 4.7: Acoustic MPE at LC-39A with acoustic blankets and 60% fill factor inside the fairing (1/3-octave bands)

Frequency [Hz]	**Acoustic MPE [dB]**	**PSD [Pa^2/Hz]**
31.5	125.0	4.016×10^{1}
40	126.5	4.467×10^{1}
50	126.5	3.573×10^{1}
63	125.5	2.253×10^{1}
80	125.0	1.581×10^{1}
100	124.5	1.127×10^{1}
125	124.0	8.038
160	123.5	5.597
200	123.0	3.991
250	122.0	2.536
315	120.5	1.425
400	118.5	7.079×10^{-1}
500	116.5	3.573×10^{-1}
630	114.5	1.789×10^{-1}
800	112.0	7.924×10^{-2}
1000	109.5	3.565×10^{-2}
1250	108.0	2.019×10^{-2}
1600	107.0	1.253×10^{-2}
2000	106.0	7.962×10^{-3}
2500	105.0	5.060×10^{-3}
3150	104.0	3.190×10^{-3}
4000	103.0	1.995×10^{-3}
5000	102.0	1.268×10^{-3}
6300	101.0	7.993×10^{-4}
8000	100.0	5.000×10^{-4}
10,000	99.0	3.177×10^{-4}
OASPL	**102.0**	-

important. Absorption and dissipation strategies are also used (converting the energy of sound waves into other forms of energy) or through scattering of sound waves in order to reduce their intensity [46].

Despite their importance, including this type of calculation within the main design loop would cause a dramatic increase in computational cost, as the computation time for a random analysis is several orders of magnitude higher than that of a simple static analysis. Therefore, since system survival under this load must

be guaranteed, the vibroacoustic analysis should be performed downstream of all calculations on the chosen configuration. If the requirements are not met, another configuration among the best obtained is selected, and the vibroacoustic analysis is carried out on that system. This process continues until a configuration passes this test. Proceeding in this way for our case study is appropriate because only the main structural components are analysed, and often for this type of structures, acoustic loads do not represent a critical design condition [49].

4.7 Optimization

In order to refine the output, it is appropriate to proceed with a numerical optimization. These algorithms vary a set of characteristic parameters of the problem, appropriately selected by the user, to achieve a solution with improved performance. Such performance is evaluated through an objective function, which must be minimized while simultaneously satisfying a set of constraint functions.

Applying this to the current study, the function to be minimized is:

$$min(f(x)) \tag{4.29}$$

where $f(x) = mass$ and x is the vector of the design variables.

It was decided to carry out the optimization by fixing the geometric parameters, thereby automatically satisfying the geometric conditions reported in Section 4.5. Consequently, the constraint equations are:

$$\begin{cases} FI < 1 \\ FNF > 25 \text{ Hz} \end{cases} \tag{4.30}$$

The variables selected for the optimization are:

- A Parameter of stringers section;
- B Parameter of frames section;
- C Parameter of floor stiffeners section;
- D Parameter of pillars section;
- th Thickness of the outer shell;
- th_{floor} Thickness of the floor.

With reference to the nomenclature in Figure 4.8, the following cross-sections were selected:

- Stringers: I-section with characteristic parameters $a = b = c = A$, $d = e = f = A/4$;
- Frames: C-section with characteristic parameters $a = b = B$, $c = d = B/4$;
- Floor stiffeners: T-section with characteristic parameters $a = b = C$, $c = d = C/4$;
- Pillars: Tube section with characteristic parameters $a = D$, $b = D/2$.

This choice was made in order to simplify the optimization process by reducing the number of design variables and, consequently, the overall complexity of the problem. For the same reason, the geometry was also fixed, adopting a configuration that satisfies all imposed geometric constraints, as well as a fixed number of reinforcements.

Surrogate-Based Optimization (SBO) is a methodology widely adopted in structural design problems where the evaluation of the objective function is computationally expensive, as is typically the case for FEM analyses. The core idea is to guide the optimization process through an approximate and computationally efficient model, referred to as a surrogate model, which is constructed using a limited set of high-fidelity simulations.

The optimization process begins with the definition of the design space, characterized by a set of input variables and their admissible ranges (Table 4.8). In this work, the optimization is performed using Matlab's built-in surrogateopt algorithm, which implements a surrogate-based global optimization strategy [50]. The algorithm iteratively samples the design space within the prescribed lower and upper bounds, evaluates the objective function, and progressively refines an internal surrogate model based on the accumulated function evaluations. At each iteration, a balance is maintained between exploration of previously unexplored regions and exploitation of promising areas of the design space.

Table 4.8: Optimization parameters and corresponding lower and upper bounds

Optimization Parameter	**Lower Bound [mm]**	**Upper Bound [mm]**
A	8	60
B	8	60
C	8	60
D	8	60
th	0.6	6
th_{floor}	0.6	6

The surrogate model is therefore used to guide the selection of new candidate solutions, which are subsequently evaluated using the high-fidelity model and

incorporated into the dataset. This iterative procedure continues until a convergence criterion is satisfied, such as reaching the maximum number of function evaluations or observing negligible improvement in the objective function.

The main advantage of surrogate-based optimization lies in its ability to significantly reduce the computational cost associated with the optimization of complex problems, while maintaining a satisfactory level of accuracy. This makes it particularly suitable for preliminary design phases, where multiple configurations must be explored efficiently.

Chapter 5

Results and discussion

This chapter presents a series of parametric analyses illustrating the relationships between key quantities and selected design parameters. Such sensitivity analyses are essential for identifying parameter dependencies and for defining the design region in which the optimal solution will be sought.

The plots are obtained through linear interpolation of the analysis results. Each analysed case is represented by a marker, which can be either a circle (○) or a cross (×). The circle denotes cases in which all constraints are satisfied, whereas the cross indicates cases that do not meet these constraints. This graphical convention is primarily intended to facilitate the interpretation of the results, although it can be disregarded when analysing the general trends shown by the plots.

5.1 Primary Structure - Cylinder

The dependence of the geometric results on the parameters that most strongly influence them is now analysed. In particular, the habitable volume and the storage volume (Figures 5.1a, 5.1b) are primarily affected by the parameters defining the external shape of the rover. In the case of a cylindrical configuration, these are the radius (r) and the length of the constant cross-section body (h), with both volumes increasing as either or both of these parameters increase.

Regarding the total floor area, it strongly depends on the radius, length, and floor height relative to the lowest point (h_{floor}), as shown in Figures 5.1c, 5.1d. The area increases with all three parameters for $0 \leq h_{\text{floor}} \leq c$, while this trend reverses if h_{floor} exceeds the lower semi-minor axis. This parameter also affects the percentage of walkable area, defined as the portion with a height of at least 2 m. As shown in Figures 5.1e, 5.1f, increasing h_{floor} reduces the ceiling height and thus the walkable area, whereas the radius has the opposite effect.

The observation and analysis of these geometric results make it possible to

identify the design region within which these variables should be varied.

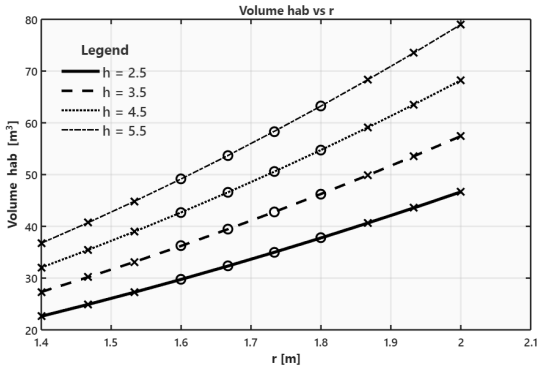

(a) Habitable volume (r, h)

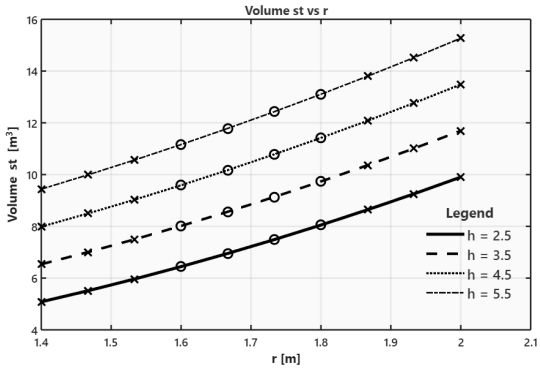

(b) Stowage volume (r, h)

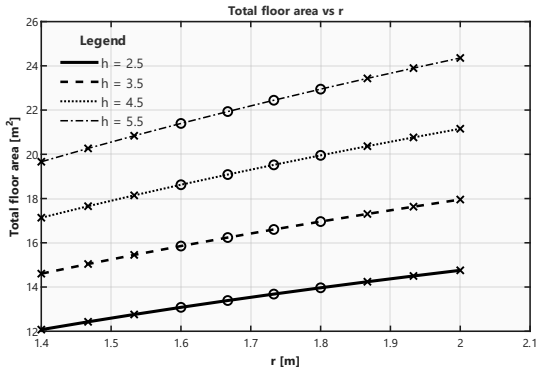

(c) Floor area (r, h)

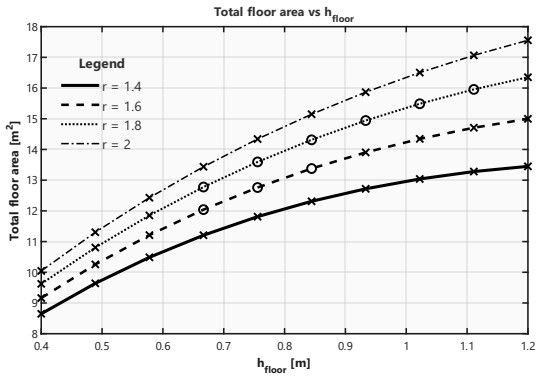

(d) Floor area (h_{floor}, r)

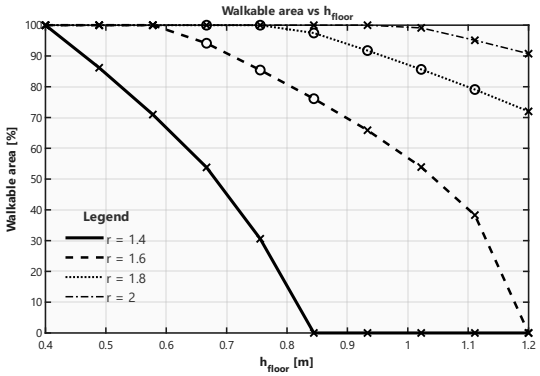

(e) Walkable area percentage (h_{floor}, r)

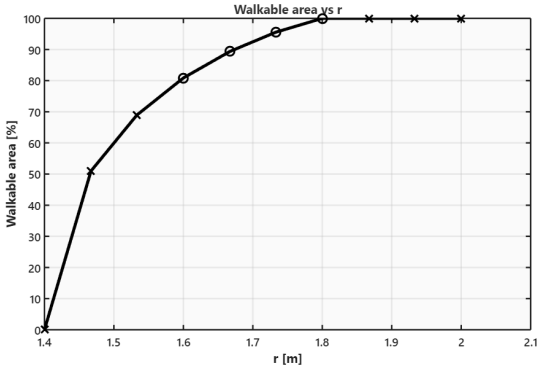

(f) Walkable area percentage (r)

Figure 5.1: Geometrical results for the cylindrical model: V_{hab}, A_{floor}, $h_{\text{hab, 2 m}}$

The effect of r and h is illustrated in Figure 5.2. Specifically, the mass shows a linear dependence on both the radius and the length (Figure 5.2a). In contrast, FNF decreases as these parameters increase (Figure 5.2b). The decrease in the first natural frequency with increasing radius and length can be explained by the combined effect of increasing mass and decreasing structural stiffness. In particular, the increase in length significantly reduces the bending stiffness, while both parameters contribute to a higher mass. As a result, the stiffness-to-mass ratio decreases, leading to lower natural frequencies.

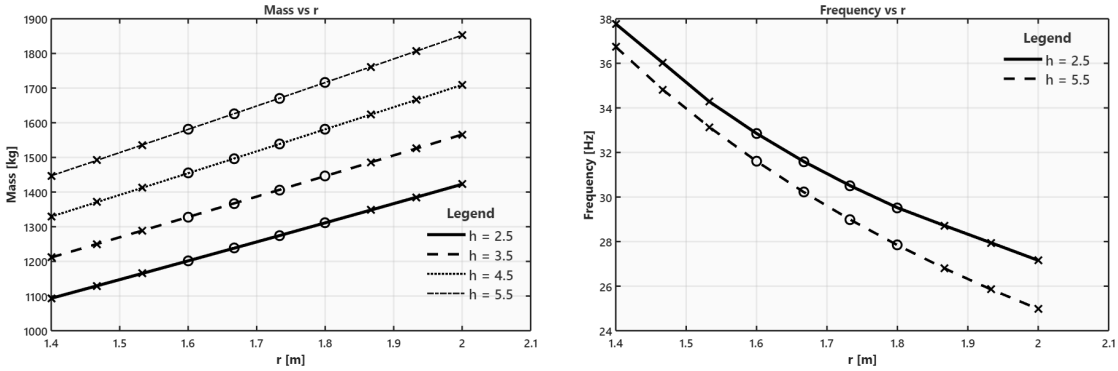

(a) Mass (r, h) **(b)** FNF (r, h)

Figure 5.2: Mass and FNF diagrams for the cylindrical model

Regarding deformations and failure indices, they have been categorized according to three different regions of the rover in order to enable a more targeted comparison and avoid mixing data from different sources:

- shell - the outer shell and its associated stiffeners
- floor - the floor and its associated stiffeners
- pil - the floor pillars

Furthermore, the failure indices have been classified according to the type of target element:

- beam - FI corresponding to CBEAM elements
- plate - FI corresponding to CQUAD (or CTRIA) elements

The presence of CTRIA elements is generally avoided, as they are less performant than CQUAD elements. However, their use is sometimes unavoidable, particularly for meshes generated via a black-box approach, as in the present case.

The effect of the outer shell thickness (th) is now evaluated. As shown in Figure 5.3, increasing the thickness leads to a reduction in both displacements and failure indices, with a particularly significant impact at lower thickness values. Moreover, the largest effect is observed on the failure index of 2D elements: a variation of -88.9% is found between the considered extremes, compared to a -43.75% variation for beam elements. The reduction in displacement is also significant, amounting to approximately -80%.

The plots refer to quantities evaluated on the outer shell elements and are presented only for load case S1, as the trends observed for the other two static cases are analogous.

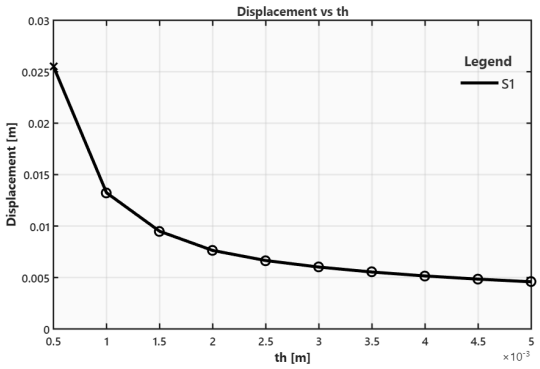

(a) Displacement (th)

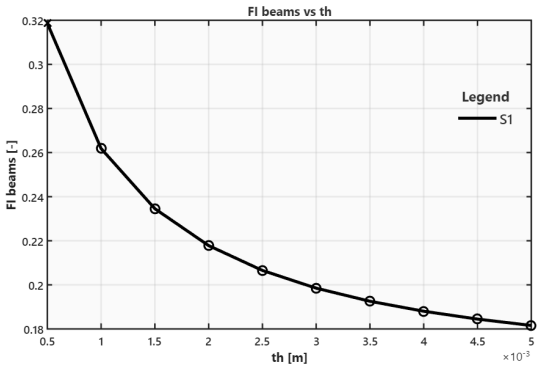

(b) FI beams (th)

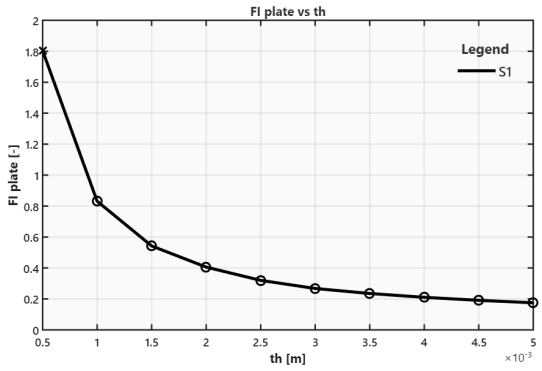

(c) FI plates (th)

Figure 5.3: Effect of shell thickness on the cylindrical model

Similarly, the effect of the floor thickness th_{floor} is shown in Figure 5.4. In this case, the reported plots refer to results extracted from the floor elements, i.e., those most affected by its thickness. As shown in Figure 5.4a, an anomalous trend in displacement can be observed for load case S1 at low thickness values, which then stabilizes as the thickness increases. This behaviour can be explained by the fact

that load cases S2 and S3 are mainly characterized by axial and lateral acceleration forces, acting within the plane of the floor. This results in smaller deformations compared to case S1, which also includes a component perpendicular to the floor. These effects are more pronounced at low thickness values, where the floor exhibits lower bending stiffness.

Regarding the failure indices (Figures 5.4b, 5.4c), the thickness has a stronger influence on the FI of plate elements, which decreases as the thickness increases. In contrast, for beam elements, an opposite trend is observed between load cases S2 and S3, again due to the different directions of the applied forces, which excite the structure differently.

Finally, the effect on the first natural frequency is shown in Figure 5.4d. This parameter has a significant impact, leading to variations of up to a factor of seven between the initial and final values within the considered range.

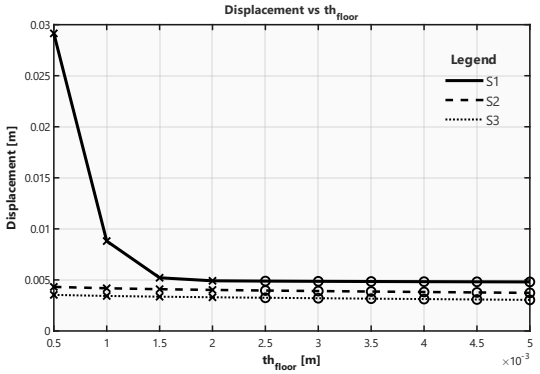

(a) Displacement (th_{floor})

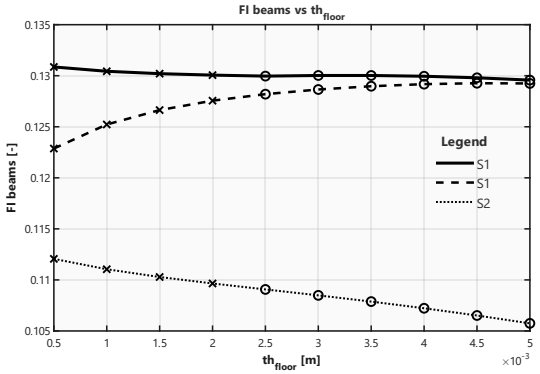

(b) FI beams (th_{floor})

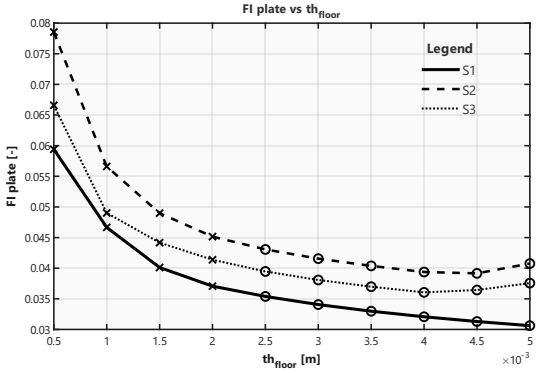

(c) FI plates (th_{floor})

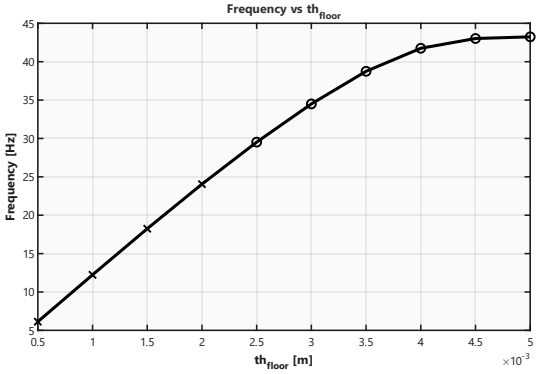

(d) FNF (th_{floor})

Figure 5.4: Effect of floor thickness on the cylindrical model

If the cross-section is changed from circular to bi-elliptical (Figure 4.3), the structural response also changes, especially under pressurization load case S1. As Figure 5.5 shows, increasing differences among the semi-axes (a, b, c), thus making the section more elliptical, significantly raises the resulting stresses. As noted earlier, the circular section is the most efficient for containing internal pressure, which is evident in Figure 5.5a, where the minimum FI occurs around 2 m when the semi-axes are similar. This behaviour holds even though increasing the section radius also raises the stress level (Figure 5.5d), making it important to keep the cross-section as close to circular as possible. Figure 5.5c shows the pronounced difference in FI between highly elliptical and nearly circular configurations, with reductions up to -26.7%. In some cases, modifying the cross-section can still be advantageous for space optimization and lowering the centre of gravity, but the resulting increase in FI (and structural mass) can be significant.

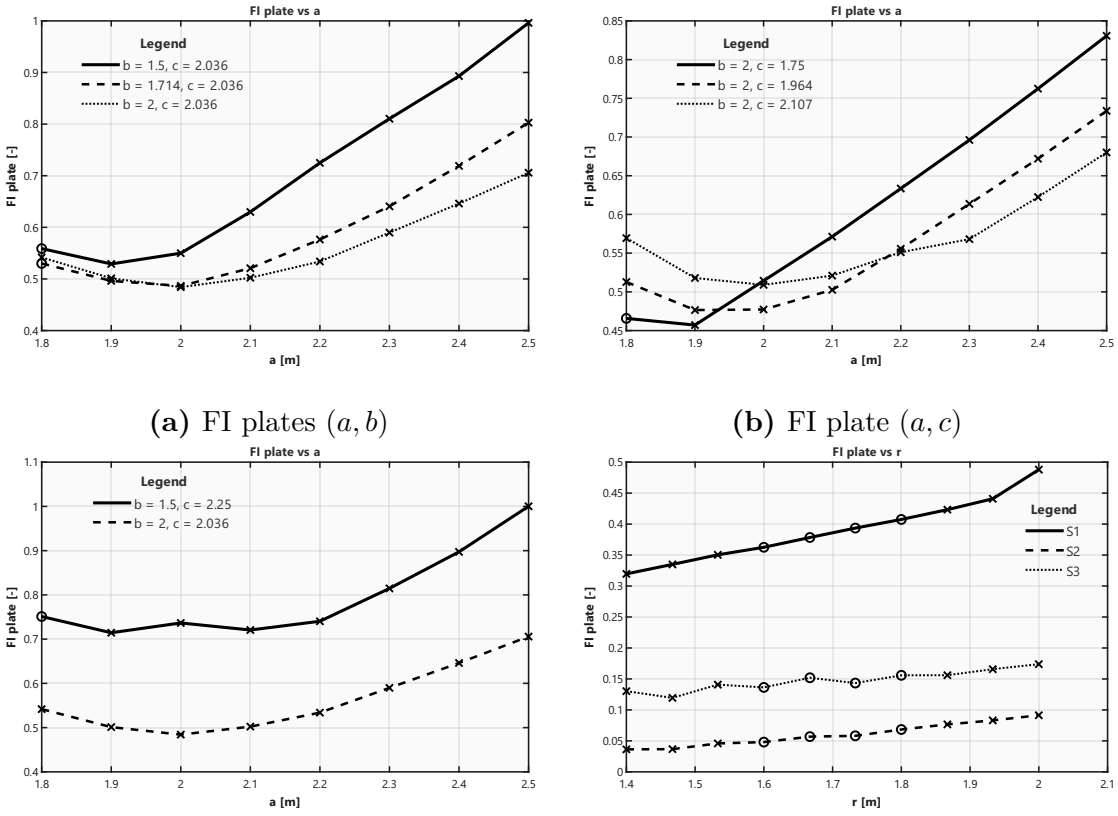

(a) FI plates (a, b) **(b)** FI plate (a, c)

(c) FI plates (a, b, c) **(d)** FI plate (r)

Figure 5.5: Effect of elliptic section on the cylindrical model

Two additional parameters of interest are n_{str} and n_{fr}, representing the number of stringers and frames, respectively.

The dependencies on n_{str} are shown in Figure 5.6. The values remain relatively constant, particularly with regard to the failure indices; this weak influence of the number of stringers is consistent with the fact that the dominant loading conditions mainly generate membrane stresses in the shell, which are efficiently carried by the shell itself.

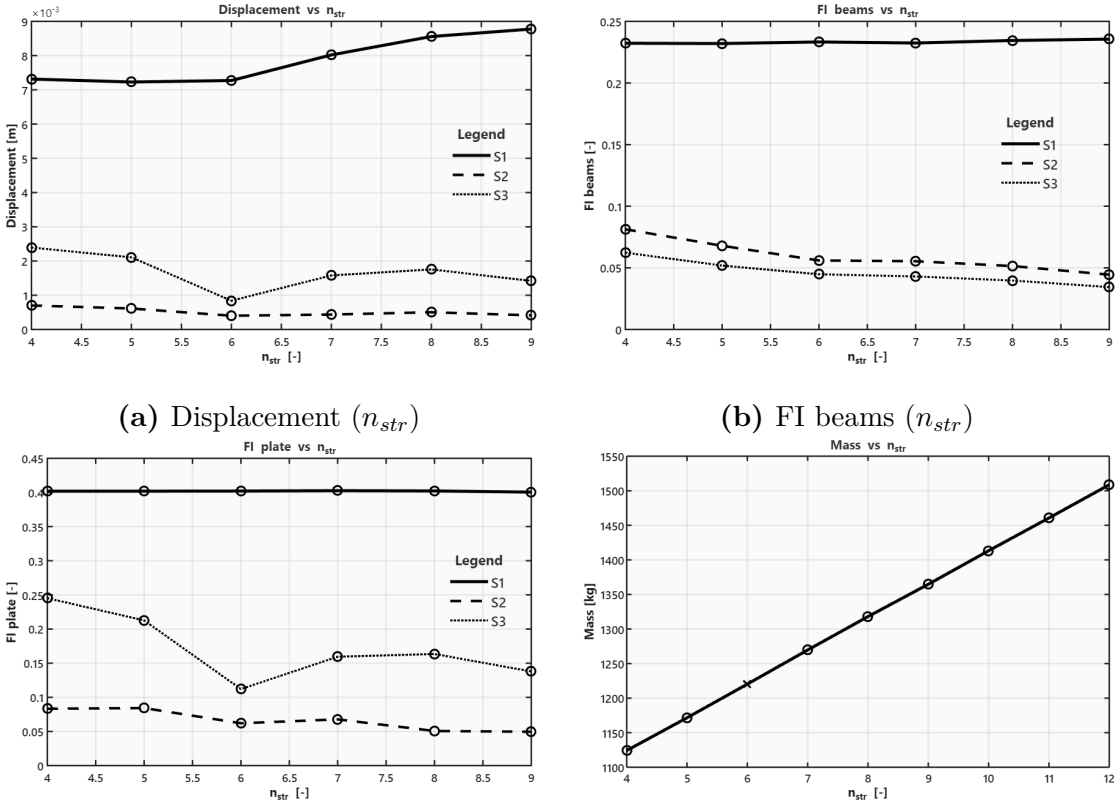

(a) Displacement (n_{str})

(b) FI beams (n_{str})

(c) FI plates (n_{str})

(d) Mass (n_{str})

Figure 5.6: Effect of number of stringers on the cylindrical model

Turning to the dependencies on n_{fr}, it can be observed that increasing the number of frames generally has a positive effect, both in terms of maximum displacement and failure indices. The exception is load case S1, where an increase in frames leads to higher stresses and, consequently, higher failure indices in the plate elements.

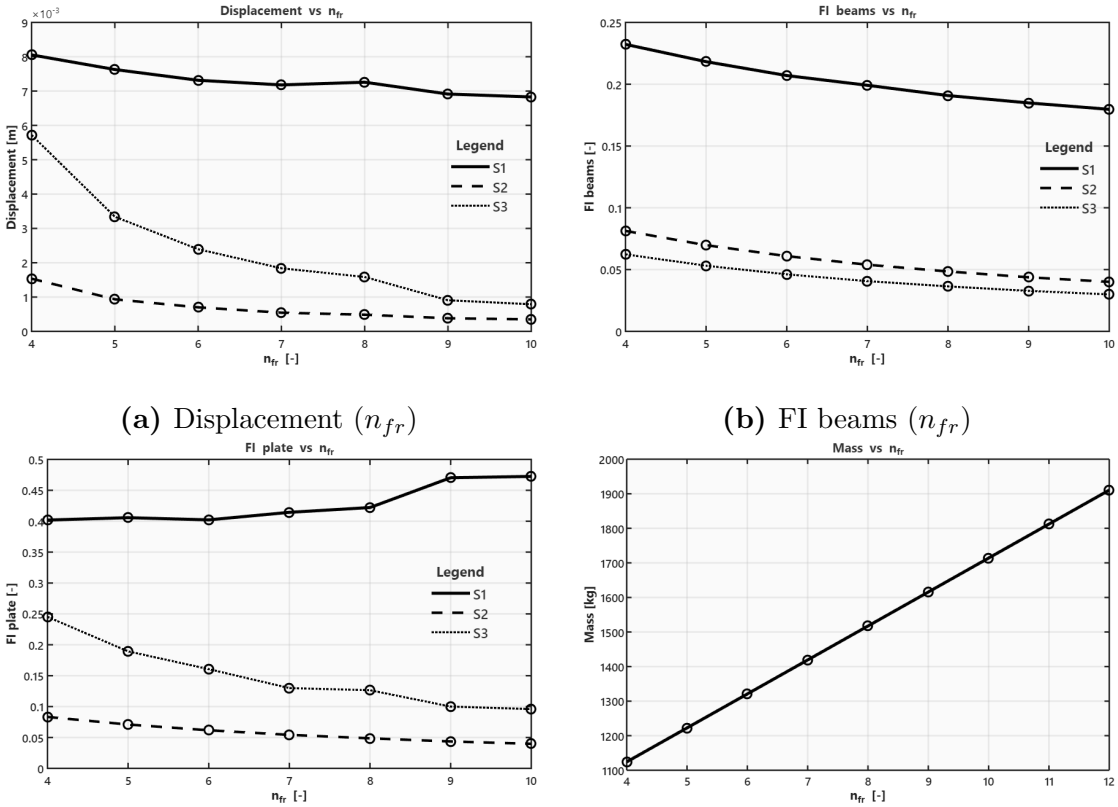

(a) Displacement (n_{fr})

(b) FI beams (n_{fr})

(c) FI plates (n_{fr})

(d) Mass (n_{fr})

Figure 5.7: Effect of number of frames on the cylindrical model

For both parameters, load case S1 shows the highest values, even though the literature indicates that the most critical loads occur during launch. This discrepancy is due to a necessary simplification adopted to obtain a practical tool for preliminary design: the masses of all subsystems were modelled as a single lumped mass, connected via a MPC to the stiffeners throughout the structure (both on the floor and on the outer shell). As a result, the inertial loads of the subsystems were distributed approximately uniformly across the structure, significantly reducing the local stress concentrations that would have occurred with a localized mass distribution.

This simplification has a much greater impact on load cases S2 and S3, which are characterized by high accelerations and thus high inertial forces, whereas the dominant load in case S1, namely pressure, acts unchanged and remains the primary driver for sizing. As will be shown in Appendix B, the results will change once this simplification is removed.

It should be noted that the variation of the FNF is shown only for the floor thickness. This is because, within the parameter ranges considered in these examples, the first mode shape always involves the floor, making its thickness the parameter with the most significant influence. By increasing the stiffness of this element, through greater plate and stiffener thickness, the influence of the other parameters becomes observable, as shown in Figure 5.8. As expected, increasing the dimensions of the structure (r and h) leads to lower natural frequencies. Increasing the structural stiffness (n_{str} and n_{fr}), on the other hand, leads to an increment in the FNF. The effect of the number of stringers (Figure 5.8c) is instead marginal and does not significantly affect this result.

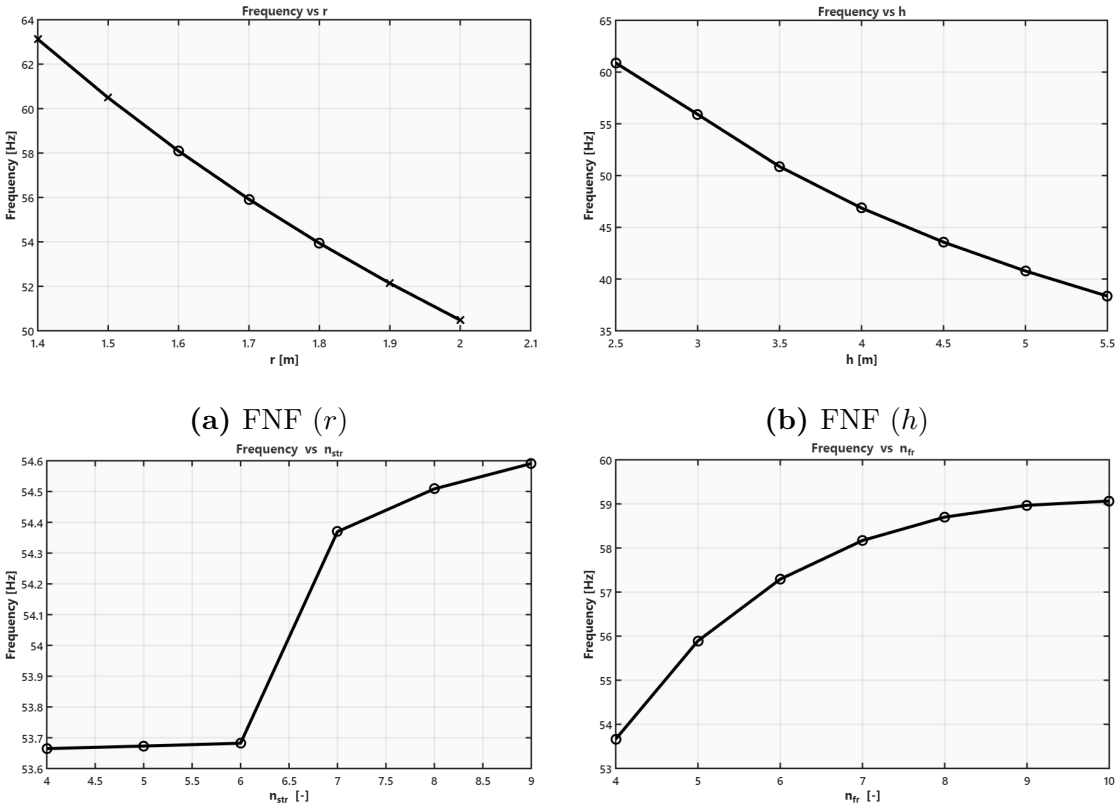

(a) FNF (r)

(b) FNF (h)

(c) FNF (n_{str})

(d) FNF (n_{fr})

Figure 5.8: Effect of FNF on the cylindrical model with stiffened floor

5.1.1 Cylinder optimization - Results

The optimization was carried out using a fixed geometric configuration, shown in Figure 5.9, whose parameters are reported in Table 5.1. The geometric constraints were satisfied:

- $V_{\text{hab}} = 29.45\,\text{m}^3 \geq 29.45\,\text{m}^3$
- $h_{\text{hab,2 m}} = 100\% \geq 75\%$
- $A_{\text{floor}} = 10.29\,\text{m}^2 \geq 10\,\text{m}^2$
- $max(2a,\, bc) = 3\,\text{m} \leq 3.63\,\text{m}$
- $V_{\text{stowage}} = 5.87\,\text{m}^3 \geq 0.758\,\text{m}^3$

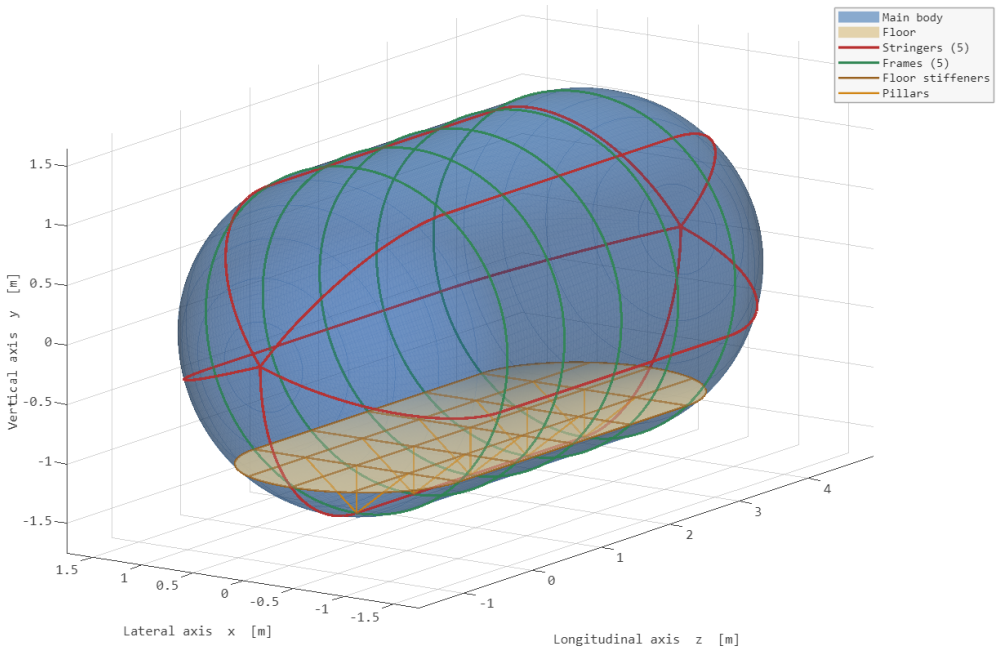

Figure 5.9: Cylindrical model geometry used for numerical optimization

The optimization was carried out with a limit of 300 objective function evaluations. A configuration was found with the parameters reported in Table 5.2, corresponding to a structural mass of 327.2 kg. This value, together with the results in terms of displacements and failure indices for the different load cases, is reported in Table 5.3. The contour plots of the quantities associated with the elements of the outer shell are shown in Figure 5.10. Note that displacements are expressed in m, while stresses are expressed in Pa.

Variable	Value	Variable	Value
a [m]	1.50	b [m]	1.40
c [m]	1.50	h [m]	3.30
f [m]	1.40	r [m]	1.40
h_{floor} [m]	0.40	$n_{\text{str,floor}}$	1
n_{str}	5	n_{fr}	5
$n_{\text{fr,f}}$	0	$n_{\text{fr,r}}$	0

Table 5.1: Geometrical parameters of the cylindrical model for the optimization

It can be observed that, in the load cases associated with launch (particularly S2) the maximum stress occurs in the stringers of the caps located closest to the floor. This behaviour is caused by the inertia of the floor, which transfers the load to the outer structure in that region. The phenomenon is especially evident in load case S2 due to the longitudinal direction of the acceleration, whereas in load case S3 a lateral acceleration component induces higher stresses in the lateral interface between the outer shell and the floor, as shown in Figures 5.10e and 5.10f.

In load case S1 (Figure 5.10d), the maximum stress occurs in the upper region of the central body of the rover. This behaviour is consistent with the theoretical considerations discussed in Section 4.2, as the cylindrical portion of the structure is subjected to higher stresses under pressurization loads.

Finally, the deformations and stresses of the beam elements are consistent with the structural behaviour described in the previous sections.

A [mm]	B [mm]	C [mm]	D [mm]	th [mm]	th_{floor} [mm]
23.18	25.68	28.35	18.53	0.93	1.37

Table 5.2: Optimization output for the cylindrical model

It can be observed that all the constraints related to the Failure Indices and the First Natural Frequency are satisfied. In particular, several FI values approach unity, for instance the FI of the floor beams in load case S2 and the FI of the shell plates in load case S3. This suggests that, for the selected configuration, the parameters A and B defining the cross-sections of the stringers and frames, as well as the shell thickness (th), were constrained during the optimization process by load cases S2 and S3, respectively. It can be observed that, in general, the pillars remain well below their FI limit. This suggests that their cross-sections could likely have been further reduced in order to achieve additional mass savings. One possible reason why the optimizer did not identify such a solution is that the pillars contribute only marginally to the total structural mass compared to the other structural components (see Figure 5.11).

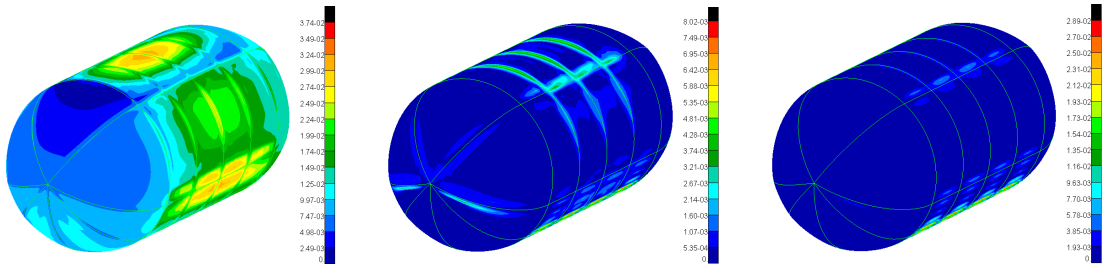

(a) Displacement - S1 **(b)** Displacement - S2 **(c)** Displacement - S3

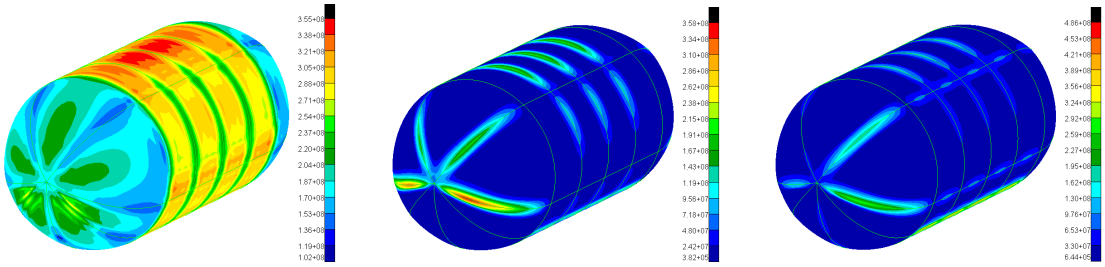

(d) Stress (Von Mises) - S1 **(e)** Stress (Von Mises) - S2 **(f)** Stress (Von Mises) - S3

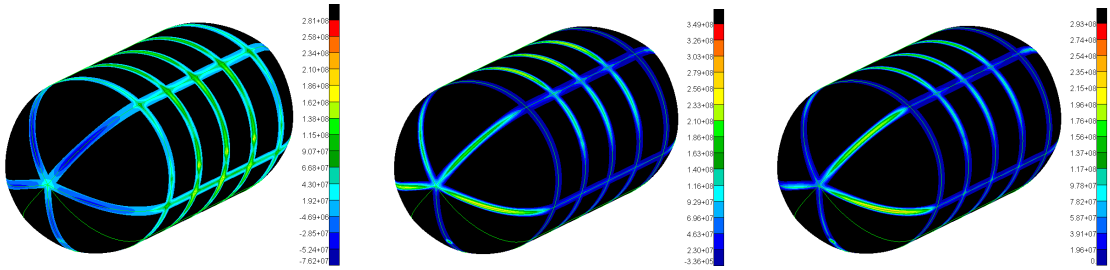

(g) Stress (Maximum stress in beams) - S1 **(h)** Stress (Maximum stress in beams) - S2 **(i)** Stress (Maximum stress in beams) - S3

Figure 5.10: Contour plots of the optimized cylindrical configuration in the outer shell region

Output	Value	Output	Value	Output	Value
Load case S1					
Displ. (shell) [m]	0.0374	Displ. (floor) [m]	0.0223	Displ. (pil) [m]	0.0008
FI beams (shell) [–]	0.974	FI beams (floor) [–]	0.505	FI beams (pil) [–]	0.098
FI plate (shell) [–]	0.757	FI plate (floor) [–]	0.131		
Load case S2					
Displ. (shell) [m]	0.0080	Displ. (floor) [m]	0.0321	Displ. (pil) [m]	0.0028
FI beams (shell) [–]	0.717	FI beams (floor) [–]	0.999	FI beams (pil) [–]	0.089
FI plate (shell) [–]	0.936	FI plate (floor) [–]	0.209		
Load case S3					
Displ. (shell) [m]	0.0289	Displ. (floor) [m]	0.0304	Displ. (pil) [m]	0.0018
FI beams (shell) [–]	0.588	FI beams (floor) [–]	0.941	FI beams (pil) [–]	0.062
FI plate (shell) [–]	0.998	FI plate (floor) [–]	0.228		
Global					
FNF [Hz]	31.07	Mass [kg]	327.2	V_{hab} [m^3]	29.45
V_{st} [m^3]	5.87	A_{floor} [m^2]	10.29	Walkable area [%]	100

Table 5.3: Structural analysis results of the optimized cylindrical model

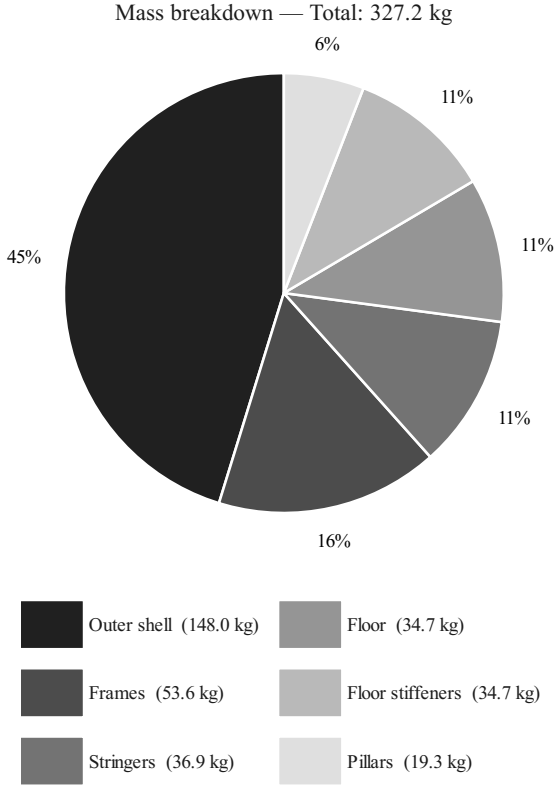

Figure 5.11: Mass breakdown optimized cylindrical configuration

5.2 Primary Structure - Ellipsoid

The results will first be presented for a spherical rover, and subsequently the variation of the semi-axes a, b and c will be analysed.

Considering the influence of the radius and the floor height on the geometric characteristics (Figure 5.12), it can be observed that the geometric requirements are satisfied only for transverse dimensions greater than 4 m, which exceed the launcher maximum cross-section constraint of 3.63 m. The sizing procedure therefore proceeds by excluding this requirement, since it is arbitrarily dictated by the choice of launcher and could be satisfied by future launch systems.

The requirement on the usable floor area is particularly restrictive for this geometry, as the sphere develops more in the vertical direction than the cylinder considered previously. For this reason, the combination of r and h_{floor} must be selected carefully.

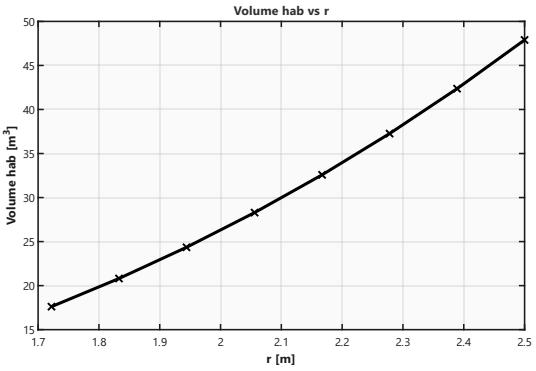

(a) Habitable volume (r)

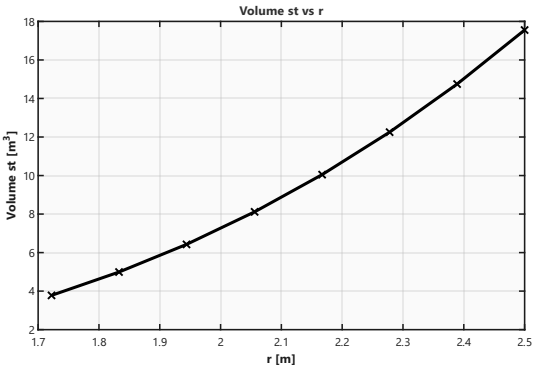

(b) Stowage volume (r)

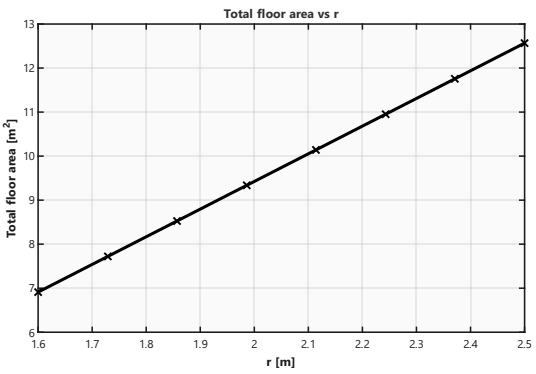

(c) Floor area (r)

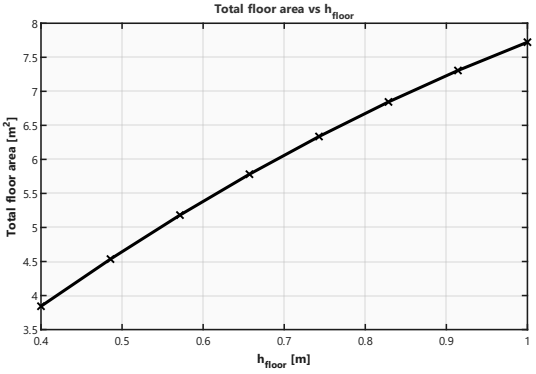

(d) Floor area (h_{floor})

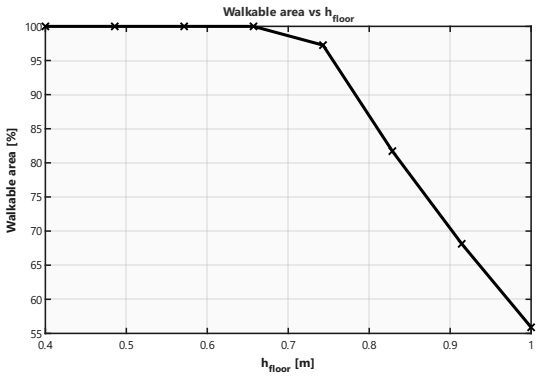

(e) Walkable area (h_{floor})

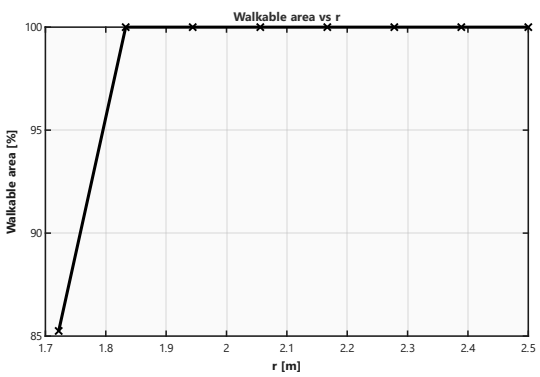

(f) Walkable area (r)

Figure 5.12: Geometrical results for the spherical model: V_{hab}, A_{floor}, $h_{\text{hab, 2 m}}$

The effect of the shell thickness can be observed in Figure 5.13. As the thickness increases, a beneficial effect for each load case is obtained, resulting in a reduction of stresses (and therefore of the failure indices). As expected, the most significant effect is observed in the FI of the CQUAD elements (Figure 5.13b), where very small thickness values lead to extremely high FI values.

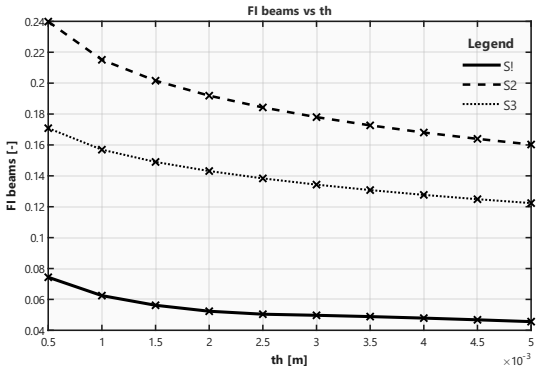

(a) FI beams (th)

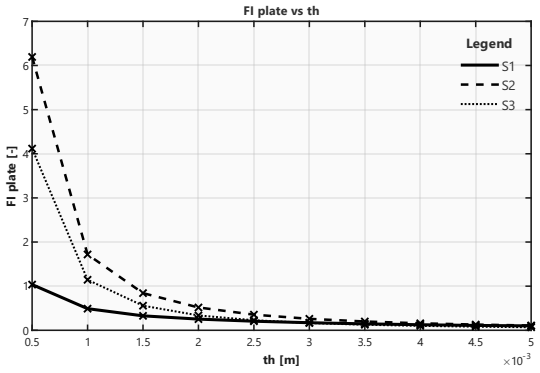

(b) FI plates (th)

Figure 5.13: Effect of shell thickness on the spherical model

Regarding the effect of the number of stringers (Figure 5.14), opposite trends can be observed between the operational and the launch cases. For load cases S2 and S3, increasing the number of stringers produces a beneficial effect, reducing both stresses and displacements. In contrast, the opposite trend is observed for case S1, where increasing the number of stringers leads to a deterioration of the structural response.

This behaviour can be explained by the fact that the structure is already well suited to withstand pressure loads, which represent the dominant loading condition in case S1. Due to the spherical geometry, the shell efficiently carries the internal pressure through membrane stresses, allowing the load to be distributed uniformly over the entire structure. As a consequence, additional stiffening elements provide little structural benefit when considering this loading condition alone.

In particular, the stringers are oriented parallel to the floor, while the maximum displacement in this case is not caused by the pressure load, since it is already optimally supported by the spherical shell, but rather by the vertical acceleration in the y direction. Due to their orientation, the stringers do not significantly increase the stiffness along this direction, and the effect of their added mass becomes dominant. In the other cases, where the load distribution and boundary conditions differ, the stringers are able to contribute more effectively to the structural stiffness, leading to an improvement in the overall structural response.

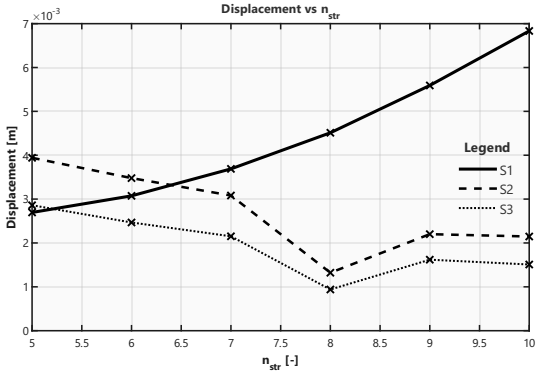

(a) Displacement (n_{str})

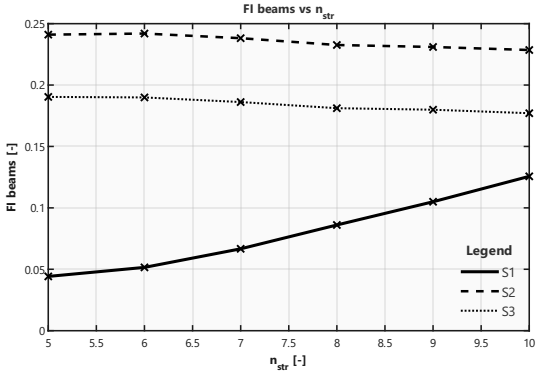

(b) FI beams (n_{str})

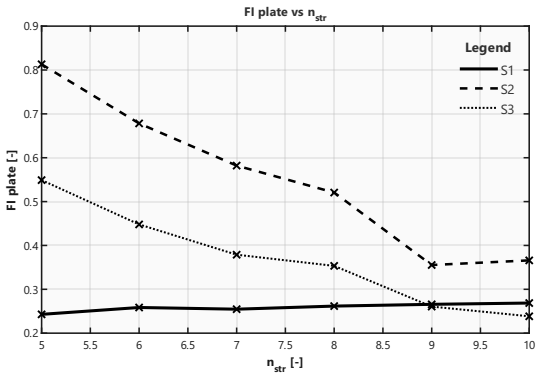

(c) FI plates (n_{str})

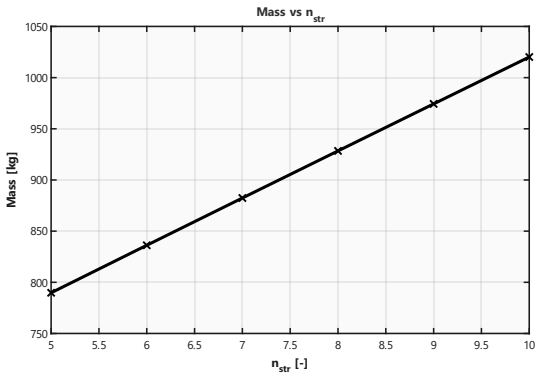

(d) Mass (n_{str})

Figure 5.14: Effect of number of stringers on the spherical model

A similar behaviour is observed for the effect of the number of frames (Figure 5.15). In this case, for load case S1 the variation of n_{fr} produces a negligible change in the results, whereas for the other load cases a beneficial effect is again observed as the number of frames increases.

The reason is that, unlike the previous case, the stiffening elements are now oriented consistently with the direction of the acceleration load. As a result, the frames contribute to increasing the structural stiffness in the direction of the dominant load. This leads to a balance between the beneficial stiffening effect provided by the frames and the penalty associated with their additional mass.

These trends are strongly influenced by the chosen location of the boundary conditions. A more detailed investigation of their nature and positioning could therefore lead to different results. Since the analyses were carried out on parametric geometries, the constraints must be applied to elements whose location is independent of the geometric parameters. However, this is not always possible, as is the case of n_{str} and n_{fr}.

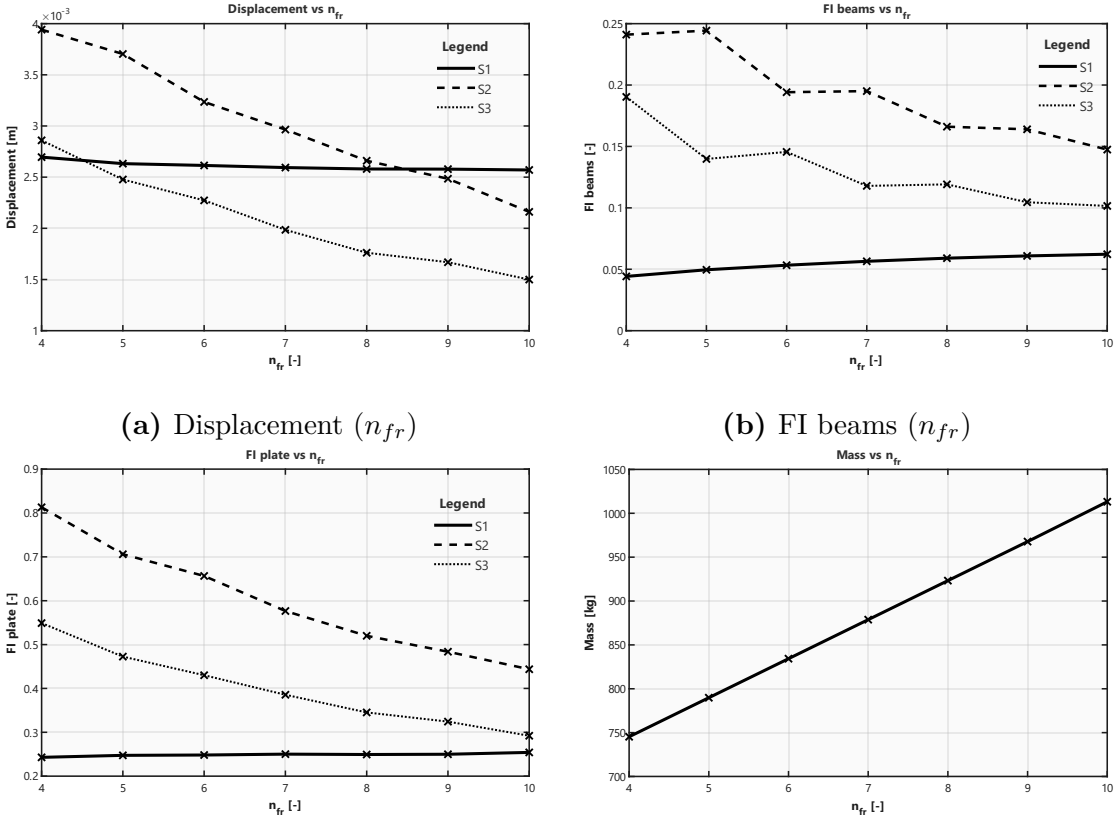

(a) Displacement (n_{fr})

(b) FI beams (n_{fr})

(c) FI plates (n_{fr})

(d) Mass (n_{fr})

Figure 5.15: Effect of number of frames on the spherical model

As shown in Figure 5.16, increasing the radius leads to a decrease in the FNF, similarly to what was previously observed for the cylindrical configuration. On the other hand, variations in the number of stringers do not significantly affect this value, whereas the number of frames has a much stronger influence.

This behaviour can be explained by considering that, during the launch phase, the boundary conditions were applied by constraining the upper and lower regions of the rover. These are the areas connected by the frames, which therefore contribute to increasing the structural stiffness of the system. Conversely, the stringers do not provide additional stiffness in that direction and are therefore largely ineffective in influencing the first natural frequency.

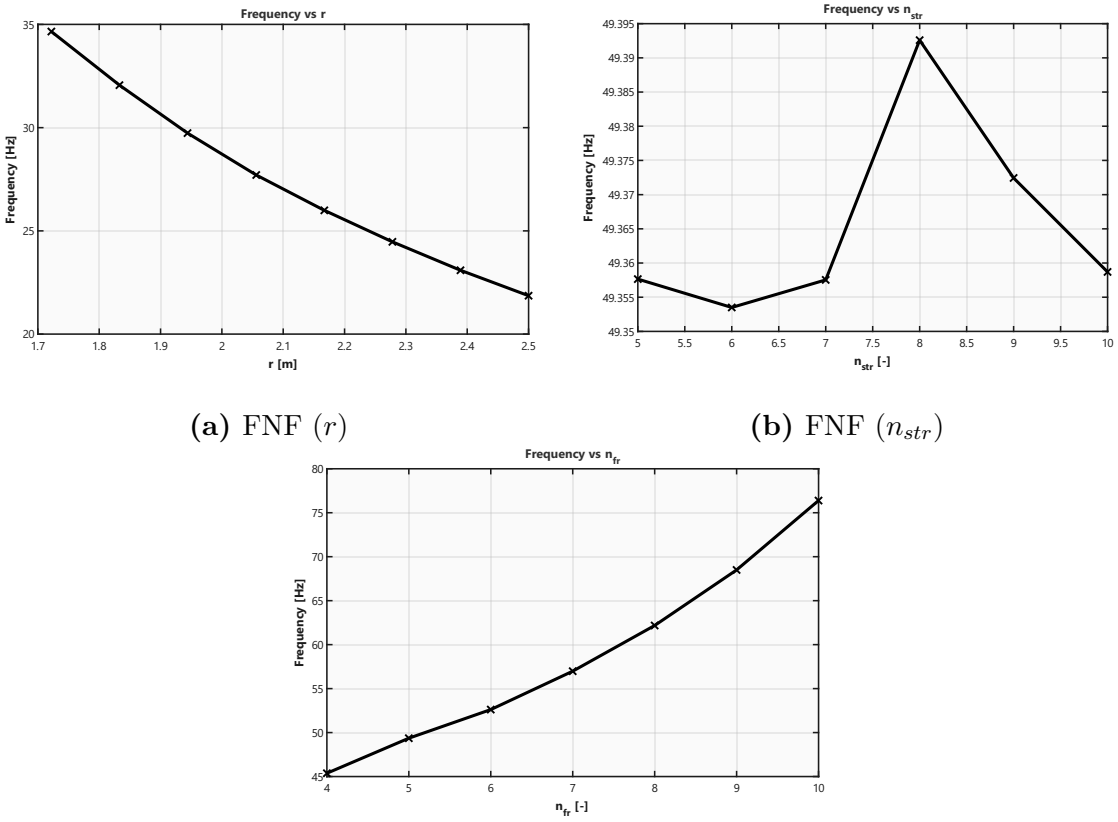

(a) FNF (r)

(b) FNF (n_{str})

(c) FNF (n_{fr})

Figure 5.16: Effect of FNF on spherical model

Finally, the effect of varying the section is also evaluated for this geometry (Figure 5.17). As observed previously for the cylindrical case, the configuration that performs best is the one closest to the spherical shape, which distributes pressure

loads more efficiently over the structure.

However, unlike the cylindrical case, adopting a geometry that deviates from the optimal spherical configuration may in some cases be advantageous in terms of internal space utilization. In fact, certain configurations allow the geometric constraints to be satisfied while requiring a lower structural mass. This aspect will be discussed in more detail in Section 5.2.1.

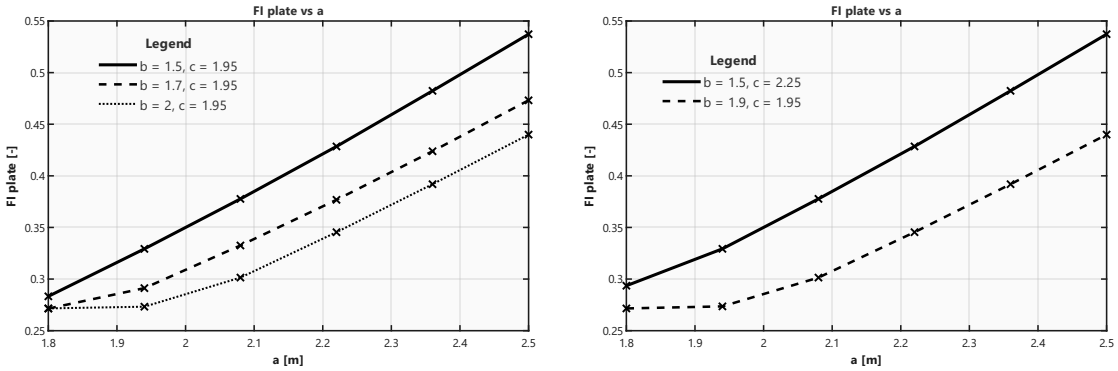

(a) FI plates (a, b) **(b)** FI plates (a, b, c)

Figure 5.17: Effect of ovalization of the spherical model

5.2.1 Ellipsoid optimization - Results

In order to illustrate the effect of geometric variations, a study was carried out on two different geometries: a spherical configuration and an ellipsoidal one (Figure 5.18). These geometries, whose main parameters are reported in Table 5.4, were selected so as to satisfy the geometric requirements:

Sphere:

- $V_{\text{hab}} = 29.45\,\text{m}^3 \geq 29.45\,\text{m}^3$
- $h_{\text{hab,2 m}} = 97.55\% \geq 75\%$
- $A_{\text{floor}} = 10\,\text{m}^2 \geq 10\,\text{m}^2$
- $V_{\text{stowage}} = 5.89\,\text{m}^3 \geq 0.758\,\text{m}^3$

Ellipsoid:

- $V_{\text{hab}} = 29.45\,\text{m}^3 \geq 29.45\,\text{m}^3$
- $h_{\text{hab,2 m}} = 91.94\% \geq 75\%$
- $A_{\text{floor}} = 10\,\text{m}^2 \geq 10\,\text{m}^2$
- $V_{\text{stowage}} = 3.56\,\text{m}^3 \geq 0.758\,\text{m}^3$

The optimization was carried out with a limit of 200 objective function evaluations for both geometries. Two configurations were obtained with the parameters reported in Table 5.4. The masses of the two models are 400.2 kg for the spherical configuration and 352.2 kg for the ellipsoidal one. These and the other results are

reported in Tables 5.6 and 5.7, respectively. The contour plots of the CQUAD and beam stresses (Pa) are shown in Figures 5.19 and 5.20.

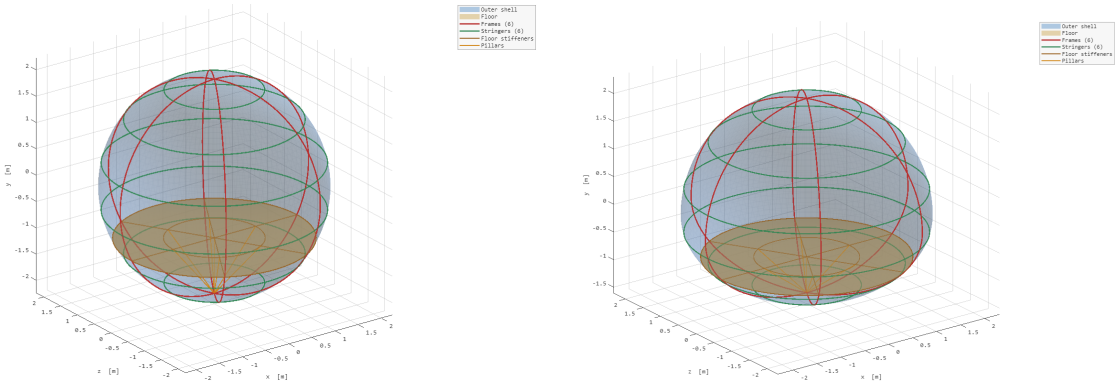

(a) Sphere **(b)** Ellipsoid

Figure 5.18: Spherical and ellipsoidal models geometry used for numerical optimization

Variable	Spherical	Ellipsoidal
a [m]	—	2.12
b [m]	—	2.10
c [m]	—	1.4063
r [m]	2.0358	—
h_{floor} [m]	1.0553	0.6467
n_{str}	6	6
n_{fr}	6	6
$n_{\text{str,floor}}$	1	1

Table 5.4: Geometrical parameters of the spherical and ellipsoidal models for the optimization

	A [mm]	B [mm]	C [mm]	D [mm]	th [mm]	th_{floor} [mm]
Sphere	10.68	20.06	49.68	19.05	1.17	3.53
Ellipsoid	9.52	20.90	49.21	10.74	0.87	4.32

Table 5.5: Optimization output for the spherical and ellipsoidal models

With regard to the spherical rover, the Von Mises stress on the shell can be observed to be uniformly distributed over the structure, indicating that the geometry

efficiently supports the internal pressure load. Consequently, load case S1 is not the critical condition for this configuration. Instead, the most critical case is the launch load case S2, in which the maximum stresses occur in the stringers that are perpendicular to the launcher acceleration.

Since both the geometry and the boundary conditions exhibit axial symmetry about the y axis, the structural stiffness is also distributed uniformly around it. As a result, because the magnitude of the acceleration in load case S3 is smaller than in load case S2, it is consistently less critical than the latter load case.

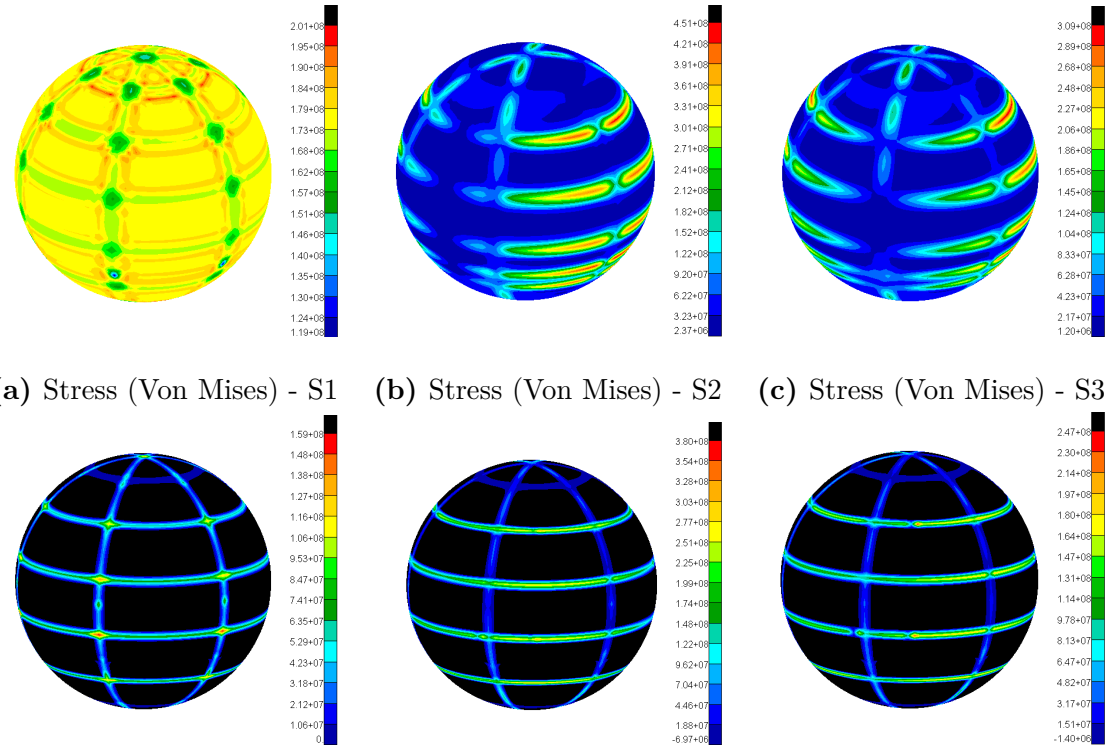

(a) Stress (Von Mises) - S1 **(b)** Stress (Von Mises) - S2 **(c)** Stress (Von Mises) - S3

(d) Stress (Maximum stress in beams) - S1 **(e)** Stress (Maximum stress in beams) - S2 **(f)** Stress (Maximum stress in beams) - S3

Figure 5.19: Contour plots of the optimized spherical configuration in the outer shell region

By examining the results of the ellipsoidal rover shown in Figure 5.20, the effect of the ovalization of the geometry becomes evident. In the stress distribution for load case S1 (Figure 5.20a), a marked inhomogeneity can be observed between the upper and lower caps. In particular, the lower cap experiences stresses that reach values up to twice those observed in the upper one. This behaviour is mainly

due to the difference in curvature between the two regions, which leads to a stress increase in the area where the structure is connected to the locomotive system.

By comparing this result with those obtained for load cases S2 and S3, it becomes clear that S1 is the most critical case for the shell elements, as it produces the highest stress levels. On the other hand, for the beam elements associated with the stiffeners, the launch load cases remain the most critical, particularly in the anchoring regions between the rover and the launcher.

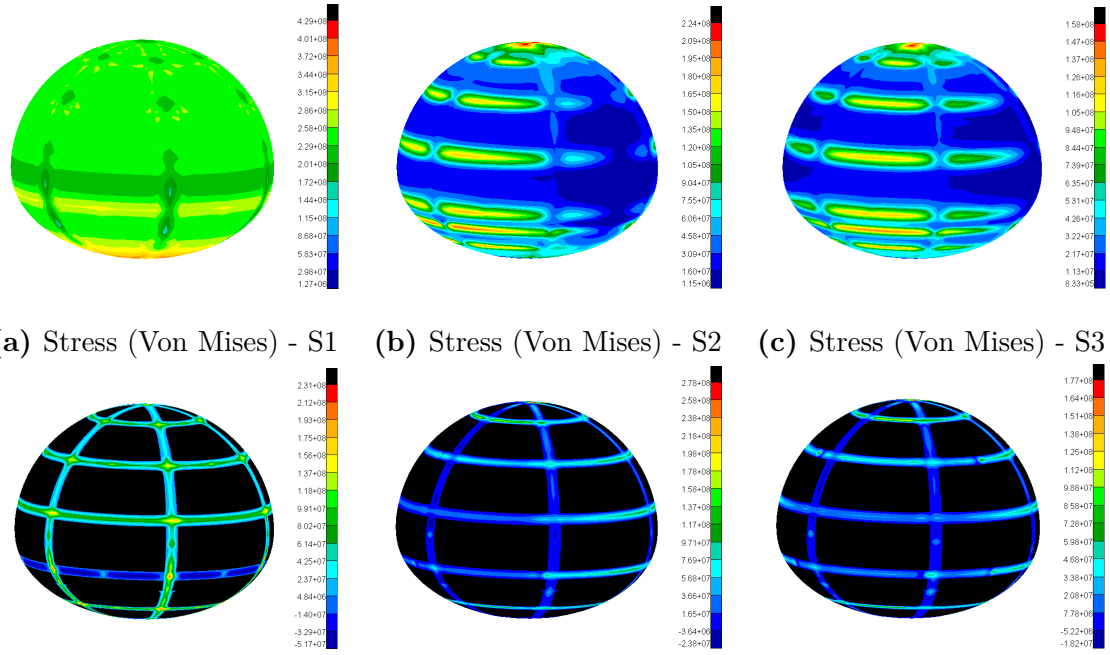

(a) Stress (Von Mises) - S1 **(b)** Stress (Von Mises) - S2 **(c)** Stress (Von Mises) - S3

(d) Stress (Maximum stress in beams) - S1 **(e)** Stress (Maximum stress in beams) - S2 **(f)** Stress (Maximum stress in beams) - S3

Figure 5.20: Contour plots of the optimized ellipsoidal configuration in the outer shell region

By examining the results tables, it can be observed that in both cases the limit imposed on the FNF is reached. This constraint therefore proves to be more critical than in the cylindrical configuration. In particular, as also shown in Figure 5.21, the first mode corresponds to a vibration mode of the floor, characterized in these cases by six half-waves, equal to the number of stiffeners that radiate from the centre of the floor.

This structural feature is also reflected in the optimization process, which prioritized a significant increase in the stiffness of floor-related parameters, such as the floor thickness th_{floor} and the cross-sectional dimensions of its stiffeners, represented

by the parameter D. These values are notably larger than those obtained in the optimization of the cylindrical configuration, highlighting their impact on the overall mass budget. As shown in Figure 5.22, the floor contributes 42 % and 53 % of the total structural mass for the spherical and ellipsoidal configurations, respectively, compared to just 22 % in the cylindrical case.

Looking at the values of the failure indices, and consistently with the contour plots, the spherical case exhibits the highest FI values in the outer shell region under load case S2, for both the 1D and 2D elements. In contrast, the ellipsoidal configuration shows significantly higher FI values in load case S1, in agreement with the behaviour previously observed.

Due to the over-dimensioning of the floor caused by the FNF constraint, the FI values in the floor region, as well as those of the pillars, remain very low in both models. This suggests that alternative floor stiffening strategies could play a key role in further reducing the total structural mass, for example by adopting a different distribution of the stiffeners or modifying their connection with the main structure.

Output	Value	Output	Value	Output	Value
Load case S1					
Displ. (shell) [m]	0.0049	Displ. (floor) [m]	0.0024	Displ. (pil) [m]	0.0001
FI beams (shell) [–]	0.470	FI beams (floor) [–]	0.041	FI beams (pil) [–]	0.010
FI plate (shell) [–]	0.448	FI plate (floor) [–]	0.014		
Load case S2					
Displ. (shell) [m]	0.0053	Displ. (floor) [m]	0.0313	Displ. (pil) [m]	0.0028
FI beams (shell) [–]	0.948	FI beams (floor) [–]	0.208	FI beams (pil) [–]	0.037
FI plate (shell) [–]	0.976	FI plate (floor) [–]	0.075		
Load case S3					
Displ. (shell) [m]	0.0037	Displ. (floor) [m]	0.0209	Displ. (pil) [m]	0.0017
FI beams (shell) [–]	0.685	FI beams (floor) [–]	0.122	FI beams (pil) [–]	0.022
FI plate (shell) [–]	0.621	FI plate (floor) [–]	0.055		
Global					
FNF [Hz]	25.09	Mass [kg]	400.2	V_{hab} [m^3]	29.45
V_{st} [m^3]	5.89	A_{floor} [m^2]	10.00	Walkable area [%]	97.55

Table 5.6: Structural analysis results of the optimized spherical model

Output	Value	Output	Value	Output	Value
Load case S1					
Displ. (shell) [m]	0.0216	Displ. (floor) [m]	0.0119	Displ. (pil) [m]	0.0058
FI beams (shell) [–]	0.916	FI beams (floor) [–]	0.051	FI beams (pil) [–]	0.049
FI plate (shell) [-]	0.994	FI plate (floor) [-]	0.018		
Load case S2					
Displ. (shell) [m]	0.0048	Displ. (floor) [m]	0.0065	Displ. (pil) [m]	0.0049
FI beams (shell) [–]	0.942	FI beams (floor) [–]	0.081	FI beams (pil) [–]	0.052
FI plate (shell) [–]	0.477	FI plate (floor) [–]	0.032		
Load case S3					
Displ. (shell) [m]	0.0032	Displ. (floor) [m]	0.0043	Displ. (pil) [m]	0.0030
FI beams (shell) [–]	0.646	FI beams (floor) [–]	0.048	FI beams (pil) [–]	0.030
FI plate (shell) [–]	0.344	FI plate (floor) [–]	0.021		
Global					
FNF [Hz]	25.05	Mass [kg]	352.2	V_{hab} [m^3]	29.45
V_{st} [m^3]	3.56	A_{floor} [m^2]	10.00	Walkable area [%]	91.93

Table 5.7: Structural analysis results of the optimized ellipsoidal model

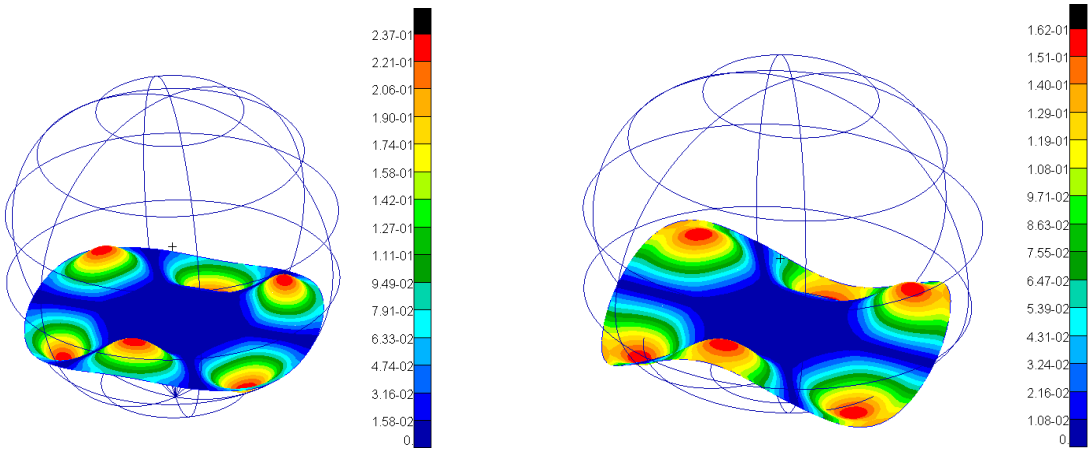

(a) Sphere **(b)** Ellipsoid

Figure 5.21: First natural frequency of spherical and ellipsoidal rover configurations

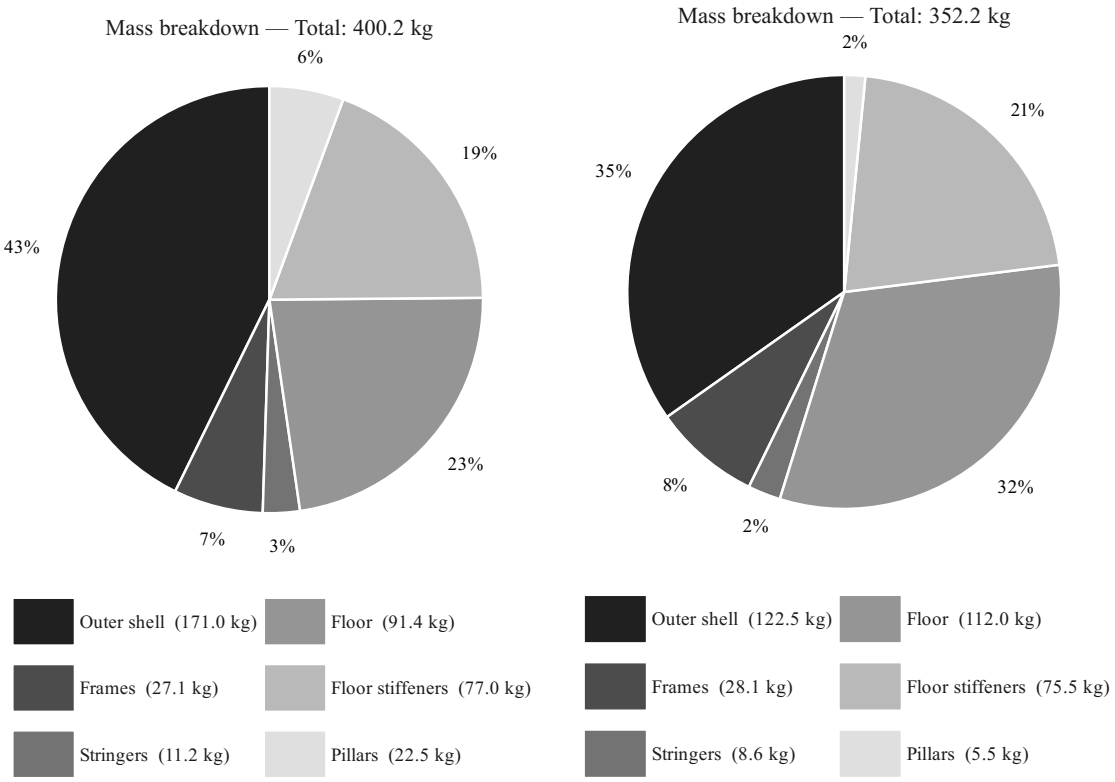

(a) Sphere **(b)** Ellipsoid

Figure 5.22: Mass breakdown optimized spherical and ellipsoidal configurations

Chapter 6

Final Remarks and Conclusion

This work presented the development of a parametric computational framework for the preliminary structural sizing of a pressurized lunar rover. The methodology integrates geometric modelling, finite element analysis, and surrogate-based optimization within a single automated workflow, and was applied to the comparative evaluation of cylindrical and ellipsoidal structural configurations.

Framework and Methodology

The principal contribution of this work is the development of an automated tool that, starting from a set of user-defined inputs, generates a finite element model of the rover, executes the required analyses in MSC Nastran, and collects and post-processes the results without manual intervention. The tool is implemented in Matlab and interfaced with MSC Patran through the automatic generation of session files written in PCL.

The framework supports three structural geometries: cylindrical, ellipsoidal and toroidal, and enables the parametric variation of both geometric quantities and structural properties. Four load cases are considered: three static analyses (ground testing and two launcher acceleration conditions) and one modal analysis for the evaluation of the first natural frequency.

The surrogate-based optimization strategy, implemented through Matlab's *surrogateopt* algorithm, proved effective in identifying minimum-mass structural configurations within the prescribed design space.

Optimization Results and Comparison

The optimization produced structurally admissible configurations for the cylindrical, spherical and ellipsoidal geometries, with total primary structural masses of respectively 327.2 kg, 400.2 kg, and 352.2 kg. All configurations satisfied the imposed constraints on failure indices and on the first natural frequency.

The cylindrical configuration achieved the lowest structural mass and the most balanced distribution among structural components. The critical load cases for the outer shell were S2 and S3 (launch), while S1 (pressurization) governed the sizing of the shell plates.

For the spherical rover, load case S2 was the critical condition for both shell plates and beam elements. This is because the spherical geometry responds extremely well to pressurization loads, which therefore do not govern the structural sizing, whereas the relatively high launch acceleration along the primary axis determines the maximum stresses. The ellipsoidal configuration, by contrast, showed S1 as the critical case for shell plates, with the asymmetric curvature amplifying the effect of internal pressure in the lower cap.

The comparison of the critical load cases highlights a broader design trade-off between the two geometries. While the spherical rover is theoretically superior for pressure containment, the ellipsoidal geometry allows a better management of the internal space, meeting all requirements while optimizing the usable volume.

Considering the discussed constraints, the most suitable shape for the selected mission is a cylinder with ellipsoidal end caps. This design optimizes internal space, reducing the rover's overall dimensions and, consequently, its total mass. Other benefits include easier integration within the launch vehicle fairing, improved manoeuvrability due to a generally lower centre of gravity compared to a fully ellipsoidal configuration, and simpler manufacturing, as the shape is considerably easier to construct.

Limitations and Future Developments

Several simplifications were introduced to make the framework practical at the preliminary design stage. The centralized mass model reduces the accuracy of local stress predictions under inertial loads; the adoption of a distributed subsystem mass model, once the layout of the rover is better defined, is expected to produce higher local stresses, particularly in load cases S2 and S3. The study on the distributed subsystem mass model confirmed this behaviour, showing that the current model underestimates peak stresses near mass attachment points.

The vibroacoustic analysis, which is essential for verifying structural survival under the acoustic loads induced during launch, was deliberately excluded from the main design loop due to the high computational cost of random response analyses. It should be performed on the final selected configuration as a verification step,

and its results may require the selection of an alternative configuration among the candidates identified by the optimizer. Other load conditions can also be considered, such as thermo-mechanical coupling, which can certainly induce additional stresses in the structure.

The present work focused on cylindrical and ellipsoidal geometries. While toroidal shapes may be relevant for future surface habitats, they were not included in the optimization campaign and represent a natural extension of this study. A promising direction for future work is the integration of parametric shape optimization with the current structural sizing approach, enabling simultaneous optimization of both geometric parameters and structural layout. This could lead to more refined and mass-efficient solutions.

Finally, the study assumed isotropic materials, currently the most reliable choice for preliminary structural design. Future developments could explore laminated composites or sandwich panels, which offer potential for reduced mass, higher structural efficiency, and greater design flexibility through tailored layer thicknesses and fibre orientations.

Overall Assessment

The framework developed in this work fulfils its stated objectives. It provides a flexible, automated, and scalable tool for the preliminary structural sizing of pressurized lunar rovers, capable of efficiently exploring a wide parametric design space and identifying minimum-mass solutions that satisfy all imposed structural and geometric constraints. The results obtained are physically consistent and provide a solid starting point for more detailed design phases.

Appendix A

Convergence analysis

In order to determine an appropriate mesh size for discretizing the model, a convergence study was performed. This analysis was carried out by varying the element length (for 1D elements) or the side length of square elements (for 2D elements). This quantity is referred to as the Global Edge Length (GEL), and in the plots shown it decreases along the horizontal axis.

Selecting a sufficiently small gel is essential to achieve the proper compromise between result accuracy and acceptable computational cost. Increasing the number of elements leads to a higher number of nodes (and therefore degrees of freedom), resulting in larger mass and stiffness matrices that require more time to solve the system.

A.1 Sphere

For the spherical geometry, a study was conducted by varying the mesh size from 0.5 m to 0.0125 m over 40 intervals. The trends are reported in Figure A.1; the parameters used for this analysis are listed in Table A.1. The variables s_i, f_i, fl_i, pl_i refer to the characteristic dimensions of the cross-sections used for the stringers, frames, floor and pillars, respectively. These cross-sections are also shown in Figure A.3. The material used for the outer shell, stringers, frames and pillars is Al7075 T6, while Al2090 T83 is used for the floor and its stiffeners.

It can be observed in Figure A.1 that for element sizes (GEL) greater than 0.45 m, the results are completely unreliable, as the excessive mesh size distorts the results significantly. The trend reaches a stabilization phase around 0.1 m; therefore, this mesh size will be adopted for the subsequent analyses.

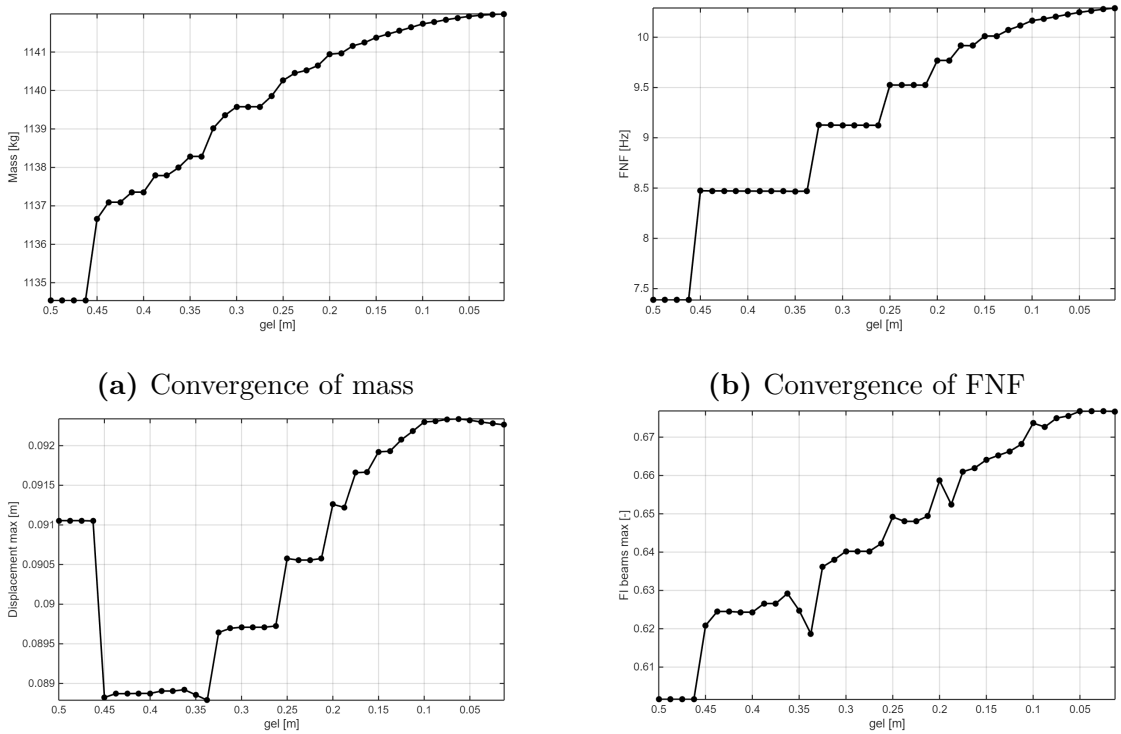

(a) Convergence of mass

(b) Convergence of FNF

(c) Convergence of displacement

(d) Convergence of FI (beam elements)

Figure A.1: Convergence of spherical model

Variable	Value	Variable	Value	Variable	Value	Variable	Value
$r[m]$	2.2	$s_6[m]$	0.015	$f_4[m]$	0.015	$fl_4[m]$	0.015
n_{str}	5	n_{fr}	6	$n_{str,floor}$	1	$pl_1[m]$	0.03
$s_1[m]$	0.06	$n_{fr,r}$	0	$th_{\text{floor}}[m]$	0.0025	$pl_2[m]$	0.015
$s_2[m]$	0.06	$n_{fr,f}$	0	$h_{\text{floor}}[m]$	0.8	$th[m]$	0.002
$s_3[m]$	0.06	$f_1[m]$	0.06	$fl_1[m]$	0.06		
$s_4[m]$	0.015	$f_2[m]$	0.06	$fl_2[m]$	0.06		
$s_5[m]$	0.015	$f_3[m]$	0.015	$fl_3[m]$	0.015		

Table A.1: Parameters used in the convergence study of the spherical model

A.2 Cylinder

Also for the cylindrical case, the mesh size was varied over a range from 0.5 m to 0.0125 m. The characteristics of the adopted geometric model are reported in Table A.2, using the same structural element cross-sections as in the spherical case

(Figure A.3) and the same materials. In this case, the results shown in Figure A.2 indicate that convergence is achieved at a mesh size of approximately 0.1 m.

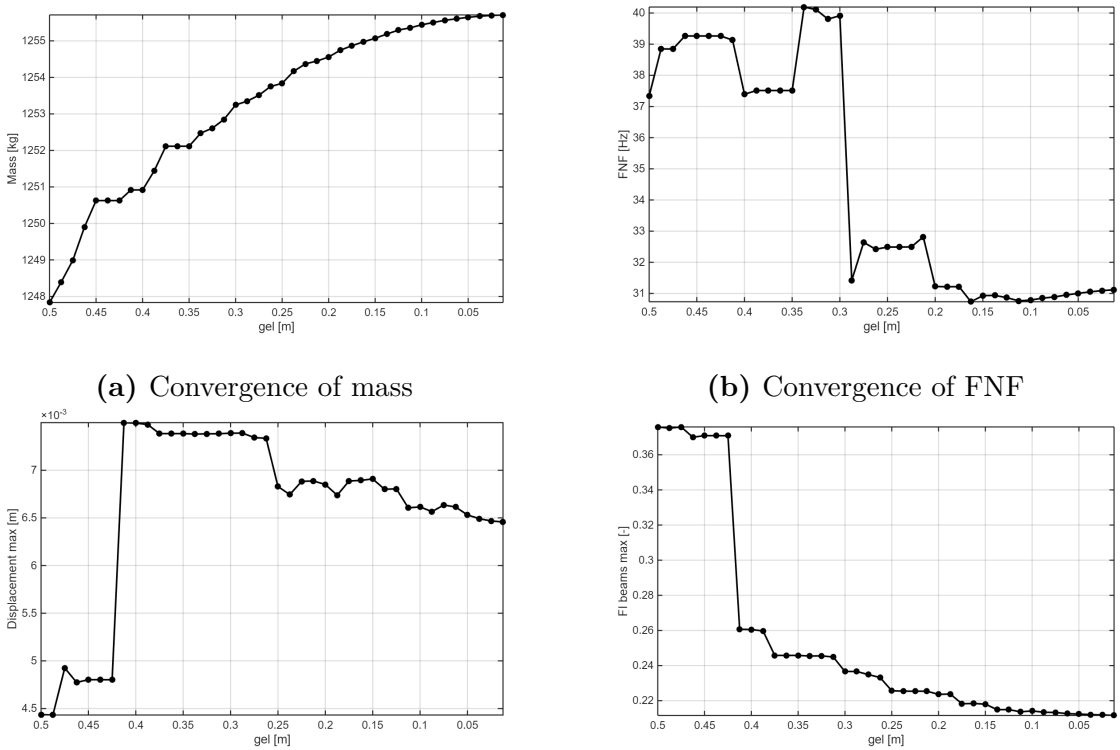

(a) Convergence of mass

(b) Convergence of FNF

(c) Convergence of displacement

(d) Convergence of FI (beam elements)

Figure A.2: Convergence of cylindrical model

Variable	Value	Variable	Value	Variable	Value	Variable	Value
r [m]	1.65	s_3 [m]	0.06	f_2 [m]	0.06	fl_2 [m]	0.06
h [m]	2.5	s_4 [m]	0.015	f_3 [m]	0.015	fl_3 [m]	0.015
$front$ [m]	1.65	s_5 [m]	0.015	f_4 [m]	0.015	fl_4 [m]	0.015
$rear$ [m]	1.65	s_6 [m]	0.015	$n_{str,floor}$	1	pl_1 [m]	0.03
n_{str}	5	n_{fr}	5	th_{floor} [m]	0.0025	pl_2 [m]	0.015
s_1 [m]	0.06	$n_{fr,r}$	0	h_{floor} [m]	0.8	th [m]	0.002
s_2 [m]	0.06	$n_{fr,f}$	0	f_1 [m]	0.06	fl_1 [m]	0.06

Table A.2: Parameters used in the convergence study of the cylindrical model

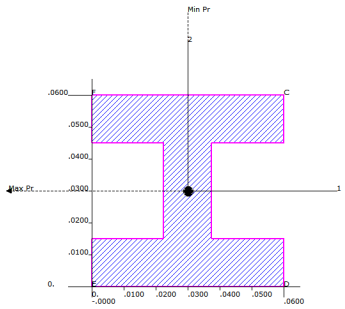

(a) Stringers section

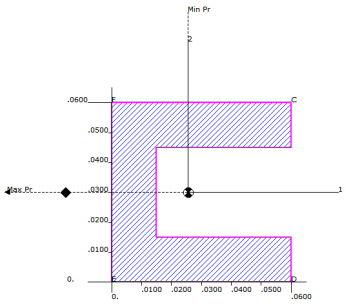

(b) Frames section

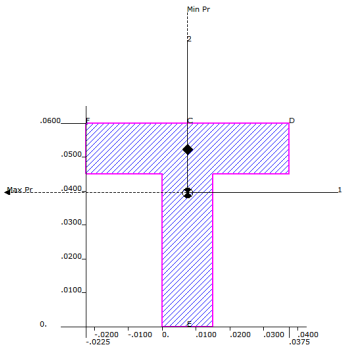

(c) Floor stiffeners section

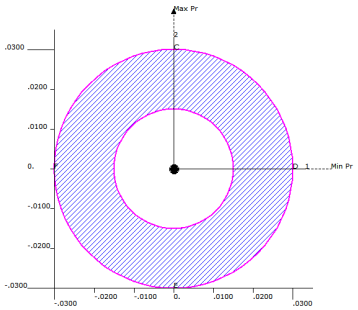

(d) Pillars section

Figure A.3: Sections selected for the convergence study and the parametric analysis

Appendix B

Distributed subsystem mass modelling

Up to this point, the results presented referred to the model in which all subsystem masses are concentrated at a single point, connected to the structural stiffeners. This approach is necessary when dealing with a variable-geometry model, since changes in the geometry affect the number and the location of the connections between subsystems and the structure. This would inevitably lead to trends that are difficult to interpret when adopting an approach such as the one proposed for preliminary sizing. Moreover, defining the exact location of these subsystems would not be appropriate at this stage, as it belongs to later phases of the design process.

Figure B.1 shows contour plots of the displacement (in mm). It can be observed that for load case S1 the difference between the deformations is not particularly pronounced, except for slight asymmetries caused by the distribution of the internal subsystems. This is no longer the case for load cases S2 and S3, where the deformation becomes about one order of magnitude higher in correspondence with the heaviest subsystems. This can be seen, for example, in Figure B.1d, where peaks appear near the attachment region of the seat and the hygiene system. In the final design, the interface regions between the structure and the subsystems will obviously require additional stiffening; therefore, these results are not particularly meaningful at this stage of the design process.

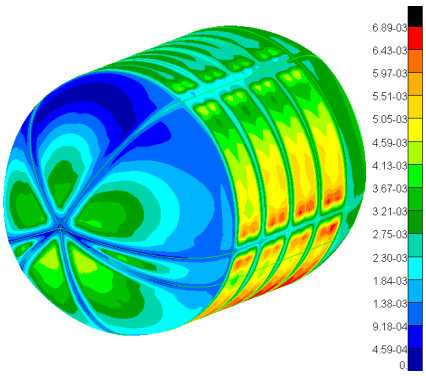

(a) Centralized model - S1

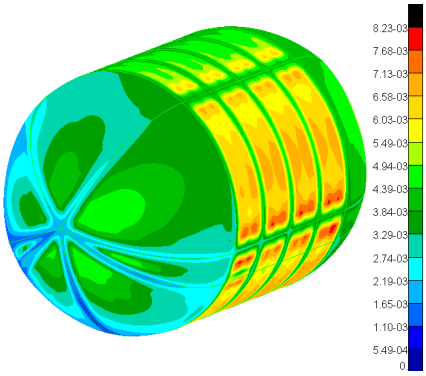

(b) Distributed model - S1

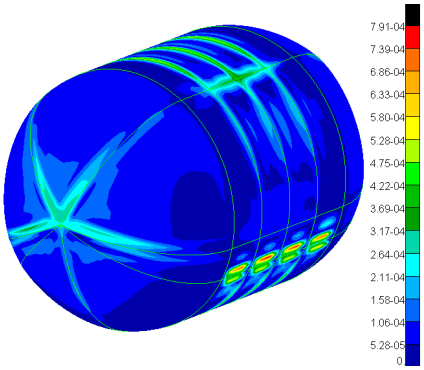

(c) Centralized model - S2

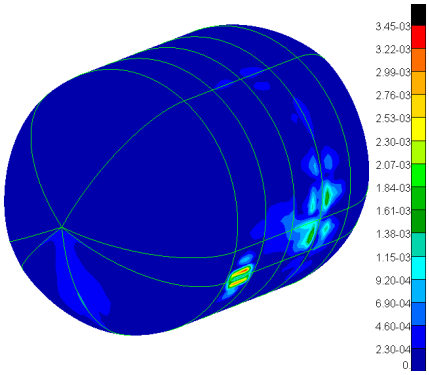

(d) Distributed model - S2

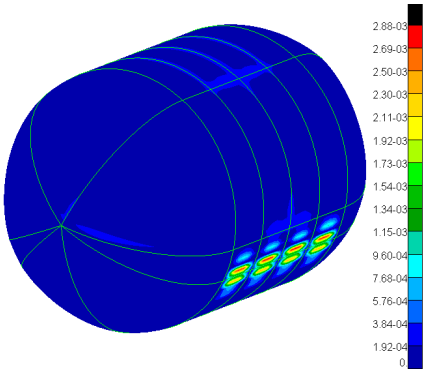

(e) Centralized model - S3

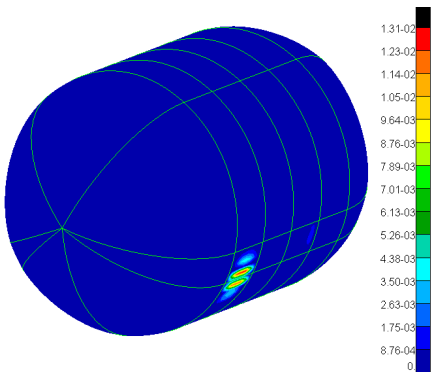

(f) Distributed model - S3

Figure B.1: Displacement comparison between the centralized and distributed models

With regard to the Von Mises stresses in the pressurized shell (shown in Figure B.2 in Pa), the same considerations made for the displacements apply. No significant difference can be observed for load case S1, since the primary load in this case is the internal pressurization, which is not affected by the distribution of the subsystems. In contrast, the maximum stresses for S2 and S3 increase significantly, locally even exceeding the stress levels observed in S1. This is consistent with the state of the art, as the governing load for structures of this type is often associated with launch conditions rather than operational phases.

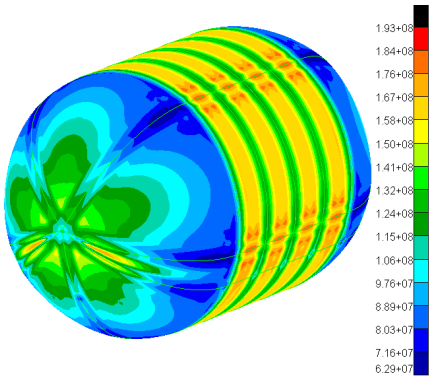

(a) Centralized model - S1

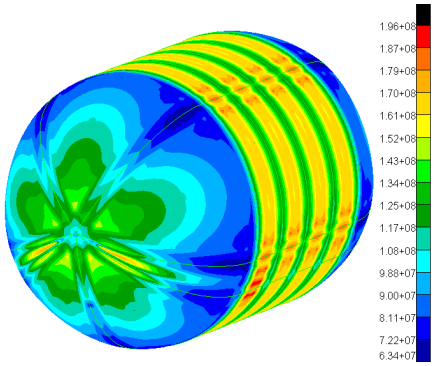

(b) Distributed model - S1

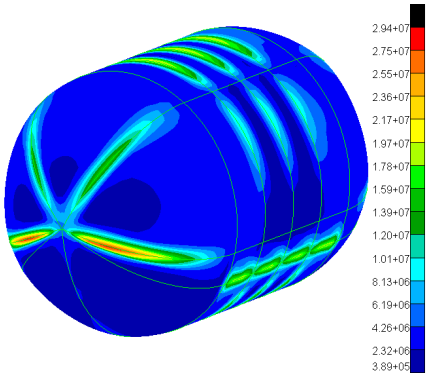

(c) Centralized model - S2

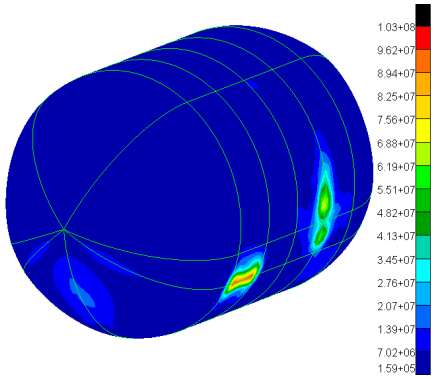

(d) Distributed model - S2

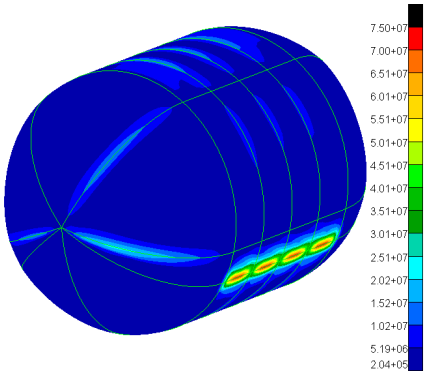

(e) Centralized model - S3

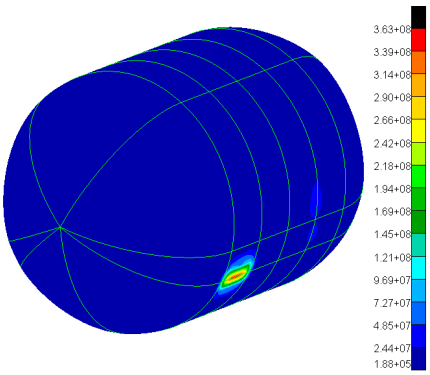

(f) Distributed model - S3

Figure B.2: Von Mises stress comparison between the centralized and distributed models

Figure B.3 shows the distribution of the maximum stress values in the beam elements (in Pa). In MSC Nastran, the maximum beam stress corresponds to the maximum combined normal stress evaluated at the beam section output points, accounting for axial and bending contributions.

Consistent with the observations for the 2D element stresses, the 1D elements also show little difference between the two models for load case S1. For the other two load cases, however, a stress peak appears in the distributed model due to the transfer of subsystem inertia at their interface points, which correspond to the beam elements. In particular, the maximum stress rises by 219 % for S2 and by 160 % for S3.

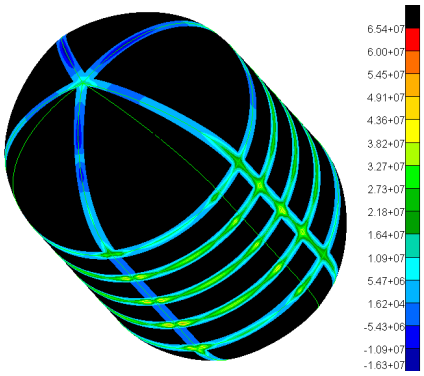

(a) Centralized model - S1

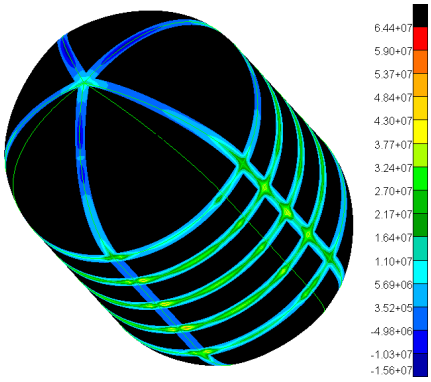

(b) Distributed model - S1

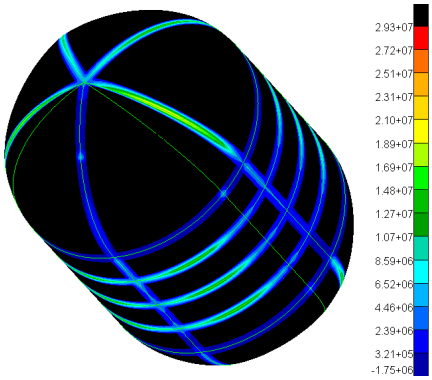

(c) Centralized model - S2

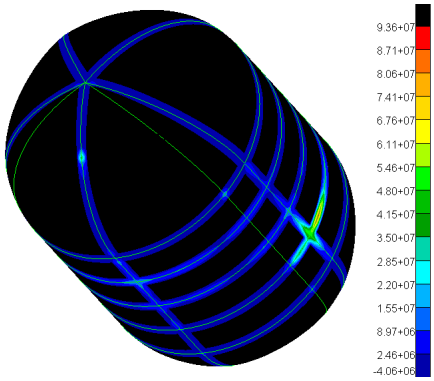

(d) Distributed model - S2

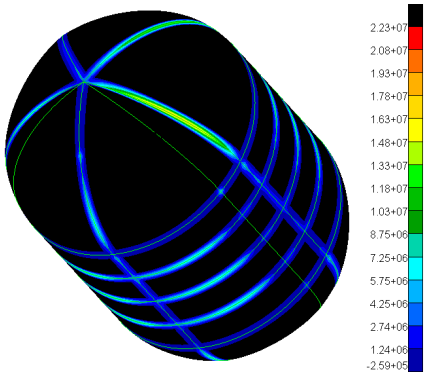

(e) Centralized model - S3

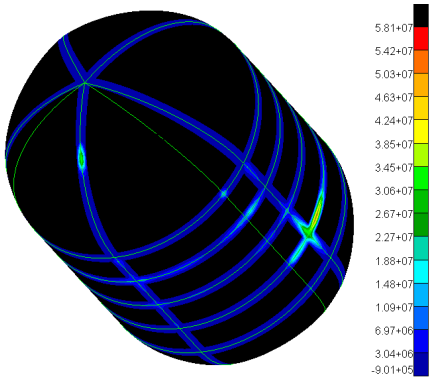

(f) Distributed model - S3

Figure B.3: Beam stress comparison between the centralized and distributed models

Bibliography

[1] M. Smith, D. Craig, N. Herrmann, E. Mahoney, J. Krezel, N. McIntyre, and K. Goodliff. «The Artemis Program: An Overview of NASA's Activities to Return Humans to the Moon». In: *2020 IEEE Aerospace Conference*. Big Sky, MT, USA: IEEE, Mar. 2020, pp. 1–10. DOI: 10.1109/AERO47225.2020.9172323. URL: https://ieeexplore.ieee.org/document/9172323/.

[2] T. Hu, Z. Yang, M. Li, C. H. Van Der Bogert, Z. Kang, X. Xu, and H. Hiesinger. «Possible sites for a Chinese International Lunar Research Station in the Lunar South Polar Region». In: *Planetary and Space Science* 227 (Mar. 2023), p. 105623. DOI: 10.1016/j.pss.2022.105623. URL: https://linkinghub.elsevier.com/retrieve/pii/S0032063322002094.

[3] S. Jester and H. Falcke. «Science with a lunar low-frequency array: From the dark ages of the Universe to nearby exoplanets». In: *New Astronomy Reviews* 53.1 (May 2009), pp. 1–26. DOI: 10.1016/j.newar.2009.02.001. URL: https://linkinghub.elsevier.com/retrieve/pii/S1387647309000086.

[4] M. Anand, I. Crawford, M. Balat-Pichelin, S. Abanades, W. Van Westrenen, G. Péraudeau, R. Jaumann, and W. Seboldt. «A brief review of chemical and mineralogical resources on the Moon and likely initial in situ resource utilization (ISRU) applications». In: *Planetary and Space Science* 74.1 (Dec. 2012), pp. 42–48. DOI: 10.1016/j.pss.2012.08.012. URL: https://linkinghub.elsevier.com/retrieve/pii/S0032063312002498.

[5] K. Seweryn, A. Kolusz, I. Świca, A. Tkacz, A. Gallina, J. Katzer, J. Kobaka, P. Konecny, and P. Młynarczyk. «A Conceptual Open Pit Mine Architecture for the Moon Environment». In: *Artificial Satellites* 59.1 (Mar. 1, 2024), pp. 11–41. DOI: 10.2478/arsa-2024-0002. URL: https://www.sciendo.com/article/10.2478/arsa-2024-0002.

[6] R. Chen, X. Wang, S. Yuan, H. Chen, F. Gao, and L. Kong. «A solution of lunar manufacturing and launch base». In: *Acta Astronautica* 236 (Nov. 2025), pp. 897–903. DOI: 10.1016/j.actaastro.2025.07.035. URL: https://linkinghub.elsevier.com/retrieve/pii/S0094576525004655.

[7] G. L. Kulcinski and H. H. Schmitt. «The moon: An abundant source of clean and safe fusion fuel for the 21st century». In: International Scientific Forum on Fueling the 21st Century. NASA, Sept. 1, 1988. URL: https://ntrs.nasa.gov/citations/19890005472.

[8] J. Zakrajsek et al. «Exploration Rover Concepts and Development Challenges». In: 1 (Apr. 2005). DOI: 10.2514/6.2005-2525.

[9] S. F. Morea. «The Lunar Roving Vehicle: Historical perspective». In: Sept. 1, 1992. URL: https://ntrs.nasa.gov/citations/19930004820?utm_source=chatgpt.com.

[10] K. Creel, J. Frampton, D. Honaker, K. Mcclure, and M. Zeinali. *Pressurized Lunar Rover*. NASA-CR-192034. May 1, 1992. URL: https://ntrs.nasa.gov/citations/19930008826.

[11] M. Bhardwaj, V. Bulsara, D. Kokan, S. Shariff, E. Svarverud, and R. Wirz. «Design of a pressurized lunar rover». In: (May 1992).

[12] S. J. Hoffman and D. I. Kaplan. *Human Exploration of Mars: The Reference Mission of the NASA Mars Exploration Study Team*. July 1, 1997. URL: https://ntrs.nasa.gov/citations/19980037039 (visited on 03/18/2026).

[13] D. Akin and M. Bowden. «MORPHLAB: Modular Roving Planetary Habitat, Laboratory, and Base». In: Sept. 2004. DOI: 10.2514/6.2004-6034.

[14] F. B. Leahy. *Cross-Program Design Specification for Natural Environments (DSNE)*. Oct. 27, 2021. URL: https://ntrs.nasa.gov/citations/20210024522.

[15] G. H. Heiken, D. T. Vaniman, and B. M. French. *Lunar Sourcebook*. Cambridge University Press, 1991.

[16] R. B. Malla and K. M. Brown. «Determination of temperature variation on lunar surface and subsurface for habitat analysis and design». In: *Acta Astronautica* 107 (Feb. 2015), pp. 196–207. DOI: 10.1016/j.actaastro.2014.10.038. URL: https://linkinghub.elsevier.com/retrieve/pii/S0094576514004160.

[17] A. Z. Howard and S. Stewart. «Thermal Impacts of Lunar Dust For Rovers». In: Cleveland, OH, Aug. 1, 2024. URL: https://ntrs.nasa.gov/citations/20240009989.

[18] E. Grün, H. Zook, H. Fechtig, and R. Giese. «Collisional balance of the meteoritic complex». In: *Icarus* 62.2 (May 1985), pp. 244–272. DOI: 10.1016/0019-1035(85)90121-6. URL: https://linkinghub.elsevier.com/retrieve/pii/0019103585901216.

[19] A. Saponaro. «Development of a modular multi-DOF motion simulator for a pressurized lunar rover». Master thesis. Turin, Italy: Polytechnic of Turin, 2026.

[20] SpaceX. *Falcon 9 User's Guide*. Version 8. Mar. 2025. URL: https://www.spacex.com/assets/media/falcon-users-guide-2025-05-09.pdf.

[21] National Aeronautics and Space Administration. *Human Integration Design Handbook*. NASA/SP-2010-3407/REV1. Revision 1. NASA. 2014.

[22] C.-S. Kang. «Multilayer Insulation for Spacecraft Applications». In: *COSPAR Colloquia Series*. Vol. 10. Elsevier, 1999, pp. 175–179. DOI: 10.1016/S0964-2749(99)80023-7. URL: https://linkinghub.elsevier.com/retrieve/pii/S0964274999800237.

[23] T. L. Bergman and A. S. Lavine. *Fundamentals of heat and mass transfer*. Eighth edition. Hoboken, NJ: John Wiley & Sons, 2017.

[24] M. M. Finckenor and D. Dooling. *Multilayer Insulation Material Guidelines*. Tech. rep. NASA/TP-1999-209263. Huntsville, AL: NASA Marshall Space Flight Center, 1999.

[25] S. Q. Zeng, A. J. Hunt, W. Cao, and R. Greif. «Pore Size Distribution and Apparent Gas Thermal Conductivity of Silica Aerogel». In: *Journal of Heat Transfer* 116.3 (Aug. 1, 1994), pp. 756–759. DOI: 10.1115/1.2910933. URL: https://asmedigitalcollection.asme.org/heattransfer/article/116/3/756/383213/Pore-Size-Distribution-and-Apparent-Gas-Thermal.

[26] B. Notario, J. Pinto, E. Solorzano, J. De Saja, M. Dumon, and M. Rodríguez-Pérez. «Experimental validation of the Knudsen effect in nanocellular polymeric foams». In: *Polymer* 56 (Jan. 2015), pp. 57–67. DOI: 10.1016/j.polymer.2014.10.006. URL: https://linkinghub.elsevier.com/retrieve/pii/S0032386114009021.

[27] N. Bheekhun, A. R. Abu Talib, and M. R. Hassan. «Aerogels in Aerospace: An Overview». In: *Advances in Materials Science and Engineering* 2013 (2013), pp. 1–18. DOI: 10.1155/2013/406065. URL: http://www.hindawi.com/journals/amse/2013/406065/.

[28] K. Wen, X.-w. Chen, and Y.-g. Lu. «Research and development on hypervelocity impact protection using Whipple shield: An overview». In: *Defence Technology* 17.6 (Dec. 2021), pp. 1864–1886. DOI: 10.1016/j.dt.2020.11.005. URL: https://linkinghub.elsevier.com/retrieve/pii/S2214914720304724.

[29] E. L. Christiansen et al. *Handbook for Designing MMOD Protection*. JSC-64399. Houston, Texas: NASA Johnson Space Center, Jan. 2009. URL: https://ntrs.nasa.gov/api/citations/20090010053/downloads/20090010053.pdf.

[30] M. A. Rakib, S. T. Smith, and T. Tafsirojjaman. «A review of shielding systems for protecting off-earth structures from micrometeoroid and orbital debris impact». In: *Acta Astronautica* 223 (Oct. 2024), pp. 404–425. DOI: 10.1016/j.actaastro.2024.07.019. URL: https://linkinghub.elsevier.com/retrieve/pii/S0094576524003874.

[31] E. L. Christiansen and J. H. Kerr. «Mesh double-bumper shield: A low-weight alternative for spacecraft meteoroid and orbital debris protection». In: *International Journal of Impact Engineering* 14.1 (Jan. 1993), pp. 169–180. DOI: 10.1016/0734-743X(93)90018-3. URL: https://linkinghub.elsevier.com/retrieve/pii/0734743X93900183.

[32] K. Fowler and F. Teixeira-Dias. «Hybrid Shielding for Hypervelocity Impact of Orbital Debris on Unmanned Spacecraft». In: *Applied Sciences* 12.14 (July 13, 2022), p. 7071. DOI: 10.3390/app12147071. URL: https://www.mdpi.com/2076-3417/12/14/7071.

[33] B. Pang, W. Zhang, D. Luo, and Z. Zhang. «Experimental investigation into water-filled pressurized vessels damaged by high-velocity projectile impact». In: *Proceedings of the Third European Conference on Space Debris*. Darmstadt, Germany, 2001, pp. 603–606.

[34] P. Zhang, K. Xu, M. Li, Z. Gong, G. Song, Q. Wu, Y. Cao, D. Tian, and Z. Yu. «Study of the shielding performance of a Whipple shield enhanced by Ti-Al-nylon impedance-graded materials». In: *International Journal of Impact Engineering* 124 (Feb. 2019), pp. 23–30. DOI: 10.1016/j.ijimpeng.2018.08.005. URL: https://linkinghub.elsevier.com/retrieve/pii/S0734743X18302872.

[35] J. Wilson, F. Cucinotta, J. Miller, J. Shinn, S. Thibeault, R. Singleterry, L. Simonsen, and M. Kim. «Materials for Shielding Astronauts from the Hazards of Space Radiations». In: *MRS Proceedings* 551 (Jan. 1998). DOI: 10.1557/PROC-551-3.

[36] G. Sinclair and J. Helms. «A review of simple formulae for elastic hoop stresses in cylindrical and spherical pressure vessels: What can be used when». In: *International Journal of Pressure Vessels and Piping* 128 (Apr. 2015), pp. 1–7. DOI: 10.1016/j.ijpvp.2015.01.006. URL: https://linkinghub.elsevier.com/retrieve/pii/S0308016115000071.

[37] T. Yasaka and J. Onoda. «Spacecraft Structures». In: *Encyclopedia of Physical Science and Technology (Third Edition)*. Ed. by R. A. Meyers. Third Edition. New York: Academic Press, 2003, pp. 449–461. DOI: https://doi.org/10.1016/B0-12-227410-5/00899-1. URL: https://www.sciencedirect.com/science/article/pii/B0122274105008991.

[38] M. Z. Naser and A. I. Chehab. «Materials and design concepts for space-resilient structures». In: *Progress in Aerospace Sciences* 98 (2018), pp. 74–90. DOI: https://doi.org/10.1016/j.paerosci.2018.03.004. URL: https://www.sciencedirect.com/science/article/pii/S0376042118300150.

[39] NASA. *Structural Design and Test Factors of Safety for Spaceflight Hardware*. NASA-STD-5001B W/CHANGE 3. Washington, DC, Oct. 2022.

[40] B. C. Di Maggio. «Multidisciplinary Design and Optimization of a Pressurized Rover for Lunar Surface Exploration». Master thesis. Turin, Italy: Polytechnic of Turin, 2026.

[41] M. Rudisill, R. Howard, B. Griffin, J. Green, L. Toups, and K. Kennedy. «Lunar Architecture Team: Phase 2 Habitat Volume Estimation: "Caution When Using Analogs"». In: *Earth and Space 2008*. 11th Biennial ASCE Aerospace Division International Conference on Engineering, Science, Construction, and Operations in Challenging Environments. Long Beach, California, United States: American Society of Civil Engineers, Sept. 4, 2008, pp. 1–11. DOI: 10.1061/40988(323)101. URL: http://ascelibrary.org/doi/10.1061/40988%28323%29101.

[42] European Committee for the Prevention of Torture and Inhuman or Degrading Treatment or Punishment (CPT). *Living Space per Prisoner in Prison Establishments: CPT Standards*. Strasbourg: Council of Europe, Dec. 15, 2015. URL: https://rm.coe.int/16806cc449.

[43] LG Chem. *Rechargeable Lithium Ion Battery Model: INR18650 MJ1 3500mAh*. Product Specification LRB-PS-CY3500_MJ1. LG Chem, 2016.

[44] H.-C. Chang and L.-C. Wang. *A Simple Proof of Thue's Theorem on Circle Packing*. Version Number: 1. 2010. DOI: 10.48550/ARXIV.1009.4322. URL: https://arxiv.org/abs/1009.4322.

[45] R. N. Schaezler and A. J. Cook. «Report on ISS O2 Production, Gas Supply and Partial Pressure Management». In: International Conference on Environmental Systems. Bellavue, WA: NASA, July 2015. URL: https://ntrs.nasa.gov/citations/20150010425.

[46] M. S. Escartí-Guillem, L. M. Garcia-Raffi, and S. Hoyas. «Review of launcher lift-off noise prediction and mitigation». In: *Results in Engineering* 23 (Sept. 2024), p. 102679. DOI: 10.1016/j.rineng.2024.102679. URL: https://linkinghub.elsevier.com/retrieve/pii/S2590123024009344.

[47] NASA. *Payload vibroacoustic test criteria*. NASA-STD-7001A. Jan. 21, 2001.

[48] D. C. Allgood, G. P. Saunders, and L. A. Langford. *Reduction of Altitude Diffuser Jet Noise Using Water Injection*.

[49] NASA. *Acoustic loads generated by the propulsion system*. June 1971.

[50] MATLAB. *surrogateopt - Surrogate optimization for global minimization of time-consuming objective functions*. URL: https://it.mathworks.com/help/gads/surrogateopt.html.

Acknowledgements

Un ringraziamento profondo va sicuramente ai miei genitori, il faro che ha sempre illuminato il mio sentiero, che mi hanno insegnato ad essere curioso e ad inseguire i miei sogni, e a tutta la mia famiglia che mi è sempre stata accanto con affetto.
La mia gratitudine va anche ai professori Karim Abu Salem e Giuseppe Palaia, in quanto mi hanno supportato e ispirato durante il mio percorso, lasciando la loro impronta nella mia formazione di ingegnere.
Infine, ai miei amici, che riescono ad essere per me fonte inesauribile di gioia e spensieratezza, oltre che un rifugio sicuro nei momenti difficili. I ricordi che abbiamo costruito negli anni sono per me un tesoro prezioso.